UNIVERSITAT DE BARCELONA

Holographic collisions and non-conformal dynamics

Miquel Triana Iglesias

HOLOGRAPHIC COLLISIONS AND NON-CONFORMAL DYNAMICS

MIQUEL TRIANA IGLESIAS

Departament de Física Quàntica i Astrofísica
Universitat de Barcelona

April 2017

UNIVERSITAT DE
BARCELONA

EXCELENCIA
MARÍA
DE MAEZTU

Institut de Ciències
del Cosmos

Programa de Doctorat en Física

HOLOGRAPHIC COLLISIONS AND NON-CONFORMAL DYNAMICS

A dissertation submitted to the University of Barcelona
for the degree of "Doctor per la Universitat de Barcelona"

I certify that this thesis was prepared under

the supervision of

Dr. David Julian Mateos Solé

ICREA Research Professor

and the tutoring of

Dr. Domènec Espriu Climent

Full Professor (Catedràtic)

both from the Departament de Física Quàntica i Astrofísica

Barcelona, April 2017

Als meus pares, a qui els ho dec tot.

A l'Ana, amb qui he compartit el camí.

Preface

The work presented in this thesis is the result of a series of research projects conducted during the period 2013-2017 within several scientific collaborations. These projects culminated in a series of publications[1–5] focused on the topics of applied holography, field theory and heavy ion physics.

The thesis is organized as follows:

- Chapter 1 serves as an introduction and motivation for the research presented in the next chapters. It contains a literature review covering the basics of heavy ion physics, hydrodynamics, applied holography and the numerical techniques we use throughout the thesis.

- Chapter 2 is a self-contained chapter in where we present the first holographic collision simulations with baryon charge and discuss the results obtained.

- In chapters 3, 4 and 5 we present a family of non-conformal models with a holographic dual and study it. In chapter 3 we examine its thermodynamics, transport properties and near-equilibrium properties. In chapters 4 and 5 we explore its far from equilibrium dynamics through shock-wave collision simulations and instability triggering.

- Chapters 6 and 7 contain the summary and conclusions, in English and Catalan respectively.

Acknowledgements

First and foremost I wish to express my gratitude to my thesis director David Mateos, under whose supervision the research presented in this thesis was conducted. During these years he has gone far beyond his duties as a thesis director becoming a true mentor. He has taken active part in my scientific training and career by devoting his time, and has often given me valuable advise at professional and personal levels. He has also funded – from his ERC grant – my travelling expenses to schools and conferences allowing me to learn, network and promote my research. In addition, as a principal investigator, he proved to be an excellent team manager: he has always been fair, trusting, and has given me the freedom and space to learn and work. From David I learned not only physics, but also scientific wisdom and professional attitudes that will sure be extremely useful in the future.

I also want to thank all the excellent people with whom I shared research projects: without them, this thesis as it stands would not have been possible. I thank very much Wilke van der Schee for his help during my first years in research and for his beautiful Mathematica scripts, from which I learned so much. I also want to thank Jorge, Miguel, Daniel, Pau, Yago, Maximilian, Carlos and Yiannis for the hard work and the perseverance, it was a pleasure to collaborate with you all.

I thank also all the people with whom I shared a workplace, and more importantly, the passion for physics. Thanks Roberto and Tomeu for your interest and comments. Thanks Genís, Marina, David, Markus, Blai, Raimon, and Adriana for the engaging physics discussions. Thanks Ivan, Albert, Vicente, Carla, Isa, Mirian, Javi, and David for your company at the faculty and the lunch times together. I want to thank also the administration people in the department and in the ICCUB: Kayla, Bea, Cristina, Elena and Olga, thanks for your help and efficiency.

Finally, I want to thank Michal Heller, my once master's thesis supervisor. To him I have to thank the start of my scientific career and many of the insights I have today.

Arribar a escriure aquesta tesi no hauria estat possible de cap de les maneres sense el recolzament constant dels meus pares. De vosaltres en vaig aprendre la passió per aprendre, la constància i el gust pel coneixement. Gràcies a vosaltres he pogut dedicar-me sempre a allò que m'agrada.

Contents

Contents

Chapter 1

Strongly coupled phases, heavy ion physics and applied holography

1.1 Why strong coupling?

The development of Quantum Field Theory (QFT) has been one of the biggest achievements in physics during the past century – both in the theoretical and the experimental front. The predictions provided by QFT and its realization in our world, the standard model, have met the experimental results with a precision unprecedented in science. Although nowadays the standard model is regarded as an effective theory in need of a UV completion, a comprehensive understanding of it remains crucial in order to answer some of the fundamental questions of nature.

Nevertheless, and despite its success, the understanding and the predictive power of QFT is still partial and limited to a set of regimes and phenomena. The traditional approach to a particular QFT consists in a perturbative analysis of its generating functional in order to obtain scattering amplitudes of its degrees of freedom. This approach requires the presence of a small parameter, which for the most of cases is the coupling constant. For strongly coupled phases, ubiquitous in nature, the perturbative approach simply fails and alternative techniques are needed. A complete description of phenomena such as confinement, the presence of a mass gap in certain theories, or the dynamics in strongly coupled regimes will certainly require of new ideas.

The quest for the understanding of strongly coupled systems is driven by both theoretical and "practical" motivations. When it comes to QFT, the motto "more is different" is particularly relevant; a reductionist approach on the degrees of freedom

around the vacuum cannot describe many of the states contained in a field theory, like soliton solutions or strongly coupled phases. A true comprehension of QFT at all regimes is also indispensable for the progress of several branches of physics. Disciplines like nuclear physics, cosmology, astrophysics or condensed matter theory consider complex systems for which there is no complete description so far.

1.2 Quantum chromodynamics and heavy ion collisions

A compelling example of a QFT with strongly coupled phases is Quantum Chromodynamics (QCD), the gauge theory responsible for the strong interaction between quarks and gluons or, equivalently, between hadrons. QCD has several ingredients that make it both difficult to model and rich in behaviour. Namely, it is a non-abelian theory, and it shows a running coupling constant that is large at low energies. As a result of these properties the vacuum of the theory has a non-trivial structure: at low temperatures and moderate densities the degrees of freedom rearrange to form bound states. At higher temperatures, however, the physics of the theory changes radically and it shows anti-screening becoming asymptotically free [6]. Far from being solved, nowadays QCD is still a very active field of research involving many communities that span from ion and nuclear physics to string theory, cosmology or even math.

1.2.1 The experiments

The discovery of asymptotic freedom motivated the existence of a deconfined phase called Quark-Gluon Plasma (QGP). In order to create and study this new state of matter, the heavy ion collision program was started in the 70s decade. Using existing hadron accelerators (synchrotrons like Bevatron, AGS and SPS), the nucleus of some heavy atoms were accelerated to relativistic velocities and made collide. In these first experiments there were indications of the presence of a deconfined phase, although it would not be until the RHIC started its operation that the creation of the QGP would be confirmed in year 2000 [7]. The creation of the QGP in heavy ion colliders opened the possibility of studying a wide range of phenomena not present in nuclear matter. Phase transitions, symmetry breaking and restoration, equilibration, and many other effects became all the
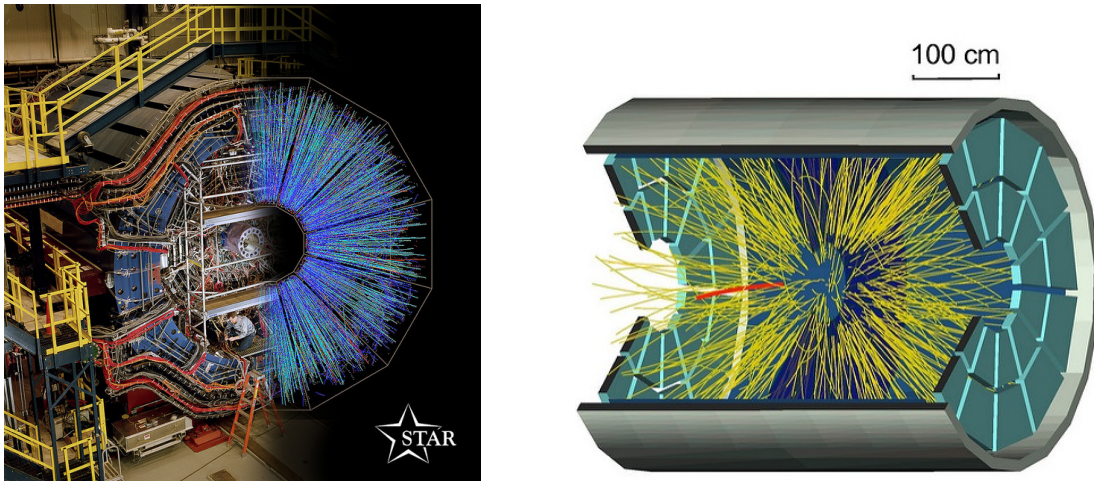
Figure 1.1: STAR detector at RHIC, Brookhaven. The diagrams depict the tracks of the produced particles, final outcome of the collision. Figures taken from RHIC website (www.bnl.gov/rhic) under creative commons licence.

sudden at the experimentalists range, giving a new tool for a deeper understanding of QCD and gauge theories in general.

Assessing the dynamics of a heavy ion collision from the debris collected in the detectors is a challenging endeavour. The detectors used in heavy ion colliders are typically a size of order $\sim 10 - 10^2$ meters. At this scale, the "fireball" produced in the collision has certainly expanded and cooled down enough for its matter to hadronize again, and the dynamics of its particles have decoupled or "freezed-out" (see fig. 1.2). An observable proposed in order to determine the presence of a collective deconfined state – the QGP – was the degree of azimuthal asymmetry in the momentum distribution of the produced particles[8]. This magnitude is known as the elliptic flow and corresponds to the second coefficient in the harmonic expansion of the final distribution of particles (v_2). Flows can also be obtained for specific species of particles, which are used to extract the net baryon momenta distributions (see fig 1.3) and provide additional information from the far from equilibrium dynamics of the collision.

Other important probes for the matter created in the experiments are the jets. When a very energetic particle crosses a medium it creates a cascade of particles, a jet. Studying the jets created in collisions provides extra and complementary information about the QGP. Although jets constitute a very significant part of the study of QGP, they are not part of the work presented in this thesis and will not be discussed any further.
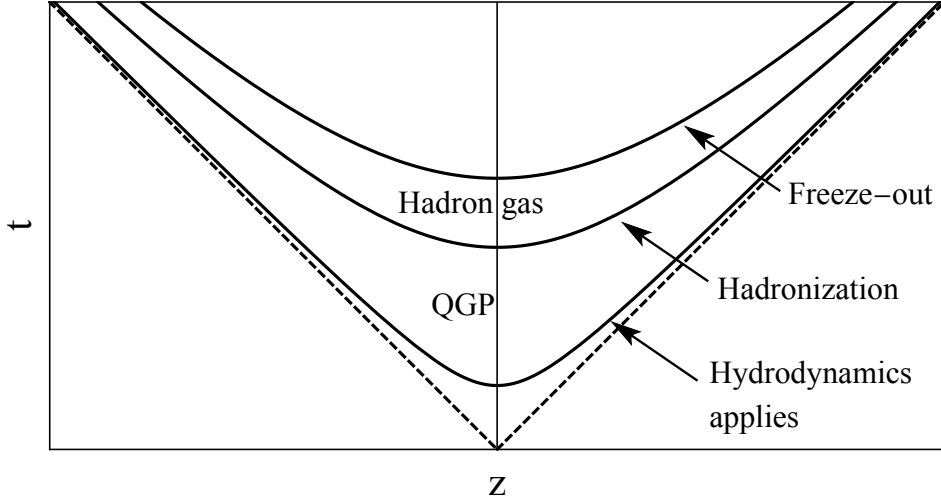
Figure 1.2: Cartoon picture of the stages of a heavy ion collision in terms of the longitudinal direction z and the laboratory time t. After a very short pre-equilibrium period the system becomes a fluid. Eventually it cools down enough to hadronize and freeze-out. The regions closer to the light-cone (dashed lines) suffer from Lorentz delay.
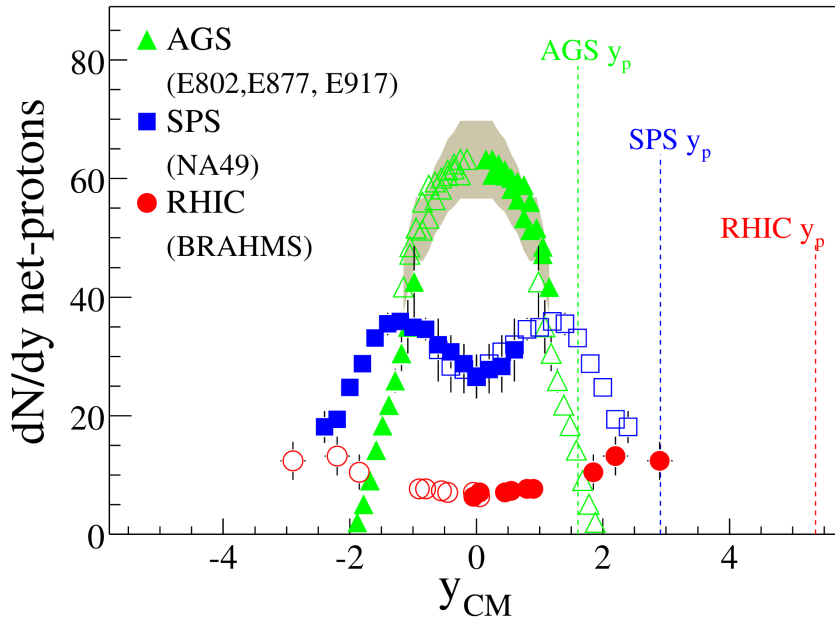
Figure 1.3: Net proton rapidity distribution (proton minus antiproton densities) obtained in different experiments at different energies. To obtain the net baryon distribution one needs to estimate the other hadron densities from the proton ones. Figure taken from [9] (BRAHMS collaboration at RHIC).

1.2.2 Hydrodynamics

The rationale behind the presence of the elliptic flow is rooted in the hydrodynamic behaviour of collective states near equilibrium. Hydrodynamics is a coarse grained effective description for field theories that works provided certain assumptions hold. The starting point for this description are the conservation equations for quantities like the stress-energy tensor or other conserved currents,

$$\partial_\mu T^{\mu\nu} = 0 \quad \text{and} \quad \partial_\mu J^\mu = 0 \tag{1.1}$$

Typically, the conservation equations are not enough to determine the dynamics of the system. As a consequence, the first necessary assumption of hydro is the reduction of the number of variables on which $T^{\mu\nu}$ and J^μ depend to meet the number of equations. The new hydrodynamic variables will be local notions of the temperature (or energy density) and the fluid velocity, and for the case of a conserved current, the chemical potential. The next assumption that hydro uses is the "local equilibrium" or the consideration of only long wavelength excitations. The long wavelength premise allows a gradient expansion of the expressions for $T^{\mu\nu}$ and J^μ, which to the first order and following the notation of [10] reads,

$$T^{\mu\nu} = \epsilon u^\mu u^\nu + p\Delta^{\mu\nu} + \eta\Delta^{\mu\alpha}\Delta^{\mu\beta}\left(\partial_\alpha u_\beta + \partial_\beta u_\alpha - \frac{2}{d}\eta_{\alpha\beta}\partial_\mu u^\mu\right) - \zeta\Delta^{\mu\nu}\partial_\lambda u^\lambda \tag{1.2}$$

$$J^\mu = nu^\mu - \sigma T\Delta^{\mu\nu}\partial_\nu(\mu/T) \tag{1.3}$$

Where $\Delta^{\mu\nu}$ is a projection tensor, and η, ζ and σ are the viscosities and conductivity respectively.

If the system produced after a heavy ion collision is big enough and has nearly equilibrated, its evolution might be described by hydrodynamics. When the heavy ions collide most of them do with a certain parameter of impact, producing some prolate ellipsoidal fireballs (see fig. 1.4). In case hydrodynamics is a good description for the system, the fireball will explode faster towards where it is narrower (and the pressure gradients are bigger), and hence it will produce elliptic flow. The elliptic flow was indeed observed in RHIC (and later in the LHC) and the data collected in the detectors could be reproduced with a good agreement using ideal hydrodynamic simulations after a very short pre-equilibrium stage ($t \sim 1$ fm/c) [11].
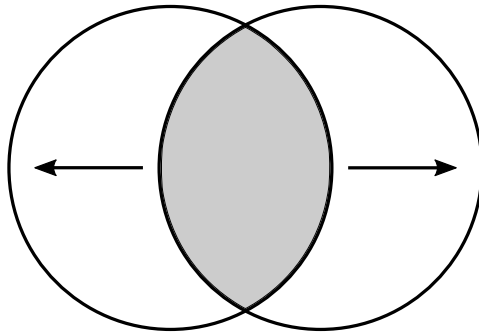
Figure 1.4: Diagram of an off-central collision where the circles represent the heavy ions seen from the longitudinal direction. The overlaping region corresponds to an "almond shaped" droplet of plasma produced in the collision. A hydrodynamical expansion of this droplet generates an angular dependence in the final distribution of particles.

The fact that ideal hydro is a good description for the QGP created in collisions awarded to it the title of "the most perfect liquid in nature". Nevertheless, improved hydrodynamic simulations including viscosity showed that in fact the QGP is best described with a very small, but non-vanishing, shear viscosity [12]. Although computing viscosities from first principles is very far from trivial, simple arguments can be used to show that a weak coupling between the degrees of freedom typically leads to big viscosities (see [13, 14] for viscosity reviews in the context of holography).

In a happy coincidence, by the same time RHIC announced the finding of the QGP, the gauge/gravity correspondence was discovered and offered a novel way to perform calculations at strong coupling. In particular, the computation of the shear viscosity for a large class of QFTs at strong coupling made a deep impression in the way we see the QGP nowadays (see [15] for the first calculation, and [16] for a generalization of it). The result given by holography was in agreement with the small viscosity seen at the experiments and, although it was obtained in theories different from QCD, it pointed that the QGP after a first equilibration could be in an strongly coupled regime.

1.2.3 Equilibration process and theoretical efforts

Regardless of the many inputs coming from thermodynamic and hydrodynamic calculations, at the current time the physics of heavy ion collisions remains far from being completely understood. The reason for this is that heavy ion collisions are very violent events for which important parts of their dynamics happen very far from equilibrium. In addition, one has to bear in mind that the collision and equilibration physics probe a wide

range of energy scales. The kinetic energy per nucleon before the collisions at RHIC and LHC is of the order $\sim 10^2 - 10^3$ GeV, energy at which the interaction strength is certainly small. On the other hand, the crossover temperature has been computed using lattice QCD obtaining a value range of $T = (185 - 195)$ MeV [17]. Even if after the equilibration the system might be well described by strongly coupled dynamics, the equilibration process itself necessarily involves a mixture of weakly and strongly interacting physics.

The approaches used to model the pre-equilibrium stage are complementary as they consider opposite regimes; this is, the weak and the strong coupling limits. The reason for using such limits is that the computations required, despite challenging, become feasible. Although neither of the descriptions holds the complete picture for the collisions, the hope is that a proper understanding of them will shed light on the real dynamics observed in the experiments. Remarkably, so far both approaches have been successful in reproducing some features of the real QGP, like the fast hydrodynamization (see [18] for a comparative analysis of both approaches).

The techniques used to compute dynamics for the two opposite regimes are completely different. In the weakly interacting limit one might use a perturbative calculation on QCD (refs. [19, 20] contain some recent developments). For strongly coupled dynamics, however, there is no other option than using toy models instead of actual QCD. Theories like $\mathcal{N} = 4$ super Yang-Mills share important features with QCD and might capture part of its dynamics. In addition, some of these toy model theories can be described in terms of a dual gravitational theory reducing the problem to the solution of differential equations like the Einstein's equations (we refer the interested reader to [21] for a comprehensive review of heavy ion collisions in the context of holography). It is worth to mention that there already are efforts in a hybrid approach to the problem using both frameworks patched together (ref. [22] contains first numerical calculations for a semi-holographic set-up).

In the next sections we introduce the gauge/gravity duality and summarize the recent developments in the study strongly coupled gauge theories and the QGP.

1.3 The gauge/gravity correspondence

1.3.1 Formulation

The gauge/gravity duality, loosely called holography, is a correspondence between some quantum gravity theories –ultimately string theories– and their gauge theory counterparts. The ideas enclosed in the holographic principle can be traced back as early as the black hole thermodynamics [23, 24] and the 't Hooft planar limit [25]. Nevertheless, a very concrete realization of it would be given in the seminal paper by Juan Maldacena in 1997 ([26], followed by [27] and [28] by other authors). At the time, the best understood example of the correspondence was the one relating type IIB string theory in $AdS_5 \times S_5$ and the gauge theory $\mathcal{N} = 4$ Super Yang-Mills (SYM). Nowadays there are several other examples of the correspondence, but perhaps the aforementioned one remains amongst the most explored and widely used.

The arguments given by Maldacena to stablish the gauge/gravity duality rely on the D-branes and the existing equivalent descriptions for their dynamics. The D-branes are some extended objects described by string theory in which open strings can end. The strings attached to the D-branes have a fluctuation spectrum that gives raise to some dynamics associated with the branes.
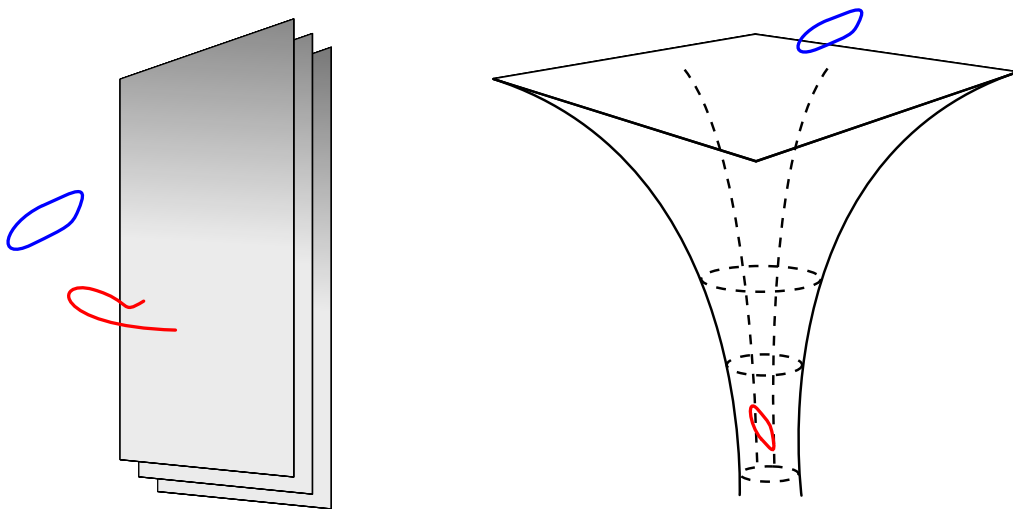

Figure 1.5: Alternative descriptions for the dynamics of strings attached to a stack of D3-branes (red strings). The strings attached to the branes can be modelled as open strings ending on the D3-branes (left panel), or as closed strings moving in the curvature generated by the branes (right panel).

When a stack of N_c D3-branes in type IIB string theory is considered, the dynamics of its low-energy excitations is described by $\mathcal{N} = 4$ super Yang-Mills theory. The same dynamics admits as well an equivalent description. As massive objects, the D-branes generate curvature around them. If one sits closely to the D3-branes, the geometry can be written as $AdS_5 \times S_5$, and the strings attached to it can be modelled as closed strings trapped and moving in the curved space generated (depicted in fig. 1.5). At the limit where $\alpha' \to 0$ (the low energy limit), the strings attached to the branes decouple from the ones outside of it and the two systems become non-interacting. Thus, the descriptions for the dynamics of the attached strings in terms of $\mathcal{N} = 4$ SYM theory and closed strings in $AdS_5 \times S_5$ can be identified in a correspondence.

The gauge/gravity duality is strongly motivated at the regime at which string theory is well described by supergravity. This is at the large 't Hooft coupling ($g_{YM}^2 N_c = \lambda \to \infty$) and large number of colours for the dual field theory. However, there are several computations at both sides of the duality showing that corrections in λ and N_c (or equivalently g_s and α') agree and, thus, nowadays the duality is believed to be true at any values of λ and N_c (see ref. [29] for a review on holography and a discussion on the regime of validity). This way, the correspondence provides an alternative manner to answer questions regarding a particular theory, which is by means of its holographic dual.

Despite finite λ and N_c would be the appropriate set-up in order to model QCD, the gravitational dual for such gauge theory would be a full non-perturbative string theory for which our knowledge is very limited. Consequently, the large λ and N_c limit is used to model the dynamics of the QGP and in most of the field of "applied holography".

1.3.2 How to use it

In order to perform calculations in a gauge theory using holography one needs first a particular realisation of it that captures the desired features of the system of study (dimension, symmetries etc.). In the ideal case, it is optimal to use a realization given from a brane construction as the ones introduced by Maldacena. This is known as the "top-down" approach and has several advantages. In top-down cases the field theories are typically well known, including their field content and gauge group. In addition, knowing the brane construction provides a better control of the gravity solution and its stability. Unfortunately, the set of known realisations of the duality is very limited and they cannot describe a good share of the physics of hot QCD. This is the case of $\mathcal{N} = 4$ SYM, which is a conformal theory and therefore is unable to show any RG flow and

confinement. Thus, this theory should only be used to model heavy ion collisions at the stages where the QGP is near-conformality and far-away from the cross-over.

To overcome the lack of toy models derived from a brane construction, one might use the "bottom-up" approach. The starting point in this case is an ad-hoc asymptotically AdS (super)gravity model that will be dual to a gauge theory with the desired properties. Although the string theory embedding for the gravitational model is not known, sometimes it can be argued that it exists and therefore provides a construction that raises a duality. An obvious disadvantage of it is that the dual field theory is only known partially through some of its operators and symmetries. The bottom-up approach gives holography more flexibility and the possibility to make the toy models closer to real QCD.

The prescription that relates operators in the gauge theory with the fields on the gravity side of the duality was given by Witten in [27],

$$\int \mathcal{D}[fields]e^{-S+\int \mathcal{O}\phi_0} = Z_{\mathcal{O}}[\phi_0]_{CFT} \approx Z_{classical}[\phi_0]_{SUGRA} \approx e^{S_{SUGRA}[\phi[\phi_0]]} \qquad (1.4)$$

This prescription equates the euclidean generating functional of the gauge theory to the classical partition function of the supergravity when the boundary conditions of the fields are set to the value of the sources in the gauge theory. In addition, the old notions of black hole thermodynamics provide the gravitational prescriptions for the temperature and the entropy density when the system of study is a thermal state. These correspond to the surface gravity and the surface density at the horizon of the black hole representing this thermal state. In conclusion, a solution of the gravity theory will represent a state in the gauge theory, and an evolving geometry will give a real time evolution.

From the generating functional and Witten's prescription one can obtain all the gauge theory n-point functions in terms of the gravity dual fields (or the "bulk" fields). Amongst these, the easiest to compute and perhaps the most useful for collision dynamics are the 1-point functions or expectation values, which give the energies, pressures, and charge densities of the system. The starting step for the extraction of the VEV of an operator of interest is to identify to which bulk field does it "couple". In case we are using a brane construction, this can give us the precise relation between the fields and operators. Conversely, when a "bottom-up" approach is used one needs to rely on symmetry arguments. Very common examples of this are the coupling of the metric field $g_{\mu\nu}$ to the stress-energy operator of the gauge theory $T_{\mu\nu}$, or the relation between gauge fields in the bulk A_μ^a and conserved currents J_μ.

With the field-operator relation in hand and eq. (1.4), the expression for the VEV is

$$\langle\mathcal{O}(x)\rangle = \frac{\delta}{\delta\phi_0(x)}Z_{\mathcal{O}}[\phi_0]|_{\phi_0=0}\,. \tag{1.5}$$

It is important to note that the actions for the theories at each side of the duality suffer from divergences. To successfully use eq. (1.5) to extract finite values for the VEVs, one needs first to renormalise the bulk action at the UV through a procedure known as "holographic renormalization" presented in [30].

The appropriate coordinate system to extract the gauge theory quantities and conduct the holographic renormalization computation is the one introduced by Fefferman and Graham. This coordinate system foliates the asymptotically AdS geometries in surfaces diffeomorphic to the conformal boundary, allowing the rewriting of (1.5) in terms of the bulk fields and a cut-off (refs. [31,32] contain detailed discussions about geometrical aspects of holographic renormalization). The Fefferman-Graham ansatz for an asymptotically (d+1)-dimensional AdS geometry in the Poincaré patch reads,

$$ds^2 = \frac{L^2}{u^2}\left(du^2 + g_{\mu\nu}(t,\mathbf{x},u)dx^\mu dx^\nu\right) \tag{1.6}$$

where L is the radius of the AdS and u the holographic coordinate, and

$$g_{\mu\nu}(t,\mathbf{x},u) = g_{(0)} + g_{(2)}u^2 + \cdots + g_{(d)}u^d + h_{(d)}u^{(d)}\log(u^2) + \mathcal{O}(u^{d+1}) \tag{1.7}$$

In this coordinates the conformal boundary is located at $u \to 0$. Very often in the literature the coordinate r is used for the inverse coordinate $r = 1/u$, with the conformal boundary at $r \to \infty$.

The process of extracting the gauge theory quantities is often called "reading off at the boundary". The reason for this is that the RHS of eq. (1.5) is ultimately expressed in terms of the near-AdS-boundary expansion coefficients for the bulk fields. When a bulk field is solved near the boundary, one realizes that typically there are two independent modes: a normalizable and a non-normalizable mode. The non-normalizable mode is fully constrained by the boundary conditions and is associated with the source for the dual operators. The normalizable mode, on the other hand, is unconstrained and depends on the whole space-time geometry. This mode is also the one carrying the non-trivial information of the 1-point functions. For the $d = 4$ pure gravity case dual to $\mathcal{N} = 4$ SYM the VEV of the stress-energy tensor, without including the scheme dependent terms, is

given by

$$\langle T_{\mu\nu} \rangle = \frac{N_c^2}{2\pi^2} \left[g_{(4)\mu\nu} - \frac{1}{8} g_{(0)\mu\nu} \left[(\mathrm{Tr} g_{(2)})^2 - \mathrm{Tr} g_{(2)}^2 \right] - \frac{1}{2} (g_{(2)}^2)_{\mu\nu} + \frac{1}{2} g_{(2)\mu\nu} \mathrm{Tr} g_{(2)} \right] \quad (1.8)$$

where we used the relation between the gravitational constant and the degrees of freedom $L^3/\kappa_5^2 = N_c^2/4\pi^2$ specific to this theory. The coefficient $g_{(2)}$ can actually be written in terms of the boundary metric $g_{(0)}$ and derivatives of it, and is 0 for $g_{(0)\mu\nu} = \eta_{\mu\nu}$. Note that in this case the whole expression reduces to $\langle T_{\mu\nu} \rangle = N_c^2/(2\pi^2) g_{(4)\mu\nu}$.

1.4 Linear dynamics and quasi-normal modes

Short after its discovery, holography started offering quantitative results and new insights for strongly coupled field theories. The first advances were done on linear dynamics, linear response, and close to equilibrium situations – which correspond through holography to thermal dissipation and hydrodynamics. This was possible because the linear approximation involves a major simplification of the dynamic equations of the bulk, allowing the calculation of solutions with modest computational resources, or even analytically.

When a close-to-thermal system is modelled, the fluctuations on top the dual equilibrium black hole (BH) can be expressed in terms of solutions of the linearized equations over a background. The gauge invariant combinations of these are known as the Quasi-Normal Modes (QNMs) and have the form,

$$\Phi(t, \mathbf{x}, u) = A\Psi(u) e^{-i\omega t + \mathbf{k} \cdot \mathbf{x}} \quad (1.9)$$

where $\mathbf{x}$ are the boundary coordinates, u the holographic coordinate, and ω and k are the complex frequency and the wave number of the mode. As a result of the boundary conditions at the BH horizon and the AdS boundary, the set of solutions is discrete in ω, and this takes complex values giving raise to oscillating and decaying behaviour (see fig. 1.6). The gauge invariant fluctuations Φ can be constituted by components of the dynamic fields in the bulk theory or combinations of them.

The QNMs were long known in the context of black hole physics, and could be quickly applied to holography and thermal dissipation studies (see [33] for a first calculation in AdS to extract dissipation times). Soon after, they would be interpreted more precisely as the spectra of poles of the retarded Green function of the field theory [34], opening
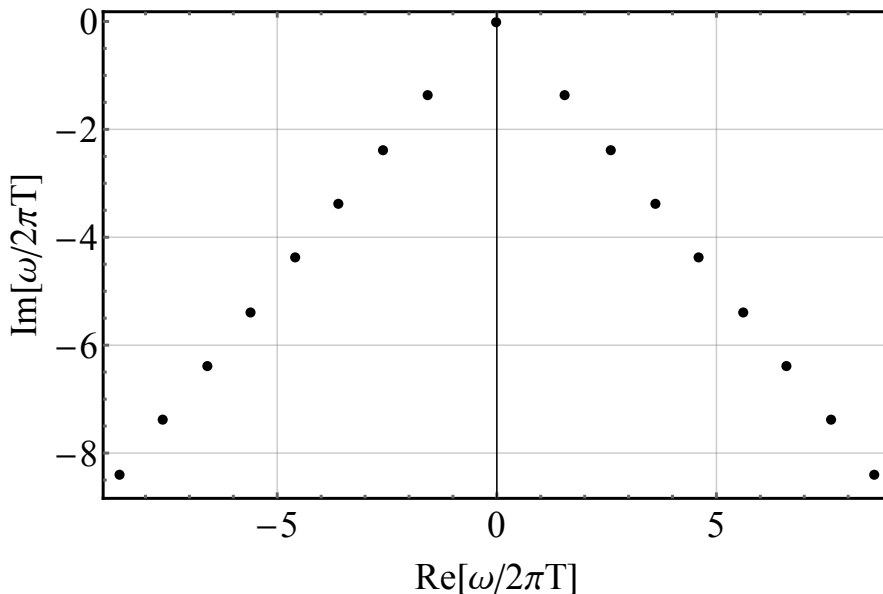
Figure 1.6: First quasi-normal frequencies for the $k = 0$ fluctuations of $\Delta = 4$ operators in $\mathcal{N} = 4$ SYM. This includes the spin 0 fluctuations of the metric in the bulk, corresponding to the sound channel of the stress-energy tensor in the boundary theory. Frequencies computed with the spectral decomposition eigenvalue method.

a new way to study systems close to equilibrium. The study of QNM also provided an explanation for the long life of the hydrodynamic regime in a strongly coupled phase. Hydrodynamic modes appear naturally in the calculations as the lowest of the non-homogeneous QNMs. Their dissipation rate tipically goes to 0 as $k \to 0$, i.e. long wave-lengths, which is precisely one of the assumptions of the hydrodynamic descriptions. Other uses of the QNMs include the study of the different channels of dissipation of a system [35], instabilities and transitions [36], and the effects of non-conformality in the dissipation process [1, 37] or the 't Hooft coupling λ corrections [38].

The methods used to solve the eigenvalue problems involved in the QNMs computation are diverse and adapted to the specific cases. The first calculations were performed using the Frobenius method, consisting in approximating the solutions of the equations using series with a large but finite number of terms [34, 35]. One then can solve the equations order by order close the horizon with the appropriate boundary conditions, and impose normalizability at the boundary. More involved cases might require the use of shooting-like methods, which is the case of the theory $\mathcal{N} = 2^*$ SYM theory studied in [39]. Finally, there is an extremely efficient method (used in [1, 36, 37]) that works

provided the fluctuation equations can be expressed in the form,

$$\hat{L}_1 \Psi(u) = \omega \hat{L}_2 \Psi(u) \tag{1.10}$$

where $\hat{L}_1$ and $\hat{L}_2$ are linear operators, and Ψ is the spatial profile of the modes. In this case, one might discretise the equation using spectral functions and solve the matricial eigenvalue problem using existing libraries.

As a final remark, it is interesting to note that the range of validity of the linear approximation sometimes also extends to far-from-equilibrium states. Studies like [40] show that the linearized equations can succesfully describe phenomena such as far-from-equilibrium homogeneous isotropization of a plasma within a 20% precision (see fig. 1.7).

1.5 Full numerical evolutions

With hindsight, the computation of full dynamics in the bulk appears to be the next logical step in the holographic plasma program. This would allow the extraction of far-from-equilibrium real time dynamics in a strongly coupled phase. However, non-linar computations in the bulk amount to the solution of a very non-trivial set of differential equations containing the Einstein's equations plus the ones for other fields. Solving this kind of systems is usually a very challenging problem extensively studied in the past. As a result, a whole branch of physics – numerical general relativity (GR) – is dedicated to the techniques involved in it.

The numerical evolution of space-times, with or without matter, has been attempted since the 1960s. Technical difficulties, however, have made the progress in the field both hard and slow for decades. It is very illustrative to note that, although the first axis-symmetrical black hole collisions where simulated in 1976, it would take 30 years until Frans Pretorius succesfully computed the collision of inspiralling black holes in 2005 [41]. Recent new techniques and computational resources have spurred a revolution in the field, allowing the evolution of many different systems that had remained intractable for a long time.

1.5.1 The characteristic formulation

There exist several formalisms in order to attempt the solution of a particular problem, among them we can find the Cauchy-based and the characteristic approaches. The latter is the one commonly used for evolutions in the Poincaré patch of AdS, and it poses three main advantages when applied to these set-ups. Namely:

- The initial data is free and one only needs to specify some of the dynamic functions. The constraints are automatically fulfilled.

- Only first time derivatives appear in the evolution equations, resulting in a smaller number of variables.

- The set of equations simplifies significantly. It adopts a hierarchical nested structure (partially or completely) and effectively decouples. It also linearizes (again, totally or partially) and becomes fully ultra-local, i.e. the system of partial differential equations (PDEs) reduces to ordinary differential equations (ODEs) with some coordinates as parameters.

The major drawback present in this formalism, the formation of caustics along the coordinates, is typically non present in Poincaré-AdS evolutions as the possible caustics form behind the black brane horizons (see [42] for a discussion about this point).

The characteristic formalism was originally introduced by Bondi [43] and Sachs [44] in 1960s for the study of gravitational waves. Although nowadays it is not very popular in the numerical GR community, the characteristic approach had some successes in the field; the first stable simulation of a black hole in 3D in 1998 is a good example of it (see [45] for a comprehensive review on the formalism).

The starting point for a characteristic evolution is the Bondi-Sachs metric ansatz which is a generalised form of the Eddington-Finkelstein metric. Following the notation of [42], a version of this metric ansatz particularly suited for holographic computations reads,

$$ds^2 = G_{ij}(t, \mathbf{x}, r)dx^i dx^j + 2dt \left[dr + A(t, \mathbf{x}, r)dt + F_i(t, \mathbf{x}, r)dx^i \right] , \qquad (1.11)$$

where r is the holographic coordinate, x^i the spatial coordinates of the boundary theory, and t is the "time" coordinate coinciding at the boundary with the gauge theory time. The fundamental feature of this metric is that uses ingoing null geodesics as the integral curves that generate one of the coordinates, r. With this, the constant t slices are null

hypersurfaces, although ∂_t itself is not null. Then, the step that dramatically simplifies the dynamic equations is expressing them using the outgoing null derivative

$$d_+ \equiv \partial_t + A(X)\partial_r \, . \tag{1.12}$$

Nevertheless, the "time" integration itself is performed on the coordinate t.

1.5.2 Discretisation and spectral methods

The numerical resolution of the differential equations involved in GR necessarily requires a discretisation of the domain of integration. There exist a big number of methods to attempt such discretisation and resolution depending on the particular features of the equation of study. For generic unbound ODE problems, Euler-like methods as the Runge-Kutta or the Adams-Bashford show both robustness and reasonable speeds. This is the case of time integrations and coordinate transformations, usually solved using Euler-like methods. However, when the domain of integration is well defined and the equations are linear, more efficient and precise methods can be used.

The equations appearing in the nested scheme within every time step of a characteristic evolution are generally linear and can be written as,

$$\hat{L}(x)f(x) = S(x) \, . \tag{1.13}$$

Where $\hat{L}(x)$ is a generic linear operator built with derivatives and linear functions, $f(x)$ is the function we solve for, and $S(x)$ is a known independent term. Thanks to linearity, the equation can be discretised and rewritten in a matricial form as,

$$\sum_{j=0}^{N} L_{ij}\widetilde{f}_j = \widetilde{s}_i \quad \text{for} \quad \forall i \leq N \, . \tag{1.14}$$

Finding the solution for the discretised version of $f(x)$ amounts then to the inversion of the matrix L_{ij}. However, due to the multiplicity of solutions depending on the boundary conditions of the equation, this matrix is usually non-invertible. This problem can be solved by substituting some rows in equation (1.14) by a representation of the boundary conditions in the selected basis. The inversion of the matrix or, equivalently, the resolution of the linear system can be achieved by using existing routines in almost every programming environment.

Given a number of points or functions in the basis, the discretisation procedure is far from unique. These procedures can be classified in two big groups: the spectral methods and finite differencing. The spectral methods are arguably the most precise and challenging method of the two, and rely on a spectral decomposition of the functions and operators in a orthogonal basis. Among the most used functions for the decomposition we can find the Chebyshev polynomials or the Fourier basis (the latter being specially suited for periodic boundary conditions). As the number of functions used in the decomposition is finite, there is some error associated with the discretization procedure, which is again non-unique. The discretisation method used in the work presented in this thesis is the so-called "collocation points" method (see [46, 47] for extensive guides on spectral methods and collocation points). The finite differencing method shares important features with the spectral methods. In this case, however, the discretization is done through a point by point interpolation of the functions in m-th order polynomials. The interpolation grid can be set to any N point grid.

Spectral methods and finite differencing are also useful for other kind of problems. For two-boundary non-linear ODE problems – such as the apparent horizon equation in 2+1 simulations – one might use a relaxation Newton's method. In this method one iteratively modifies a seed solution by linear corrections. The linear corrections are found by solving the linerised equation using spectral methods or finite differencing.

1.5.3 Homogeneous isotropization

In pioneering work by Chesler and Yaffe, the characteristic approach was first applied in holography in order to study the relaxation of far-from-equilibrium plasmas in a homogeneous four dimensionsional set-up [48]. The gravitational model used for this study was the simplest possible: pure Einstein gravity on an asymptotically $AdS_5 \times S_5$ space, which is a consistent truncation of the type IIB supergravity. The gauge theory evolved then would be $\mathcal{N} = 4$ SYM, a conformal theory sharing important features with QCD. This choice of set-up is motivated by simplicity and requires the further assumption of conformality for the system modelled. As we will argue chapter 3, this might be justified in extremely hot plasmas but not at temperatures close to critical temperature of QCD.

The action describing the pure gravity set-up is the Einstein-Hilbert with a cosmological constant,

$$S = -\frac{1}{16\pi G} \int d^5 x \sqrt{-g} \left(\mathcal{R} + \frac{12}{L^2} \right) , \tag{1.15}$$

which results in the Einstein's equations

$$\mathcal{R}_{mn} + \frac{4}{L^2} g_{mn} = 0 . \tag{1.16}$$

By constraining the ansatz (1.11) to have dependence only on coordinates r and t and setting the fluxes $F_i = 0$, one can impose homogeneity on the dual plasma. Decreasing the number of dynamic directions results in a drastic computational time reduction and a simplification of several technical aspects. This simulations are popularly known as "$1 + 1$", as they consider dynamics in one spatial direction plus the time. In this case the simplified metric reads,

$$ds^2 = \Sigma^2 \left[e^B d\mathbf{x}_\perp^2 + e^{-2B} dx_\parallel^2 \right] + 2dt \left[dr + A dt \right] , \tag{1.17}$$

where it is necessary to allow for anisotropy in the $x_\perp$ and $x_\parallel$ directions to obtain an evolving metric free of divergences [49]. It is precisely this anisotropy in the metric the one giving raise to pressure anisotropy in the dual plasma.

The homogeneous simulations cannot capture any kind of flow by construction. However, the results obtained in this first simulations in [48] and [40] were successful in reproducing a fast "equilibration" in the plasma of study, which in this simple set-up amounts to a fast isotropization. The time the system spends in isotropying was found to be of order the inverse of the temperature (see fig. 1.7), which is in line with the observations in the experiments.

Subsequent works have studied homogeneous relaxation using other gravitational theories. In ref. [50] the model considered is Einstein-Maxwell in order to capture the equilibration process in presence of external magnetic fields and conserved charges. In [36] a scalar field is added in the dynamics to add non-conformality and instabilities in the dual gauge theory. One can also consider higher derivative gravity models, like Gauss-Bonet gravity, to study the effects of the coupling λ corrections [51].
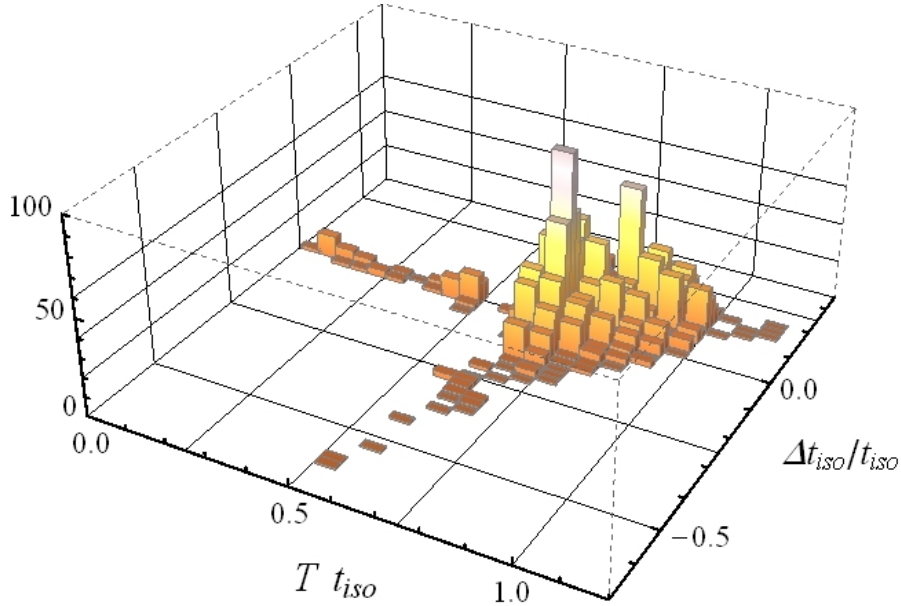
Figure 1.7: in ref. [40] ~ 2000 initial far from equilibrium states were evolved, both linearly and with a full dynamic code. The results depicted in the histograms show how the isotropisation time (t_{iso}) is always of order the temperature (T) and that the linear approximation gives for most of cases a good prediction for t_{iso} up to a 20% error. Figure originally appearing in [40].

1.5.4 Shock-wave collisions

In order to study the onset of hydrodynamics and make contact with the experiments, one needs to allow for inhomogeneities in the set-up. The metric ansatz in this case considers the presence of "flux" metric coefficient F,

$$ds^2 = \Sigma^2 \left[e^B d\mathbf{x}_\perp^2 + e^{-2B} dx_\parallel^2 \right] + 2dt \left[dr + Adt + Fdx_\parallel \right] , \qquad (1.18)$$

and the dynamics is now allowed in the coordinates r and $x_\parallel$; this is, "2 + 1" simulations.

The next step is to provide an initial state that can reproduce some of the characteristics of the real collisions in experiments. The desired state needs to feature two long-lived initial projectiles, travelling at speeds close to c in a collision course. For a "2 + 1" evolution this projectiles are two infinite sheets of energy with translational symmetry in the transverse plane known as the shock-waves. A proposal of a holographic implementation of them is introduced in [52], and used in [53] for studying the infinitely thin shock-wave limit. However, the first full-fledged dynamic evolution would be performed by Chesler and Yaffe, again in pure gravity, in [54]. In the original notation of Chesler and Yaffe the

shock-wave metric in Fefferman-Graham coordinates reads,

$$ds^2 = \frac{L}{r^2} \left(dr^2 + h(x_\pm)dx_\pm^2 + r^4 \left[-dx_+dx_- + d\mathbf{x}_\perp^2 \right] \right) . \tag{1.19}$$

where $x_\pm = t \pm z$, and $h(x_\pm)$ is a free function that characterizes the waveform. Using eq. (1.8) we can immediately obtain the VEV for the stress energy tensor of the initial state,

$$\langle T_{\mu\nu} \rangle = \frac{N_c^2}{2\pi^2} \begin{pmatrix} h(t \pm z) & \pm h(t \pm z) & 0 & 0 \\ \pm h(t \pm z) & h(t \pm z) & 0 & 0 \\ 0 & 0 & 0 & 0 \\ 0 & 0 & 0 & 0 \end{pmatrix} \tag{1.20}$$

which corresponds to a pressure and density wave of a fluid travelling in vacuum. After transforming the shock-wave metric from the Fefferman-Graham to the Bondi-Sachs form, one can evolve the configuration to simulate a collision and its subsequent equilibration. The outcome of the computation is a dynamic geometry that, through holography, is equivalent the evolution of the $\langle T_{\mu\nu} \rangle$ of the dual plasma (see fig. 1.8). With the stress-energy tensor one might study the longitudinal flow and the rapidity profiles of the debris, and with them the onset onset of hydrodynamics in the plasma after the collision.

An effective way to test whether hydrodynamics is a good description of the system is to verify that the stress-energy tensor can be approximately written in the form of equation (1.2). To do so, one needs to extract the local energy and velocities of the fluid by diagonalizing $\langle T_{\mu\nu} \rangle$, and plug them in the hydrodynamic constitutive expression (1.2). Along the information extracted from the dynamics, it is also necessary to provide an "equation of state" relating the pressure and the energy in equilibrium ($\epsilon = 1/3p$ for a conformal fluid), and the transport coefficients for the theory studied ($\eta/s = 1/4\pi$ and $\zeta = 0$ for $\mathcal{N} = 4$ SYM). Then, if the predicted "hydrodynamic stress-energy tensor" agrees with $\langle T_{\mu\nu} \rangle$ up to a certain tolerance, one might declare that the plasma has "hydrodynamized" (see fig. 1.9). One of the main results found in [54] is indeed the fast hydrodynamization time, that gives a result of order the temperature of the plasma, again in line with the data from the experiments. After the plasma has hydrodynamized, the evolution can be continued using a fully fledged hydrodynamic simulation and attempt a more quantitative comparison with the experimental data, as it is done in [56].
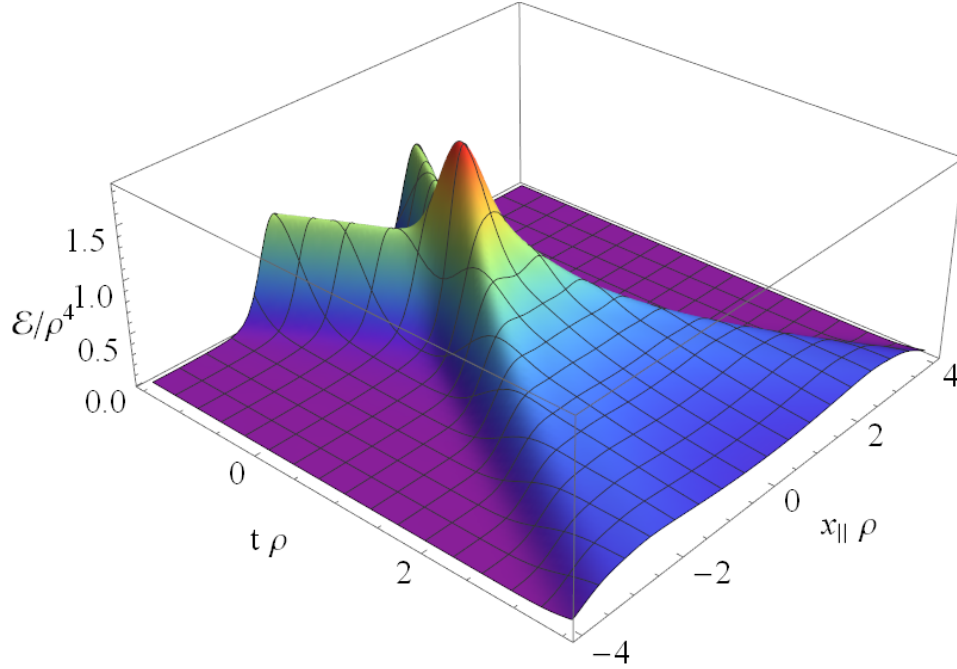
Figure 1.8: Rescaled energy density defined as $\mathcal{E} = (2\pi^2/N_c^2)T_{tt}$ in units of the maximum initial energy density on the shock-wave (ρ), in terms of t and $x_{\parallel}$. In the plot one can see the incoming projectiles, the collision, and the expanding debris in a typical pure gravity shock-wave collision. The waveform for the initial states is a gaussian with a with "1/2" in the language of [55].
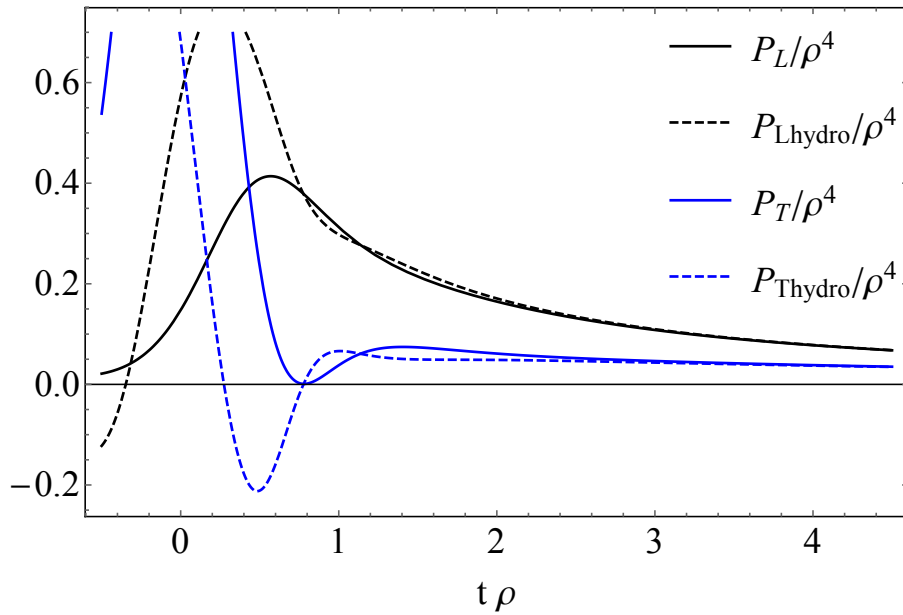
Figure 1.9: Plots for the longitudinal and transverse presures at mid rapidity over time (in units of ρ), and their hydrodynamic predictions. Short after the collision, hydrodynamics becomes a good description for the system's stress-energy tensor. Plots corresponding to the same pure gravity collision of fig. 1.8.

The first simulation by Chesler and Yaffe was quickly followed by other works that started exploring the potential of holographic collisions. For example, In refs. [55, 57], still in a pure gravity set-up, strong effects were observed in the resulting plasma depending on the waveform for the initial initial shock-waves (width and multiplicity of projectiles). Other studies of shock-waves include the exploration of different observables such as the entanglement entropy and 2-point functions [58], the study of coupling corrections as in [59], or the works appearing in this thesis where one considers set-ups beyond pure gravity.

In the following chapters we will present a set of works [1–5] focused on exploring the physics of holographic plasmas and shock-waves collisions in set-ups including more fields than the metric. A gauge field is added to the set-up in chapter 2 in order to add a conserved current in the dual plasma and capture the behaviour of the baryon current and its rapidity profile, experimentally accessible in the heavy ion colliders. The rest of the thesis is devoted to the study of non-conformal models and their dynamics. In chapter 3 a new model containing a scalar field is introduced to explore the physics of non-conformal systems, first for the homogeneous linear dynamics, and afterwards in chapter 4 to explore full dynamic shock-wave collisions. Finally, in chapter 5, we explore a model showing phase transitions and study the spinoidal instabilities present in it.

Chapter 2

Shock-wave collisions with baryon charge

Pure gravity simulations have provided valuable insights into the dynamics of strongly coupled gauge theories – presumably relevant to the QGP created in heavy ion collisions. Unfortunately, the amount of observables accessible in this kind of set-ups is very limited. The gravitational field in AdS encodes only the dynamics of the stress-energy tensor in dual gauge theory and, therefore, the dynamics of any additional conserved current are out of the reach of such set-ups. As a consequence, the collisions in pure gravity result in the formation of a baryon neutral plasma. Conversely, the plasma created in heavy ion collisions certainly carries some non-zero baryon charge. This charge increases in importance as the energy of the collision decreases (see fig. 1.3), making a case for a shock-wave simulation that includes it. There are, in addition, other motivations for such study. The baryonic chemical potential is a crucial ingredient for the critical phenomena of QCD and the extension of its phase diagram. Understanding its dynamics in the conformal case will certainly help in more complicated and realistic set-ups.

The goal of the work presented in this chapter is therefore to provide the first simulation of charged shock-wave collisions in AdS in order to model the formation and hydrodynamization of a QGP with a non-zero baryon charge. The conserved baryon current is dual on the gravity side to a Maxwell field, so we consider collisions in Einstein-Maxwell theory.

The numeric code used for the evolution of the shock-wave collisions presented in this chapter it is written in *Wolfram Mathematica* and is built upon the code used in [55, 57] for pure gravity collisions. The code uses the characteristic formulation, outlined in section 1.5.

2.1 The set-up

We start with the Einstein-Maxwell action with a negative cosmological constant by adding the term describing the electromagnetic field to (1.15),

$$S = -\frac{1}{16\pi G} \int d^5x \sqrt{-g} \left(\mathcal{R} + \frac{12}{L^2} - \frac{1}{4}e^2 L^2 \mathcal{F}_{mn}\mathcal{F}^{mn} \right) . \qquad (2.1)$$

Where G is Newton's constant, $\mathcal{R}$ is the Ricci scalar, L is the asymptotic AdS radius, e is a parameter controlling the backreaction of the Maxwell field on the metric, and $\mathcal{F}_{mn} \equiv \partial_{[m}A_{n]}$ is the electromagnetic field strength with A_m the vector potential. The metric and the gauge field are respectively dual on the gauge theory side to the stress tensor $T_{\mu\nu}$ and to a conserved $U(1)$ current J^μ whose time component one is free to think of as the baryon number density. In the case in which the action (2.1) is viewed as a consistent truncation of the dimensional reduction of type IIB supergravity on S^5 the dual gauge theory is $\mathcal{N} = 4$ Super Yang-Mills and the $U(1)$ current arises from the R-symmetry of this theory.[1] When we need to be concrete (for example to fix normalization factors) we will adopt this viewpoint. However, we emphasize that for most purposes the specific origin of the Maxwell field is unimportant and one could think of (2.1) simply as a bottom-up model that incorporates the minimal set of ingredients to describe the dynamics of the stress tensor and a conserved $U(1)$ current in the dual gauge theory.

The equations of motion following from (2.1) are

$$\mathcal{R}_{mn} + \frac{4}{L^2}g_{mn} = e^2 L^2 T_{mn} , \qquad (2.2)$$

$$\partial_m \left(\sqrt{-g}\mathcal{F}^{mn} \right) = 0, \qquad (2.3)$$

where

$$T_{mn} = \frac{1}{2}\mathcal{F}_{mp}\mathcal{F}_n{}^p - \frac{1}{12}g_{mn}\mathcal{F}^2 \qquad (2.4)$$

is the stress tensor sourced by the electromagnetic field. These equations admit the following analytic solution – in Fefferman-Graham coordinates – describing a charged

---

[1]The full five-dimensional action for this truncation would include a Chern-Simons term (see e.g. [60]), but this will play no role in our analysis and we have therefore omitted it.

shock wave moving at the speed of light:

$$ds^2 = \frac{L^2}{u^2}\left(- dx_+ dx_- + dx_\perp^2 + \left[u^4 h(x_+) - \frac{1}{3} e^2 u^6 a(x_+)^2 \right] dx_+^2 + du^2 \right), \qquad (2.5)$$

$$A = \frac{u^2}{L^2}\, a(x_+)\, dx_+\,, \qquad (2.6)$$

where $x_\pm = t \pm z$ and $h(x_+)$ and $a(x_+)$ are arbitrary functions of x_+. This solution is reminiscent of the pure gravity shock-wave metric, as only amounts to the addition of the $-\frac{1}{3} e^2 u^6 a(x_+)^2$ term in (1.19). Also, as in the pure gravity case, this metric ansatz is not suitable for starting a characteristic evolution, and will have to be numerically transformed to the Bondi-Sachs form.

In the case in which the dual theory is $\mathcal{N} = 4$ SYM the metric functions are related to the expectation values of the corresponding dual operators through [30]

$$\langle T_{++} \rangle = \frac{N_c^2}{2\pi^2} h(x_+)\,, \qquad (2.7)$$

$$\langle J_+ \rangle = \frac{N_c^2 e}{\pi^2} a(x_+)\,. \qquad (2.8)$$

The fact that J scales as N_c^2 reflects its R-symmetry origin, namely that microscopically it is built out of adjoint degrees of freedom. An analogous solution describing a wave moving in the opposite direction is obtained by replacing $x_+ \to x_-$ in the expressions above.

We will adopt the following choices for the functions h and a describing our incoming projectiles:

$$h(x_\pm) = \frac{m^3}{\sqrt{2\pi w^2}} \exp\left(-\frac{x_\pm^2}{2w^2} \right)\,, \qquad a(x_\pm) = h(x_\pm)/2m \qquad (2.9)$$

The energy and charge densities per unit area of the shock are $2\pi^2 m^3/N_c^2$ and $2\pi^2 m^2/N_c^2$, respectively. Note that we choose the centers and the widths of the Gaussian profiles for h and a to be the same, as corresponds to the fact that we want to model the collision of projectiles that carry both energy and charge.

We see from Eq. (2.2) that the parameter e controls the magnitude of the backreaction of the Maxwell field on the dynamics of the spacetime metric. It is clear from the action (2.1) that this parameter could be absorbed in the normalization of the Maxwell field, at the expense of including an explicit factor of e multiplying the gauge field amplitude

$a(x_+)$ in Eq. (2.6). In other words, one can either think of the backreaction as being controlled by e for a fixed incoming amplitude $a(x_+)$, or as it being controlled by the incoming amplitude for a fixed e. We find it convenient to adopt the first viewpoint.

The limit $e \to 0$ on the gravity side corresponds to an approximation in which the Maxwell field is treated as a probe field that propagates in a fixed background without affecting it. In the gauge theory this means that the charge density is treated in a quenched approximation in which it has a negligible effect on the dynamics of the gluons. This limit is physically interesting since it describes the situation in which the energy density dominates over the charge density, and also as a benchmark against which the backreacted results can be compared. In Sec. 2.4 we will consider the collision in the probe approximation, and in Sec. 2.5 we will consider the backreacted case.

2.2 Thermodynamics and hydrodynamics

We begin by reviewing the thermodynamics and transport properties of the plasma in the theory described by the action (2.1). This will be necessary later in sections 2.4 and 2.5 when we analyse the outcome of the collisions and the hydrodynamization process. We will work with a rescaled stress tensor and current

$$\mathcal{T}_{\mu\nu} = \frac{2\pi^2}{N_c^2} \langle T_{\mu\nu} \rangle \,, \qquad \mathcal{J}^{\mu} = \frac{2\pi^2}{N_c^2} \langle J^{\mu} \rangle \,, \qquad (2.10)$$

and set

$$\mathcal{E} = -\mathcal{T}_0^0 \,, \qquad \rho = \mathcal{J}^0 \,. \qquad (2.11)$$

The relation between these quantities and the temperature (T) and chemical potential (μ) can be obtained by studying the analytic solutions corresponding to homogeneous and static black branes in the set-up of study. This equilibrium solutions are known as the AdS-Reissner-Nordstrom black holes, and in Eddington-Finkelstein coordinates are given by the metric,

$$ds^2 = 2dtdr - \left(\frac{a_{(4)}}{r^2} + \frac{2A_{(2)t}^2 e^2}{3r^4} + r^2 \right) dt^2 + r^2 dx^i dx^j \,. \qquad (2.12)$$

In these coordinates, $a_{(4)}$ and $A_{(2)t}$ are constants that parametrize the family of static solutions, and coincide with the fall-off coefficients that will give the energy and charge densities of the dual theory. To obtain the temperatures and chemical potential corresponding to a particular solution one should follow the black hole thermodynamics prescriptions; the surface gravity for the temperature, and the integral of the electric field along a null geodesic for the chemical potential. For the one point functions of the stress-energy tensor and the conserved current we use the holographic renormalization prescriptions,

$$\mathcal{T}_{\mu\nu} = g_{(4)\mu\nu}\,, \qquad \mathcal{J}^{\mu} = e\,\mathcal{F}^{r\mu}_{(3)} \tag{2.13}$$

where $g_{(4)\mu\nu}$ is the fourth term in the Fefferman-Graham expansion of the metric (as defined in (1.7)), and $\mathcal{F}^{r\mu}_{(3)}$ is the third term in the electromagnetic tensor expansion.

Working out the black hole surface gravity, the thermodynamics is given by the following expressions (see e.g. [61]):

$$\mathcal{E} \;=\; \frac{3}{4}\,x^4\left(1+\sqrt{1+\frac{1}{6}\,y^2}\right)^3\left(3\sqrt{1+\frac{1}{6}\,y^2}-1\right), \tag{2.14}$$

$$\rho \;=\; \frac{1}{2}\,x^3\,y\left(1+\sqrt{1+\frac{1}{6}\,y^2}\right)^2, \tag{2.15}$$

where

$$x = \frac{\pi T}{2}\,, \qquad y = \mu/x\,. \tag{2.16}$$

Using these expressions one can show that, for a small charge density, the chemical potential is given by

$$\mu \simeq \frac{\sqrt{3}\rho}{\sqrt{\mathcal{E}}}\left[1+\frac{\sqrt{3}}{4}\left(\frac{\rho}{\mathcal{E}^{3/4}}\right)^2+\cdots\right]. \tag{2.17}$$

We see that, for fixed energy density, μ and ρ are linear in one another with a 1% (10%) accuracy if $\rho/\mathcal{E}^{3/4}$ is no larger than 0.15 (0.48). In the opposite limit, when the chemical potential is high compared to the temperature, $y \gg 1$, we have that

$$\mathcal{E} \simeq \frac{\pi^4}{2^8}\,\mu^4\,, \qquad \rho \simeq \frac{\pi^3}{3\cdot 2^5}\,\mu^3\,, \tag{2.18}$$
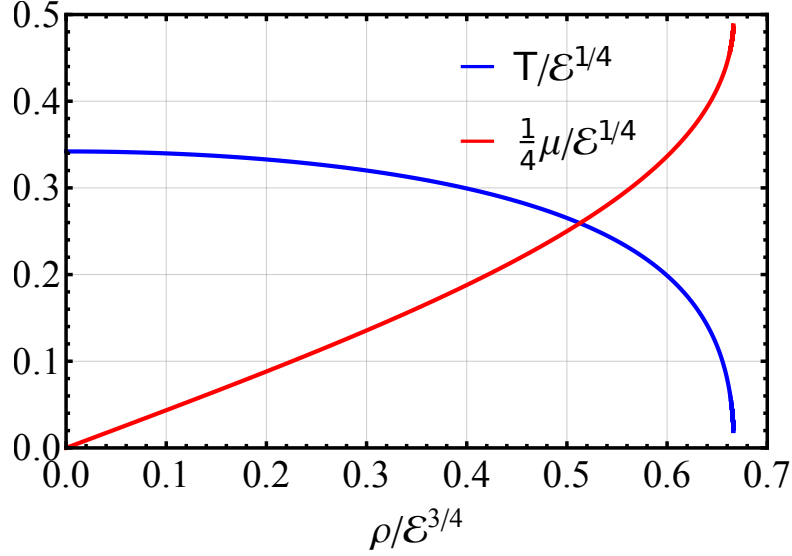
Figure 2.1: Temperature and chemical potential as a function of the charge density, all normalized by the energy density.

and the ratio of charge to energy density approaches the value

$$\frac{\rho_{max}}{\mathcal{E}^{3/4}} = \frac{2}{3}\,. \tag{2.19}$$

The subindex 'max' indicates that this is the maximum value of ρ for a fixed energy density. At this value the black brane becomes extremal and the temperature approaches zero compared to any other scale. Above this value a naked singularity appears. These features are illustrated in Fig. 2.1.

Charged hydrodynamics for $\mathcal{N} = 4$ SYM has been studied extensively [61, 62]. In the case of a 1+1 dimensional flow, as is of interest here, the constitutive relations take the form

$$\mathcal{T}_{\mu\nu} = \mathcal{E}\, u_\mu u_\nu + P(\mathcal{E})\Delta_{\mu\nu} - \eta\,\sigma_{\mu\nu}\,, \tag{2.20}$$

$$\mathcal{J}_\mu = \rho\, u_\mu - \kappa\,\Delta_\mu^\nu \partial_\nu \left(\frac{\mu}{T}\right)\,, \tag{2.21}$$

where

$$\Delta_{\mu\nu} = g_{\mu\nu} + u_\mu u_\nu\,, \tag{2.22}$$

$$\sigma_{\mu\nu} = \Delta^{\mu\alpha}\Delta^{\mu\beta}\left(\nabla_\alpha u_\beta + \nabla_\beta u_\alpha\right) - \frac{2}{3}\Delta^{\mu\nu}\Delta^{\alpha\beta}\nabla_\alpha u_\beta\,, \tag{2.23}$$

and the transport coefficients (rescaled by $2\pi^2/N_c^2$) are

$$\eta \;=\; \frac{1}{4}\,x^3\left(1+\sqrt{1+\frac{1}{6}\,y^2}\,\right)^3 , \tag{2.24}$$

$$\kappa \;=\; \frac{2}{\pi}\,x^2\left(1+\sqrt{1+\frac{1}{6}\,y^2}\,\right)\left(3\sqrt{1+\frac{1}{6}\,y^2}-1\right)^{-1} . \tag{2.25}$$

We note that, although the ratio η/s remains constant at the pure gravity value $(1/4\pi)$, η itself will depend on the temperature and chemical potential in a non-trivial fashion.

2.3 Dynamic equations and algorithm

As it is done in the pure gravity case, to obtain the dynamic equations for the system in a characteristic form, one needs to plug the Bondi-Sachs ansatz for the metric (1.18) into the dynamic equations (2.2)-(2.3). Additionally, one also needs to provide an ansatz for the gauge field. The most general electromagnetic tensor preserving the $2+1$ symmetry is simply,

$$\mathcal{F} = \mathcal{F}_{rt}dr \wedge dt + \mathcal{F}_{rz}dr \wedge dz + \mathcal{F}_{tz}dt \wedge dz , \tag{2.26}$$

where r is the holographic coordinate, t the null time, and $z = x_\parallel$ the direction of the collision.

To start a characteristic evolution it is only necessary to specify the initial state for some of the dynamic variables. Unfortunately, the shock-wave solution (2.5) is only known analytically in the Fefferman-Graham frame, so a coordinate change is needed. There are several equivalent ways to compute the coordinate change. In particular we use the fact that the $u = 1/r$ coordinate in the Eddington-Finkelstein frame generates ingoing null geodesics, so one can use the geodesic equations to find them. This method has been previously used in the literature, and is more extensively explained in chapter 4, where shock-waves in non-conformal models are discussed.

Thanks to the Bondi-Sachs coordinates, the resulting equations are ultra-local in the longitudinal direction. Unfortunately, the inclusion of a gauge field partially spoils the linearity and nestedness of the system when $e \neq 0$. These features are recovered at the probe limit, where the equations for the metric evolution smoothly connect with the ones

of the pure gravity set-up. The Einstein-Maxwell equations with backreaction read,

$$3SS'' = e^{2B}\left(-e^2\right)\mathcal{F}_{rz}^2 - \frac{3}{2}S^2\left(B'\right)^2 \tag{2.27a}$$

$$S^2 F'' = S\left(6\tilde{S}B' + 4\tilde{S}' + 3F'S'\right) + S^2\left(3\tilde{B}B' + 2\tilde{B}'\right) - 4\tilde{S}S'$$
$$- 2e^2\mathcal{F}_{rt}\mathcal{F}_{rz}S^2 \tag{2.27b}$$

$$S^3\mathcal{F}_{rt}' = -e^{2B}\left(\mathcal{F}_{rz}\left(S\left(2\tilde{B} - F'\right) + \tilde{S}\right) + S\tilde{\mathcal{F}}_{rz}\right) - 3\mathcal{F}_{rt}S^2 S' \tag{2.27c}$$

$$12S^3\dot{S}' = e^{2B}\left(S^2\left(4\tilde{B}F' - 7\tilde{B}^2 - 4\tilde{\tilde{B}} + 2\tilde{F}' + \left(F'\right)^2\right) + 2S\left(\tilde{S}\left(F' - 8\tilde{B}\right) - 4\tilde{\tilde{S}}\right)\right.$$
$$\left. + 4\tilde{S}^2\right) + S^4\left(24 - 2e^2\mathcal{F}_{rt}^2\right) - 24\dot{S}S^2 S' \tag{2.27d}$$

$$6S^4\dot{B}' = e^{2B}\left(-S^2\tilde{B}F' + S^2\tilde{B}^2 + S^2\tilde{\tilde{B}} + S\tilde{B}\tilde{S} + 4S\tilde{S}F' - 2S^2\tilde{F}' + 2S\tilde{\tilde{S}} - 4\tilde{S}^2\right.$$
$$\left. - S^2\left(F'\right)^2 + 2Ae^2\mathcal{F}_{rz}^2 S^2 + 4e^2 F\mathcal{F}_{rt}\mathcal{F}_{rz}S^2 + 4e^2\mathcal{F}_{rz}\mathcal{F}_{tz}S^2\right)$$
$$- 9S^3\left(\dot{S}B' + \dot{B}S'\right) \tag{2.27e}$$

$$6S^4 A'' = e^{2B}\left(21S^2\tilde{B}^2 + 12S^2\tilde{\tilde{B}} + 48S\tilde{B}\tilde{S} + 24S\tilde{\tilde{S}} - 12\tilde{S}^2 - 2Ae^2\mathcal{F}_{rz}^2 S^2\right.$$
$$\left. - 4e^2 F\mathcal{F}_{rt}\mathcal{F}_{rz}S^2 - 4e^2\mathcal{F}_{rz}\mathcal{F}_{tz}S^2 - 3S^2\left(F'\right)^2\right) + 72\dot{S}S^2 S'$$
$$+ 2S^4\left(-9\dot{B}B' + 7e^2\mathcal{F}_{rt}^2 - 12\right) \tag{2.27f}$$

$$4S^3\mathcal{F}_{tz}' = S^2\left(-2S\left(\tilde{\mathcal{F}}_{rt} + \mathcal{F}_{rz}\left(A' + AB' + 2\dot{B}\right) + A\mathcal{F}_{rz}' + 2B'(F\mathcal{F}_{rt} + \mathcal{F}_{tz}) + \mathcal{F}_{rt}F'\right)\right.$$
$$\left. + S'(-A\mathcal{F}_{rz} + 10F\mathcal{F}_{rt} - 2\mathcal{F}_{tz}) - 2\mathcal{F}_{rz}\dot{S}\right)$$
$$+ 4e^{2B}F\left(\mathcal{F}_{rz}\left(S\left(2\tilde{B} - F'\right) + \tilde{S}\right) + S\tilde{\mathcal{F}}_{rz}\right) \tag{2.27g}$$

$$4\dot{\mathcal{F}}_{rz}S = -2S\left(-\tilde{\mathcal{F}}_{rt} + \mathcal{F}_{rz}\left(A' + AB' + 2\dot{B}\right) + 2B'(F\mathcal{F}_{rt} + \mathcal{F}_{tz}) + \mathcal{F}_{rt}F'\right)$$
$$- S'(A\mathcal{F}_{rz} + 2F\mathcal{F}_{rt} + 2\mathcal{F}_{tz}) - 2\mathcal{F}_{rz}\dot{S} \tag{2.27h}$$

where $f = f[r,t,z]$, $\tilde{f} = \partial_z f - F\partial_r f$, $\dot{f} = \partial_t f + (A/2)\partial_r f$, and $f' = \partial_r f$.

Analogously to the pure gravity case, one only needs to specify B and now $\mathcal{F}_{rz}$ at the initial time slice to start integrating the semi-nested scheme (2.27). The outcome of this scheme are precisely the time derivatives $\partial_t B$ and $\partial_t \mathcal{F}_{rz}$ with which one can evolve the geometry to following time step. Additionally to the equations, one also needs to provide boundary conditions at the AdS boundary. These are formally given by the order by order solution of the dynamic equations close to the boundary in terms of the fall-off coefficients, which are evolved independently using the conservation equations. Overall, the algorithm used to evolve the Einstein-Maxwell equations is very similar to the ones

used for other shock-wave collisions. In the present case we used a Chebyshev spectral grid in the u direction and a periodic Fourier grid in the z direction. In the latter the derivatives can be performed using the full spectral matrix or, alternatively, an n-point finite differencing one.

In order to solve the equations using the spectral methods, one needs a compact domain between the AdS boundary and the apparent horizon. To obtain it, it is convenient to use the coordinate $u = 1/r$ as a holographic coordinate. Additionally, one needs to regularize the dynamic functions, as these diverge in a known fashion close to $u = 0$. From the order by order solution we obtain the finite functions,

$$Bf[u,t,z] = \frac{B[u,t,z]}{u^4} \tag{2.28a}$$

$$\mathcal{F}_{ry}f[u,t,z] = \frac{\mathcal{F}_{ry}[u,t,z]}{u^3} \tag{2.28b}$$

$$Sf[u,t,z] = \frac{uS[u,t,z] - u\xi[t,z] - 1}{u^5} \tag{2.28c}$$

$$Ff[u,t,z] = \frac{F[u,t,z] - \partial_z\xi[t,z]}{u^2} \tag{2.28d}$$

$$\mathcal{F}_{rt}f[u,t,z] = \frac{\mathcal{F}_{rt}[u,t,z]}{u^3} \tag{2.28e}$$

$$\dot{S}f[u,t,z] = -\frac{(u\xi[t,z] + 1)^2 - 2u^2\dot{S}[u,t,z]}{2u^4} \tag{2.28f}$$

$$\dot{B}f[u,t,z] = \frac{\dot{B}[u,t,z]}{u^3} \tag{2.28g}$$

$$Af[u,t,z] = \frac{u^2 A[u,t,z] + 2u^2\partial_t\xi[t,z] - (u\xi[t,z] + 1)^2}{u^4} \tag{2.28h}$$

$$\mathcal{F}_{ty}f[u,t,z] = \frac{\mathcal{F}_{ty}[u,t,z]}{u^2} \tag{2.28i}$$

$$\dot{\mathcal{F}}_{ry}f[u,t,z] = \frac{\dot{\mathcal{F}}_{ry}[u,t,z]}{u^2} \tag{2.28j}$$

$$\dot{F}f[u,t,z] = \frac{\dot{F}[u,t,z] - \partial_t\partial_z\xi[t,z]}{u} \tag{2.28k}$$

Where we have set the AdS radius $L = 1$ for convenience. The equations for the redefined fields can be trivially obtained by substituting the full functions in (2.27) by their expressions in terms of the finite ones.

2.4 The probe approximation

With the initial conditions (2.9) for the collision we can solve the Einstein-Maxwell equations, as outlined in [42, 63]. In this section we work in the strict probe approximation for the Maxwell field, where the Einstein's and Maxwell's equations completely decouple and all them are linear. We are therefore computing the evolution of a Maxwell field on top of the dynamical shock wave collisions studied earlier in [42, 54, 55, 57, 63, 64]. Computationally it is however convenient to evolve both the metric and the Maxwell field at the same time, thereby recomputing the gravitational shock wave background. This is equivalent to setting $e = 0$ in (2.27) and reordering the equations to solve first for the metric coefficients and then for the electromagnetic tensor components.

We performed simulations for $mw = 0.1$ (1/4-shocks in the language of [55]) and $mw = 1.9$ (2-shocks in the language of [55]), which we will refer to as thin and thick shock collisions, respectively. The resulting charge density ρ is plotted in Fig. 2.2 for both cases, whereby we included the energy density $\mathcal{E}$ for comparison (also found in [55]). Clearly in the thin regime the shocks gradually lose their charge into a charged plasma between the shocks, much like the energy density. For the thick shocks the energy density already hydrodynamizes during the collision regime [55] and, as we will see below, the same is true for the charge density. The shape of the charge and energy densities is different, a feature which we will later analyze in the local rest frame as well. One interesting feature is the decay of the original shocks in the thin regime. Indeed, we see that on the attenuating maxima the charge density exactly follows the energy density, despite the fact that the charge and the energy are distributed differently in between the shocks. This agreement on the attenuating maxima is remarkable in view of the fact that the energy and the charge are governed by in principle completely different dynamics, i.e. the Einstein equations and the Maxwell equations on a fixed background, respectively. This suggests that on the light cone a simplified picture may be possible (perhaps along the lines of [65]).

2.4.1 Hydrodynamization

Having the complete stress-tensor we are able to extract the energy and charge density in the local rest frame, defined through

$$T_\mu^\nu u_\nu = -\mathcal{E}_{loc}\, u_\mu \,, \tag{2.29}$$
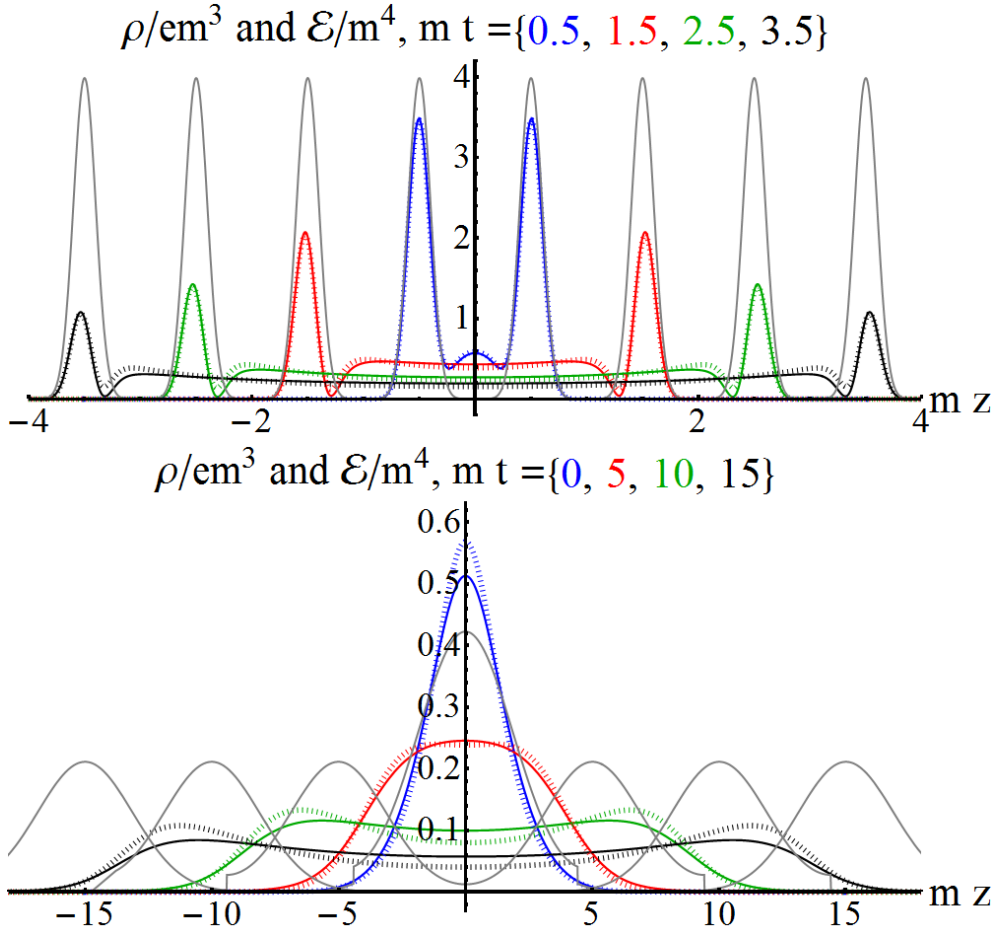
Figure 2.2: Snapshots of the charge density (solid curves) and energy density (dotted curves) for thin (top) and thick (bottom) collisions. The grey curves indicate the charge density of the unperturbed original shocks.

from which we find

$$
\mathcal{E}_{loc} = \frac{1}{2} \left(\sqrt{(\mathcal{T}^{zz} + \mathcal{T}^{tt})^2 - 4(\mathcal{T}^{tz})^2} - \mathcal{T}^{zz} + \mathcal{T}^{tt} \right),
$$

$$
v_{loc} \equiv \frac{u_z}{u_t} = \frac{\mathcal{T}^{zz} + \mathcal{T}^{tt} - \sqrt{(\mathcal{T}^{zz} + \mathcal{T}^{tt})^2 - 4(\mathcal{T}^{tz})^2}}{2\mathcal{T}^{tz}}, \tag{2.30}
$$

where u_μ is the (timelike) fluid velocity. For the charge density we have

$$
\rho_{loc} = J_\mu u^\mu. \tag{2.31}
$$

This allows us to study the approach to charged hydrodynamics. We read off from our simulations the fluid velocity and the energy and charge densities. We then use

the constitutive relations (2.20)-(2.21) to obtain the hydrodynamic prediction for the transverse and longitudinal pressures, P_L^{hyd} and P_T^{hyd}, and for the time component of the current, J_t^{hyd}. We define the hydrodynamization time for the stress tensor, t_{hyd}, as the time beyond which

$$\frac{3\left|P_L - P_L^{hyd}\right|}{\mathcal{E}} < 0.1 \,. \tag{2.32}$$

Similarly, we define the hydrodynamization for the current, t_{hyd}^J, as the time beyond which

$$\frac{\left|J_t - J_t^{hyd}\right|}{\rho} < 0.1 \,. \tag{2.33}$$

A crucial difference between the hydrodynamization of the stress tensor versus the charge current is that the pressures at $z = 0$ can deviate from their hydrodynamic values due to the gradients of the velocity field. In contrast, parity symmetry implies that u has no spatial component at $z = 0$ and that J_z vanishes identically. As a consequence, the (ideal) hydrodynamic prediction for the current is always exact at mid-rapidity. In order to asses the validity of the hydrodynamic description for J we will therefore look at non-zero rapidity.

The hydrodynamization times for the stress tensor in the case of a neutral fluid were determined in Refs. [54, 55, 64]. The result is

$$mt_{\mathrm{hyd}} = \{2.0, 2.4, 3.6\} \qquad \text{at} \qquad mz = \{0, 1.5, 3.0\} \qquad \text{for thin shocks}\,, \tag{2.34}$$
$$mt_{\mathrm{hyd}} = \{2.1, 4.7, 16\} \qquad \text{at} \qquad mz = \{0, 5, 15\} \qquad \text{for thick shocks}\,. \tag{2.35}$$

Since in this section we are working in the probe approximation, these times agree with our hydrodynamization times. With our new simulations we can now also study the hydrodynamization of the charge current, whose evolution and hydrodynamic approximations are shown in Fig. 2.3. The hydrodynamization times are

$$mt_{\mathrm{hyd}^J} = \{2.0, 3.5\} \qquad \text{at} \qquad mz = \{1.5, 3.0\} \qquad \text{for thin shocks}\,, \tag{2.36}$$
$$mt_{\mathrm{hyd}^J} = \{0, 0\} \qquad \text{at} \qquad mz = \{5, 15\} \qquad \text{for thick shocks}\,. \tag{2.37}$$

In the case of thick shocks we have listed the value $t_{hyd}^J = 0$ to indicate that the current is always well predicted by hydrodynamics. In contrast, for thin shocks we see that
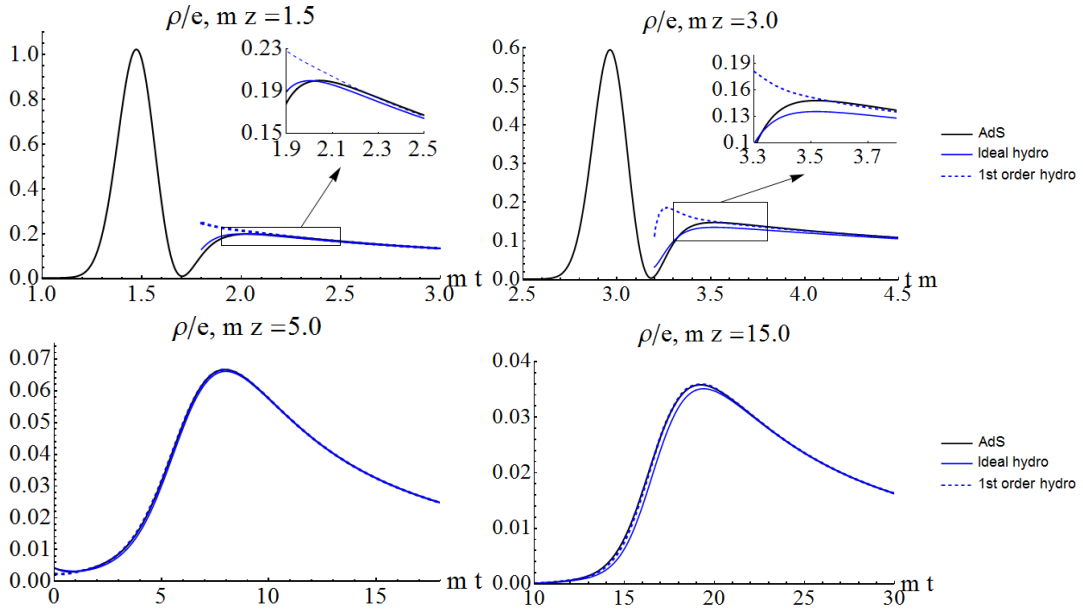
Figure 2.3: Time component of the current J_t (black, solid curve) and its approximations based on ideal (blue, solid curve) and viscous (blue, dashed curve) hydrodynamics, for thin (top row) and thick (bottom row) shocks. The hydro curves start at a time after which a local rest frame can be defined (as in [66]). The insets show that even though ideal hydrodynamics gives a better overall fit in the range plotted, viscous hydrodynamics gives a better description of the final approach to hydrodynamics. Thick shocks (bottom) are always well described by charged hydrodynamics, whereby viscous hydrodynamics gives a significant improvement.

the hydrodynamization times for the current away from mid-rapidity are very similar to those for the stress tensor. In both cases, after t_{hyd}^J there is a small but significant difference between ideal and viscous hydrodynamics, which shows that the fluid velocity of the charge differs from the velocity of the energy-momentum flow.

2.4.2 Rapidity profiles and charge deposition

Fig. 2.4 shows the spacetime rapidity profile of the local charge density.   This is compared
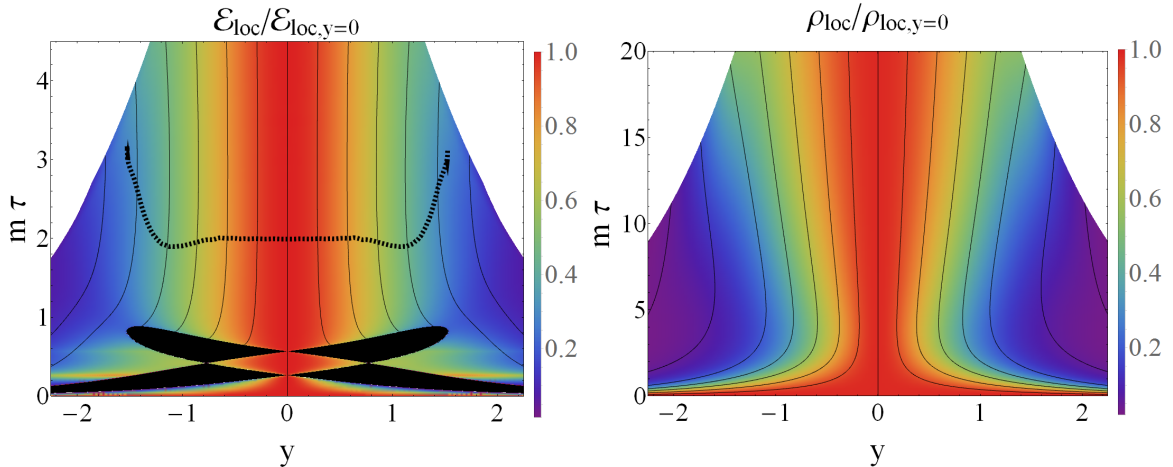
Figure 2.4: Local charge density as a function of proper time τ and rapidity y. The left plot shows the rapidity distribution for thin shocks, where regions without a rest frame are drawn black [66], and the hydrodynamic region is indicated by the dashed line (according to (2.32)). The upper white regions are outside our numerical grid. The right plot is for thick shocks, which is always in the hydrodynamic regime for $\tau > 2$. The black lines are stream lines of the fluid velocity, which are similar to the charge velocity.

with the local energy density rapidity profile for several different proper times in Fig. 2.5. Especially striking in Fig. 2.5 is the development of maxima at non-zero rapidity for the charge profile; we will come back to this in the Discussion section. This happens fast in the case of thin shocks, whereas it takes longer for thick shocks. Furthermore, we see that for thin shocks the evolution of the charged rapidity profile is expanding much faster than the equivalent profile for the local energy density. For thick shocks both profiles expand at a similar rate.

To characterize the charge deposition after the collision, we compare the charge density in the local rest frame, ρ_{loc}, to the local energy density, $\mathcal{E}_{loc}$. More precisely, at
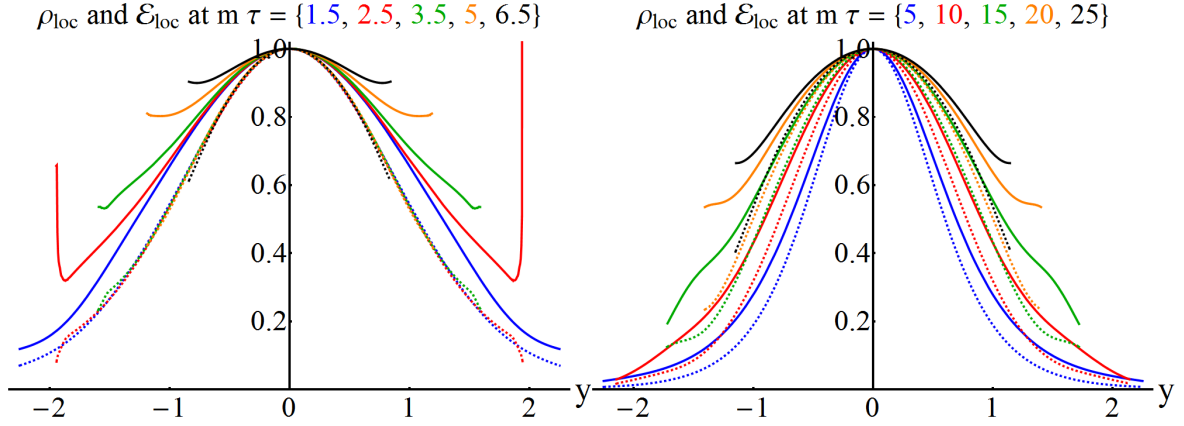
Figure 2.5: Rapidity profile of the local charge (solid curves) and the local energy (dashed curves) densities at different proper times τ as a function of rapidity y and normalized at mid-rapidity (see also [55, 63, 64] for similar plots of the energy density). For thin shocks the energy density does not evolve much on the times shown, whereas the profile for the charge density widens significantly. For thick shocks the charge and energy profiles widen in a similar fashion, though the profile of the charge is always wider.
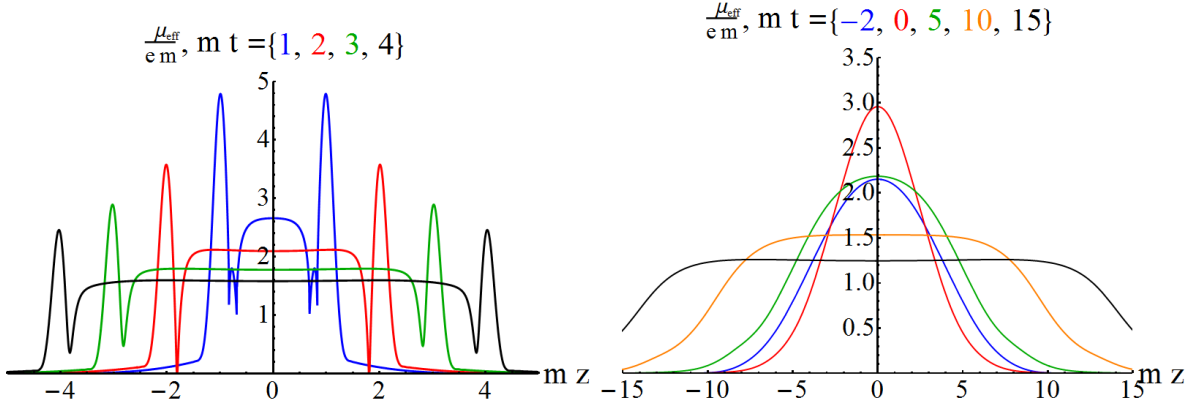
Figure 2.6: Chemical potential for thin (left) and thick (right) shock collisions.

all points in spacetime at which a local rest frame exists, we define the ratio

$$\mu_{eff} \equiv \sqrt{3}\rho_{loc}/\mathcal{E}_{loc}^{1/2} \, . \tag{2.38}$$

The significance of this ratio, which we plot in figure 2.6, is that, in equilibrium, μ_{eff} coincides with the small-charge limit of chemical potential of the plasma, eq. (2.17). We will come back to figure 2.6 in the Discussion section.

When colliding shocks with symmetric energy and charge distributions it is impossible to determine which part of the energy and charge in the final plasma comes from the
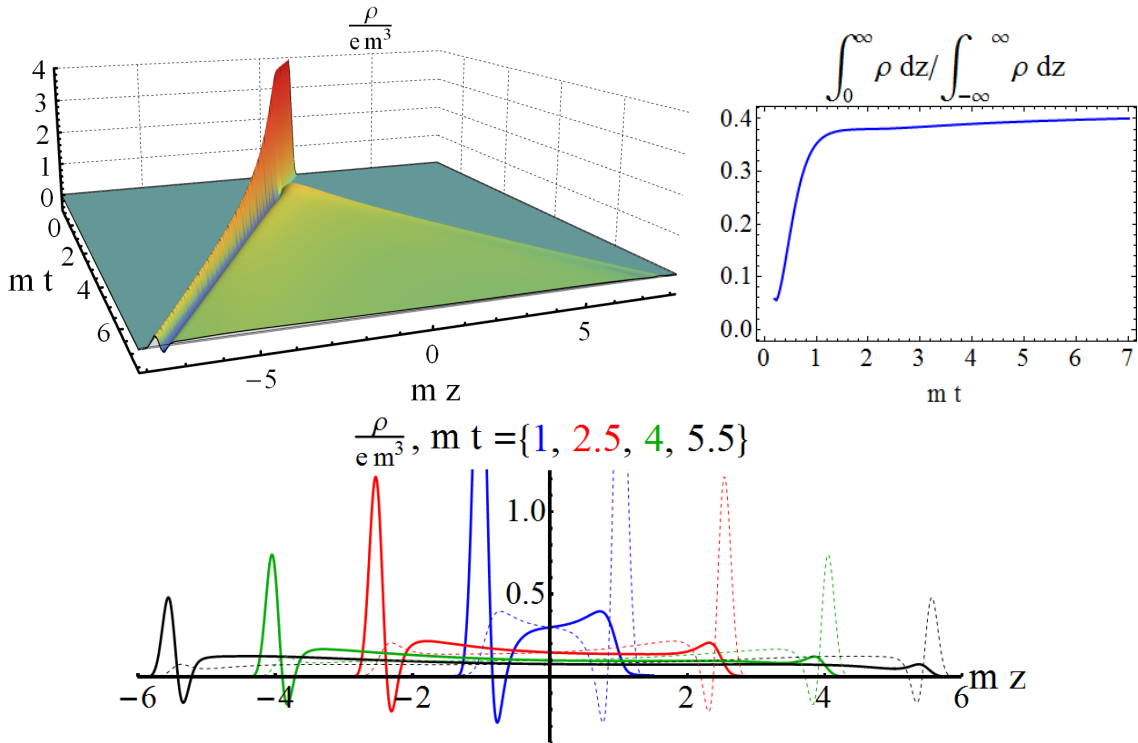
Figure 2.7: We present the charge density ρ for a $mw = 0.1$ collision where only the left-moving shock is charged, with a 3D plot (top-left), snapshots with dashed lines showing a reflection (bottom) and with the fraction of the charge ending up at $z > 0$ as a function of time (top-right). Interestingly, even though the initial charge moves towards negative z at the speed of light the collision causes about 41% ends up at positive z, indicating very strong interactions.

left- or right-moving shock. In our current set-up, however, it is possible to charge only the left-moving shock, leaving the right-moving shock neutral. This results in a charge distribution as shown in Fig. 2.7.[2] Clearly most of the charge ends up at $z < 0$, but at later times a surprisingly large fraction of about 41% ends up at $z > 0$, indicating that the strong interactions of the collision can indeed let the charge density bounce back, reflecting the direction of 41% of the charge.

Quite interestingly, the right-moving charge contains a bump moving close to the speed of light, though not as fast as the left-moving shock moving at the speed of light. This bump, however, does not come with a minimum with negative charge density, indicating that the negative charge density has to be associated to the presence of the original shock on the light cone. We verified that the profile away from the original

---

[2]Note that without backreaction the charge of the colliding shocks does not interact with itself; the charge profile of the symmetric collision is hence equal to the sum of the dashed and solid lines in Fig. 2.7.

shock is independent of the width of the charge, in agreement with the findings in [57]. Experimentally, these simulations have potential consequences when it is possible to vary the baryon charge while leaving the energy constant. This can for instance be done by comparing proton with antiproton collisions, or deuteron collisions with proton collisions of double the energy (preferably selected such that the deuteron is aligned along the beam direction).

2.5 Charge backreaction

We move away from the probe limit and include the full back-reaction of the charge density. In the $e \neq 0$ case the computation becomes somewhat more challenging: the first equation of the scheme (2.27) is now non-linear and one needs to implement a Newton relaxation on the spectral grid in order to solve it. A useful trick to speed up the computation is to use the solution obtained in the previous time step as a seed for the relaxation. In most of cases, a single iteration of the Newton method will be enough to find the solution with the desired tolerance. A second drawback arisen from the inclusion of backreaction is the non-nestedness of the rest of the equations: the equations appear in two groups of two and three coupled equation systems. Although coupled, the equations remain linear and therefore can be solved using (larger) spectral matrices. As the matrix inversion algorithm does not scale with the number of points, the computation is slowed down an overall 20%.

We find that, for a given width of the incoming shocks, there is a maximum value of e that our code is able to evolve. One clear physical reason why there is such a maximum value is that the charged plasma formed after the collision has to have a smaller charge density than the maximum density set by Eq. (2.19), and indeed our simulations reach as high as 80% of the maximum value according to the instantaneous energy density. On the other hand, this maximum value is also sensitive to the performance of the numerical code and furthermore depends sensitively on the initial separation of the shocks. The latter may be an indication that single charged shock waves cannot be evolved in a stable manner by themselves. Nevertheless, choosing initial conditions with the shocks close enough to each other determines well-defined initial conditions, which shows us the effect of the back reaction of the charge on the metric. In a nutshell, the conclusions from these simulations are that (i) the effect of the charge on generic observables is relatively small, and (ii) this effect scales approximately linearly with e^2. We emphasize that these

results are non-trivial since the charge density attains values well into what is expected to be the non-linear regime based on Eq. (2.17).

To illustrate these results, in Fig. 2.8 we compare the energy density at mid-rapidity as a function of time for collisions with identical initial conditions but different values of e. The first row shows the energy density itself, whereas the second row shows the
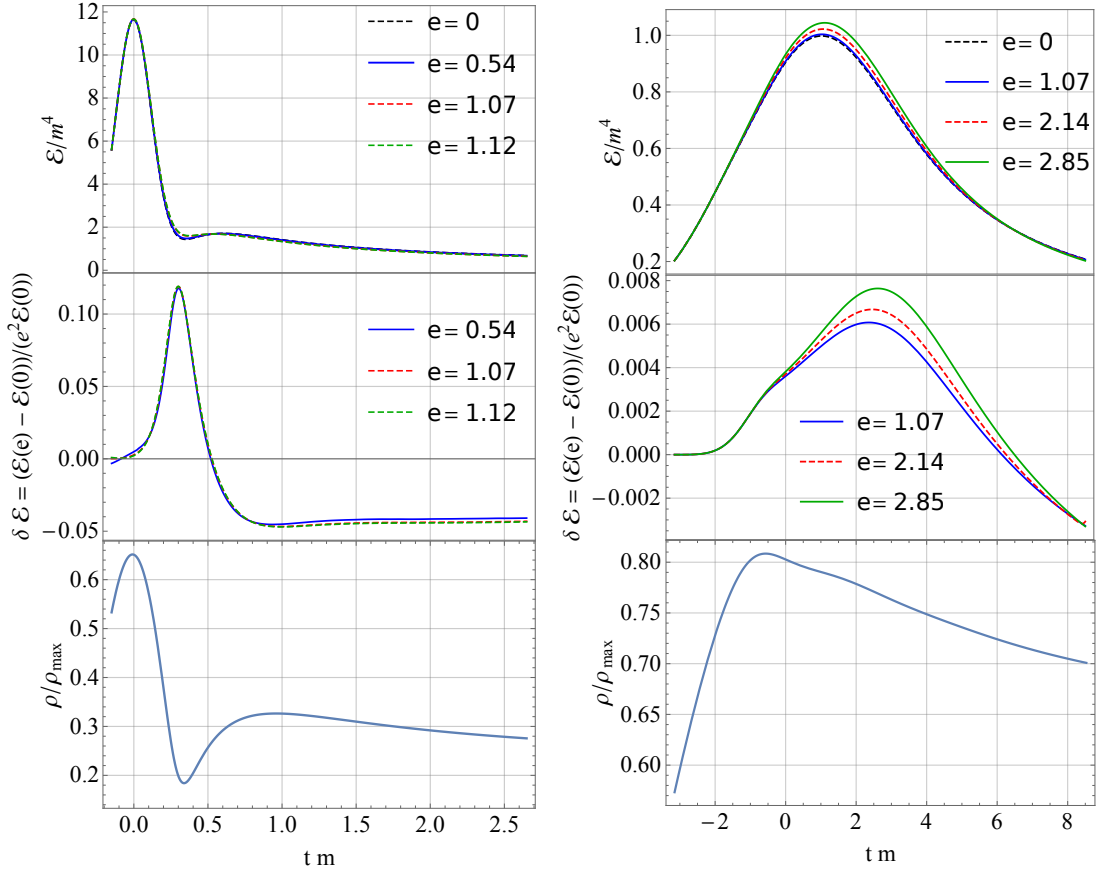
Figure 2.8: Backreaction of the charge as a function of time. The first row shows the energy density at mid-rapidity as a function of time for collisions with different values of e or, equivalently, different amounts of charge on the initial shocks, for thin (left) and thick (right) shocks. The second row is the relative difference between a given collision and a collision with the same initial energy density but zero charge. The third row shows the charge density as function of time in units of $2\mathcal{E}^{3/4}/3$ at that time (see Eq. (2.19)).

relative difference between a given collision and the $e = 0$ collision, normalized by e^2. The maximum value of the curves on the second row tells us that the maximum effect of the backreaction is about $0.12 \times 1.12^2 \simeq 15\%$ for thin shocks and $0.0075 \times 2.85^2 \simeq 6\%$ for thick shocks. The fact that the curves on the second row fall almost on top of each other for thin shocks (left) means that in this case the backreaction of the charge is almost

exactly linear in e^2. For thick shocks the deviations from linearity are slightly larger. Note that in both cases the charge density as a function of time is not small. Indeed, for thin shocks it initially exceeds 60% of the would-be maximum value according to the instantaneous energy density and drops to around 30% at later times. For thick shocks the maximum exceeds 80% and the curve drops to 70% at later times. Fig. 2.9 shows the same information as Fig. 2.8 but as a function of z at a constant time t_0. In the case of thin shocks we have chosen $t_0 = t_{hyd}$, whereas in the case of thick shocks t_0 is the time at which the green curve in the second row of Fig. 2.8 attains its maximum.
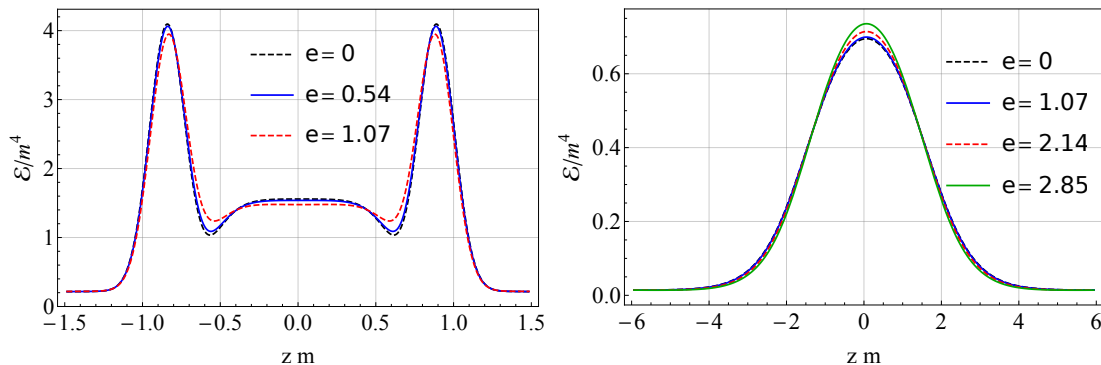
Figure 2.9: Backreaction of the charge as a function of z. We show the energy density at $t = t_0$ as a function of z for collisions with different values of e or, equivalently, different amounts of charge on the initial shocks, for thin (left) and thick (right) shocks. The time t_0 is equal to t_{hyd} for thin shocks and equal to the time at which the green curve in the second row of Fig. 2.8 attains its maximum for thick shocks.

As expected from this discussion, the effect of the charge density on the hydrodynamization time of the stress tensor is relatively small. For example, we find that for collisions with $mw = 0.1$ the hydrodynamization time in the charged case, with $e = 1.07$, is 3% shorter than in the neutral case. Instead, for collisions with $mw = 0.75$ the hydrodynamization time in the charged case, with $e = 1.7$, is 6% longer than in the neutral case.

2.6 Discussion

We have studied collisions of charged shocks in AdS_5. Via the gauge/gravity duality, these are dual in the gauge theory to collisions of lumps of energy carrying fixed amounts of baryon charge (per unit area). As discussed in [55], the dynamics of the stress tensor show qualitatively different features depending on the width of the colliding shocks. In this

paper we have shown that similar qualitative differences also appear in the distribution of baryon charge after the collision. One of the main observations of [55] was that, while thick shocks lead to a complete stopping of the incident energy followed by a subsequent hydrodynamic evolution, narrow shocks exhibit a transparent regime at early times in which the initial shocks cross each other depositing their energy gradually as time progresses. In this paper we have shown that the baryon charge deposition exhibits identical behaviour, as illustrated in Fig. 2.2.

This transparent regime is transient, meaning that at a sufficiently late time the receding shock fragments are completely absorbed by the plasma. Nevertheless, the space-time rapidity distribution of baryon charge exhibits interesting diverse features for the two cases we have explored, as shown in Fig. 2.4. At fixed proper times, both for thick and thin shocks the charge distribution is wider in rapidity than the energy distribution. This means that, as rapidity grows, the plasma becomes more baryon rich, as illustrated by the increase in the chemical potential plotted in Fig. 2.6. However, for thin shocks the deposition of charge is wider than for thick shocks and it evolves much faster with time. Quite remarkably, for thin shocks the initial close-to-Gaussian charge distribution at early times, prior to hydrodynamisation, changes quickly to an almost-flat distribution in space-time rapidity which, within our limited numeric range, hints at the formation of maxima at relatively large rapidity, $y > 1$. In the range of proper times and rapidities covered by our simulations, see Fig. 2.5, these structures appear in regions in which the evolution is well described by hydrodynamics. However, the formation of these maxima may involve far-from-equilibrium dynamics that the hydrodynamic regions are in causal contact with. For thin shocks at very late times, the large rapidity region also develops local minima close to the edge of the rapidity coverage, which arise solely from the hydrodynamic evolution of the plasma.

The space-time rapidity profile of the charge distribution hence indicates that collisions of shock waves lead to a significant stopping of the baryon charge of the incident projectiles. To best illustrate this point it is instructive to determine the fraction of the total charge (per unit area) of the incident shocks that is deposited between momentum rapidity $y_p = -1$ and $y_p = 1$, with $y_p = \operatorname{arctanh}(v_z)$ and v_z the velocity field in the collision direction. This is determined by integrating the charge between the two points where the fluid velocity reaches $v_z = \tanh(1) \approx 0.76$, divided by the total charge. We show this quantity as a function of time in Fig. 2.10 for both thin and thick shocks.

For thick shocks, the mid-rapidity charge fraction is bigger than for the thin shocks, which implies that the charge distribution is narrower in rapidity, as also illustrated in
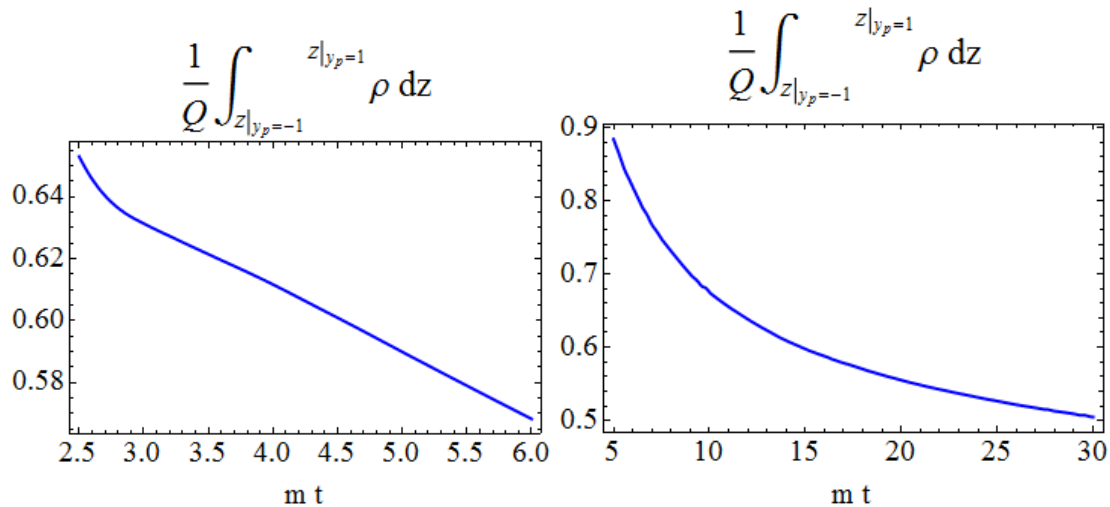
Figure 2.10: We show the fraction of the charge (given in Eq. (2.11)) in the plasma that has momentum rapidity $y_p = \tanh^{-1}(v_{\text{loc}})$ smaller than 1.0 for thin (left) and thick (right) shocks. The plots start at the time that a fluid cell attains momentum rapidity 1.0. Clearly, a large fraction of the charge ends up at relatively small rapidities. Due to the hydrodynamic expansion this charge ends up at larger rapidity later on, which explains why the fraction decreases as a function of time.

the right panel of Fig. 2.4. If the expansion of the system were exactly boost invariant, this quantity would remain constant in the hydrodynamic regime; therefore, the decrease of this fraction at later times is a consequence of non-boost invariant dynamics. Despite this decrease, this computation shows that more than 50% of the charge carried by the initial shocks is deposited within two units of rapidity at early times.[3]

This strong baryon stopping is reminiscent of the behaviour of the net proton number in low-energy heavy ion collisions at $\sqrt{s} < 20$ GeV. Indeed, heavy ion experiments performed at AGS [67] and SPS [68] found a large stopping of the baryon charge, with most of the net protons concentrated in the mid-rapidity region. As the energy of the beams increases, the rapidity width of the charge distribution increases, reducing the fraction of the total charge at mid-rapidity. Taking the width of our shocks as a proxy for the energy of the incident nuclei [55], this trend is in qualitative agreement with the behaviour of the charge distribution in our simulations. This qualitative agreement indicates that shock wave collisions may provide a good framework to understand the

---

[3]This quantity does not directly correspond to experimental measurements, as this requires a longer and more advanced hydrodynamic evolution and freeze-out. Nevertheless, for comparison, experimentally the fraction of baryon charge between rapidity -1.0 and 1.0 is approximately 37% and 8.4% for heavy ion collisions at $\sqrt{s_{\text{NN}}} = 17$ and 200 GeV respectively [9].

hydrodynamisation of low- and moderate-energy heavy ion collisions, as those studied in the RHIC energy scan.

In contrast, the dynamics of our simple holographic model does not seem to agree qualitatively with the distribution of net baryon number in heavy ion collisions at full RHIC or LHC energies. For those energies, the amount of net baryon number at mid-rapidity represents a small fraction of the total baryon number, and the distribution of baryon charge peaks a few units of rapidity away from the beam rapidity. Quite remarkably, as we have discussed, our thin shock simulations hint at the development of maxima at moderately large rapidity, which may be interpreted as the onset of this non-monotonous behaviour. However, unlike in heavy ion collisions, most of the baryon charge is initially concentrated within a few units of rapidity.

The discrepancy above is consistent with the difficulties in reproducing the LHC multiplicity rapidity profiles at high energies, as noted in [56]. It may be due to the extreme simplicity of our model, which just evolves in the simplest holographic setting with the simplest Maxwell field possible, and for instance does not contain any matter in AdS. We are also working in a model that only describes the very first moments of a high energy collision, without treating a long hydrodynamic phase or freeze-out, and our model restricts to homogeneity in the transverse plane. Naturally, the discrepancy may also point to a deeper difference between our holographic setup and the dynamics of QCD. Indeed, most of the baryonic charge of hadrons are carried by valence quarks, which also carry a large fraction of the full hadron momentum. In contrast, the shock waves posses structure functions concentrated at small Bjorken x [69]. Since processes able to reduce the rapidity of valence quarks by a significant amount involve large momentum transfers, large rapidity shifts at high energies are suppressed as a consequence of asymptotic freedom. The qualitative disagreement in the rapidity distribution of the charge is perhaps not surprising given the absence of this perturbative physics on the gravity side. Nevertheless, since the matter produced at mid-rapidities in a ultra-relativistic collision is soft, the interactions and generation of this matter may still be dominated by strong coupling processes. It would be interesting to develop hybrid approaches able to address these two separated regimes within the duality, perhaps along the lines of [70, 71].

Chapter 3

Transport and linear dynamics in non-conformal theories

3.1 Background

Driven by its relative simplicity, most of the studies of strongly coupled dynamics using holography have been performed in conformal field theories. Alas, the conformal symmetry prevents many interesting phenomena present in generic gauge theories. Phase transitions, critical behaviour, and diverse mechanisms to reach equilibrium are left out in such set-ups, making a strong case for studies including non-conformality. Turning to more specific motivations for examining non-conformal theories, we also find the connection with hot quantum chromodynamics and heavy ion collisions. As is well known, QCD is a non-conformal theory even in the limit of vanishing quark masses. State of the art determinations of the QCD equation of state via lattice QCD [17, 72] show that, in equilibrium, the trace of the stress tensor normalised by the enthalpy attains values of order one close to the QCD transition. At high temperature this ratio quickly approaches zero, indicating that QCD behaves as an almost-conformal theory in this regime. However, the experimental exploration of the QCD phase diagram via high-energy heavy ion collisions can only reach temperatures a few times larger than the critical temperature. Even though most central, top-energy LHC collisions lead to initial temperatures well into the quasi-conformal regime, the subsequent evolution and cooling of the QGP after production spans all temperature regimes, including those in which non-conformal effects are maximal. In fact, recent attempts for high-precision extraction of the shear viscosity of the QGP have highlighted the need to include the bulk viscosity of the plasma, which is a purely non-conformal effect [73]. Furthermore, off-central

45

collisions both at the LHC and RHIC, as well as lower-energy collisions as those explored at the RHIC energy scan, produce a QGP with a smaller initial temperature. Similarly the apparent success of hydrodynamics in smaller systems such as p-Pb [74] and p-p [75, 76] collisions indicate the need to study the properties of deconfined but cooler QCD plasma, where non-conformal effects become significant (see [77] and references therein for a recent review on the hydrodynamic modelling of heavy ion collisions).

3.1.1 An additional channel towards equilibrium

The study of the off-equlibrium dynamics of conformal field theories by means of holography has shown that hydrodynamics is a much better approximation to the evolution of this type of matter than ever thought before. Indeed, examples based in flow motions imposed by symmetries [78, 79] or by explicit simulations of the collision dynamics [42, 55, 57, 80] have shown that hydrodynamics provides a good approximation to the complete evolution of the system at time and distance scales as small as a fraction of the (local) inverse temperature of the system. This occurs even in situations in which gradient corrections to the hydrodynamic stress tensor are large, extending the applicability beyond a simple gradient expansion (see also [81]). This observation has led to the coining of the term "hydrodynamisation" to refer to the process by which a system comes to be well described by hydrodynamics, in order to differentiate this process from (local) thermalisation.

In a CFT the vanishing of the trace of the stress tensor implies that the equation of state, namely

$$\bar{p} = \frac{1}{3}e \,, \tag{3.1}$$

where

$$\bar{p} = \frac{1}{3}\left(p_x + p_y + p_z\right) \tag{3.2}$$

is the average pressure, is fixed by symmetry. As a consequence, the equation of state is always obeyed both in and out of equilibrium. We emphasize that the equation of state fixes only the average pressure in terms of the energy density, but not the individual pressures. For this reason the relaxation towards equilibrium in a CFT typically involves "isotropization", namely the process by which the different pressures become approximately equal to one another.

The applicability of the gauge/string duality is not restricted to CFTs. By now infinite families of non-conformal examples are known. One of the main new features in these theories as compared to their conformal cousins is that new channels exist for the relaxation of the out-of-equilibrium matter. In particular, in non-conformal theories the equation of state is not fixed by symmetry. As a consequence, out of equilibrium the energy density and the average pressure may fluctuate independently. The relaxation towards equilibrium in these theories therefore involves the evolution of the energy density and the average pressure towards asymptotic values related to one another by the equation of state (EoS). When this happens we will say that the system has "EoSized" and we will refer to this process as "EoSization". In this chapter we will show the appearance of an additional channel in a particular non-conformal theory and study its near equilibrium properties. We keep for chapter 4 the study of the interplay between the EoSization and hydrodynamization in the context of shock-wave collisions.

In order to study non-conformal theories in a holographic setup we will consider a five-dimensional bottom-up model that nevertheless shares many qualitative features with top-down string models. Specifically, our model is dual to a four-dimensional gauge theory that, at zero temperature, flows from an ultraviolet (UV) fixed point to an infrared (IR) fixed point. This renormalisation group (RG) flow is dual on the gravity side to a domain-wall geometry that interpolates between two AdS spaces. The reason why we require that the flow approaches a fixed point in the UV is that this is the situation in which the holographic duality is best understood. The reason for the IR fixed point is that this guarantees that the zero-temperature solution is smooth in the deep IR. The flow is triggered by a source Λ for a relevant, dimension-three operator in the UV. We will see that this simple model exhibits a rich phenomenology. In particular, we will study the relaxation of small-amplitude, homogenous perturbations by computing the spectrum of quasi-normal modes with zero spatial momentum. We will see that the dominant channel for relaxation in this approximation depends on the value of the ratio T/Λ, with T the temperature of the system. At small T/Λ the system first EoSizes and subsequently isotropises. In contrast, at large T/Λ the order in which these two processes take place is reversed. Although our calculation is done at zero spatial momentum we will argue that, actually, the ordering above is still valid for long-wave-length fluctuations with $k \ll T$. Previous analysis addressing the near-equilibrium properties of strongly coupled non-abelian plasmas include [37, 39, 40, 82–87].

This chapter is organised as follows. In Sec. 3.2 we introduce the holographic model and discuss its vacuum properties. In Sec. 3.3 we study black brane solutions and extract

from them the equation of state and the viscosities of the model. In Sec. 3.4 we study
the relaxation of small excitations of the system by computing the QNM spectrum of the
black branes at different temperatures and zero spatial momentum. Finally, in Sec. 3.5
we discuss our main findings and place them in the context of the hydrodynamisation of
non-abelian plasmas.

3.2 The non-conformal holographic model

The holographic model that we will consider consists of five-dimensional Einstein gravity
coupled to a scalar field with a non-trivial potential:

$$S = \frac{2}{\kappa_5^2} \int d^5 x \sqrt{-g} \left[\frac{1}{4} \mathcal{R} - \frac{1}{2} \left(\nabla \phi \right)^2 - V(\phi) \right] , \tag{3.3}$$

where κ_5 is the five-dimensional Newton constant. For specific forms of $V(\phi)$, this action
may be viewed as a consistent truncation of five-dimensional $\mathcal{N} = 8$ supergravity. The
dynamic equations following from this action are,

$$\mathcal{R}_{\mu\nu} - \frac{\mathcal{R}}{2} g_{\mu\nu} = 8\pi T_{\mu\nu} , \tag{3.4}$$

$$\Box \phi = \frac{\partial V}{\partial \phi} , \tag{3.5}$$

where

$$8\pi T_{\mu\nu} = 2\partial_\mu \phi \partial_\nu \phi - g_{\mu\nu} \left(g^{\alpha\beta} \partial_\alpha \phi \partial_\beta \phi + 2V(\phi) \right) , \tag{3.6}$$

In this chapter we will consider a bottom-up model by choosing a potential that is
particularly simple and yet shares some of the qualitative properties of these top-down
potentials. In particular, we will choose $V(\phi)$ to be negative and to possess a maximum
at $\phi = 0$ and a minimum at $\phi = \phi_M > 0$. Each of these extrema yields an AdS solution
of the equations of motion with constant ϕ and radius $L^2 = -3/V$. In the gauge theory
each of these solutions is dual to a fixed point of the RG with a number of degrees of
freedom N^2 proportional to L^3/κ_5^2.[1]

We will be interested in domain-wall solutions interpolating between these two AdS
solutions. In the gauge theory, these are dual to RG flows from the UV fixed point

---

[1]In the case of $\mathcal{N} = 4$ SYM the precise relation would be $L^3/\kappa_5^2 = N^2/4\pi^2$.

at $\phi = 0$ to the IR fixed point at $\phi = \phi_M$. The problem of finding those solutions is significantly simplified if the potential can be written globally in terms of a superpotential, W, as

$$V(\phi) = -\frac{4}{3} W(\phi)^2 + \frac{1}{2} W'(\phi)^2 \ . \tag{3.7}$$

In this case, vacuum solutions to the Einstein equations can be easily found. Parametrizing the metric as

$$ds^2 = e^{2A(r)} \left(-dt^2 + d\mathbf{x}^2 \right) + dr^2 \ , \tag{3.8}$$

the solution of the back-reacted gravitational problem is reduced to the first-order equations [88]

$$\frac{dA}{dr} = -\frac{2}{3} W \ , \qquad \frac{d\phi}{dr} = \frac{dW}{d\phi} \ . \tag{3.9}$$

3.2.1 A potential leading to two fixed points

We will choose a simple superpotential characterised by a single parameter, ϕ_M,

$$L\,W(\phi) = -\frac{3}{2} - \frac{\phi^2}{2} + \frac{\phi^4}{4\phi_M^2} \ , \tag{3.10}$$

which together with equation (3.7) yields the potential

$$L^2 V = -3 - \frac{3}{2}\phi^2 - \frac{1}{3}\phi^4 + \left(\frac{1}{3\phi_M^2} + \frac{1}{2\phi_M^4} \right) \phi^6 - \frac{1}{12\phi_M^4}\phi^8 \ . \tag{3.11}$$

Note that both the superpotential and the potential have a maximum at $\phi = 0$ and a minimum at $\phi = \phi_M$. This choice leads to three important properties of the associated vacuum solution. First, the resulting geometry is asymptotically AdS$_5$ in the UV with radius L, since $V(0) = -3/L^2$. Second, the second derivative of the potential at $\phi = 0$ implies that, in this asymptotic region, the scalar field has mass $m^2 = -3/L^2$. Following the standard quantisation analysis, this means that, in the UV, this field is dual to an operator in the gauge theory, $\mathcal{O}$, with dimension $\Delta_{UV} = 3$. Third, the solution near

$\phi = \phi_M$ is again AdS$_5$ with a different radius

$$L_{\text{IR}} = \sqrt{-\frac{3}{V(\phi_M)}} = \frac{1}{1 + \frac{1}{6}\phi_M^2} L \, . \tag{3.12}$$

In this region the effective mass of the scalar field differs from its UV value and it is given by

$$m_{\text{IR}}^2 = \frac{12}{L^2}\left(1 + \frac{1}{9}\phi_M^2\right) = \frac{12}{L_{IR}^2} \frac{\left(1 + \frac{1}{9}\phi_M^2\right)}{\left(1 + \frac{1}{6}\phi_M^2\right)^2} \, . \tag{3.13}$$

As a consequence, the operator $\mathcal{O}$ at the IR fixed point has dimension

$$\Delta_{IR} = 2 + 2\sqrt{1 + \frac{m_{\text{IR}}^2 L_{\text{IR}}^2}{4}} = 6\left(1 + \frac{\phi_M^2}{9}\right)\left(1 + \frac{\phi_M^2}{6}\right)^{-1} \, . \tag{3.14}$$

To summarize, the vacuum solution describes a RG flow from an UV to an IR fixed point with a smaller number of degrees of freedom, as indicated by the fact that $L_{\text{IR}} < L$. We see that changing ϕ_M has two main effects. First, as ϕ_M increases the difference in degrees of freedom between the UV and the IR fixed points increases. Second, the dimension of the scalar operator at the IR fixed point decreases with increasing ϕ_M, reaching the marginal dimension $\Delta_{IR} = 4$ at $\phi_M \to \infty$. However, in this limiting case the IR fixed point disappears and the background solution becomes singular, as is evident from the fact that the effective AdS radius goes to zero as $\phi_M \to \infty$.

3.2.2 Vacuum solution

Our simple choice of the superpotential allows us to determine analytically the vacuum solution for arbitrary ϕ_M. Solving equations (3.9), we obtain

$$e^{2A} = \frac{\Lambda^2 L^2}{\phi^2}\left(1 - \frac{\phi^2}{\phi_M^2}\right)^{\frac{\phi_M^2}{6}+1} e^{-\frac{\phi^2}{6}} \tag{3.15}$$

$$\phi(r) = \frac{\Lambda L e^{-r/L}}{\sqrt{1 + \frac{\Lambda^2 L^2}{\phi_M^2} e^{-2r/L}}} \, , \tag{3.16}$$

where Λ is an arbitrary constant that controls the magnitude of the non-normalizable mode of the scalar field. As we will see, in the dual gauge theory side, Λ is identified with

the source of the dimension-3 operator $\mathcal{O}$. The presence of this source breaks conformal invariance explicitly.

Noticing that the small field behaviour of the superpotential (4.8) is identical to that of the GPPZ flow [89], we can readily determine the vacuum expectation values (VEV) of the stress tensor and the scalar operator. We begin by expanding the metric and the scalar field in powers of $u = Le^{-r/L}$ in the $u \to 0$ limit. Following [88], we write the 5-dimensional metric in the form

$$ds^2 = \frac{L^2}{u^2} \left(du^2 + g_{\mu\nu} \, dx^\mu dx^\nu \right) , \tag{3.17}$$

and we write the power expansion coefficients of the metric and the scalar field as

$$g_{\mu\nu} = \eta_{\mu\nu} + g^{(2)}_{\mu\nu} u^2 + g^{(4)}_{\mu\nu} u^4 + \dots , \tag{3.18}$$

$$\phi = \Lambda u \left(1 + \phi_2 u^2 + \dots \right) . \tag{3.19}$$

The expectation values of the field theory operators are then given by

$$\langle T_{\mu\nu} \rangle = \frac{2L^3}{\kappa_5^2} \left[g^{(4)}_{\mu\nu} + \left(\Lambda^2 \phi_2 - \frac{\Lambda^4}{18} + \frac{\Lambda^4}{4\phi_M^2} \right) \eta_{\mu\nu} \right] , \tag{3.20}$$

$$\langle \mathcal{O} \rangle = -\frac{2L^3}{\kappa_5^2} \left(2\Lambda \phi_2 + \frac{\Lambda^3}{\phi_M^2} \right) . \tag{3.21}$$

To arrive at these expressions we have chosen the superpotential as a counterterm to regularise the on-shell action, which is possible because in our model the superpotential corresponds to a deformation of the gauge theory as opposed to a VEV [90]. We emphasize that these expressions are valid even if the metric $g_{\mu\nu}$ does not posses the full Poincaré symmetry but only rotational and translational invariance along the gauge theory directions, as will be the case for the black brane geometries that we will study in the next section. As expected, eqs. (3.20) and (3.21) imply the Ward identity for the trace of the stress tensor

$$\langle T^\mu_\mu \rangle = -\Lambda \langle \mathcal{O} \rangle . \tag{3.22}$$

Eqs. (4.10) and (4.11) determine the VEVs in the vacuum of the theory. Let us define the energy density ϵ and the pressure p as the diagonal components of the expectation value of the stress tensor, $\langle T^{\mu\nu} \rangle = \text{Diagonal} \{ \epsilon, p, p, p \}$. The near boundary behaviour of

ϕ, (4.11), leads to

$$\phi_2 = -\frac{\Lambda^2}{2\phi_M^2} \, , \tag{3.23}$$

which implies that in the vacuum

$$\langle \mathcal{O} \rangle = 0, \qquad \langle T^{\mu\nu} \rangle = 0 \, . \tag{3.24}$$

Note that the explicit breaking of scale invariance means that the trace of the stress tensor is non-zero as an operator. However, the VEV of this operator vanishes in the vacuum state, as implied by trace Ward identity (2.17) together with the fact that $\langle \mathcal{O} \rangle = 0$ in the vacuum for our choice of renormalisation scheme. It should be emphasized that even though the trace Ward identity (3.22) is scheme-independent, the individual vacuum expectation values of the trace of the stress tensor and of the scalar operator do depend on the renormalisation scheme. In the model we study here the only scheme ambiguity corresponds to a term of the form $\Lambda^4 \eta_{\mu\nu}$ in the expectation value of the stress tensor, accompanied by a term of the form Λ^3 in the expectation value of $\mathcal{O}$, with the relative coefficient such that the identity (3.22) is preserved.

To estimate at which scale non-conformal effects become important, let us perform a change of variables in the holographic direction, which explicitly exploits the relation between the dynamics in the bulk with the physics at different scales in the field theory. Denoting the coordinate by z, we write the metric as

$$ds^2 = \frac{L_{\text{eff}}(z)^2}{z^2} \left(-dt^2 + d\mathbf{x}^2 + dz^2 \right) \, , \tag{3.25}$$

with L_{eff} a non-trivial function of z such that $L_{\text{eff}}(0) = L$ and $L_{\text{eff}}(\infty) = L_{\text{IR}}$. In this set of coordinates, at least in the two asymptotic conformal regions, the coordinate z is related to the energy scale, Q, in the gauge theory through $z \sim 1/Q$. The relation between z and u is given by

$$z(u) = \int_0^u du \frac{L}{u} e^{-A} \, , \tag{3.26}$$

and the function L_{eff} is given by

$$L_{\text{eff}}(z) = z \, e^A \, . \tag{3.27}$$

In Fig. 3.1 we show the ratio L_{eff}/L as a function of z for several different values of the parameter ϕ_M controlling the physics of the model. We see that the system behaves approximately conformally up to scales of order $z \sim \Lambda$. At this scale, the metric starts to deviate significantly from that of AdS_5, and L_{eff} decreases as a function of z. Sufficiently deep in the IR, L_{eff} approaches L_{IR} and the system behaves again as approximately conformal. However, the scale at which this transition occurs depends significantly on the model parameter ϕ_M; as ϕ_M increases, the function L_{eff} approaches its asymptotic value more slowly. This different rates at which the IR fixed point is approached have consequences for the finite-temperature behaviour of the dual gauge theory, as we will see in the next section.

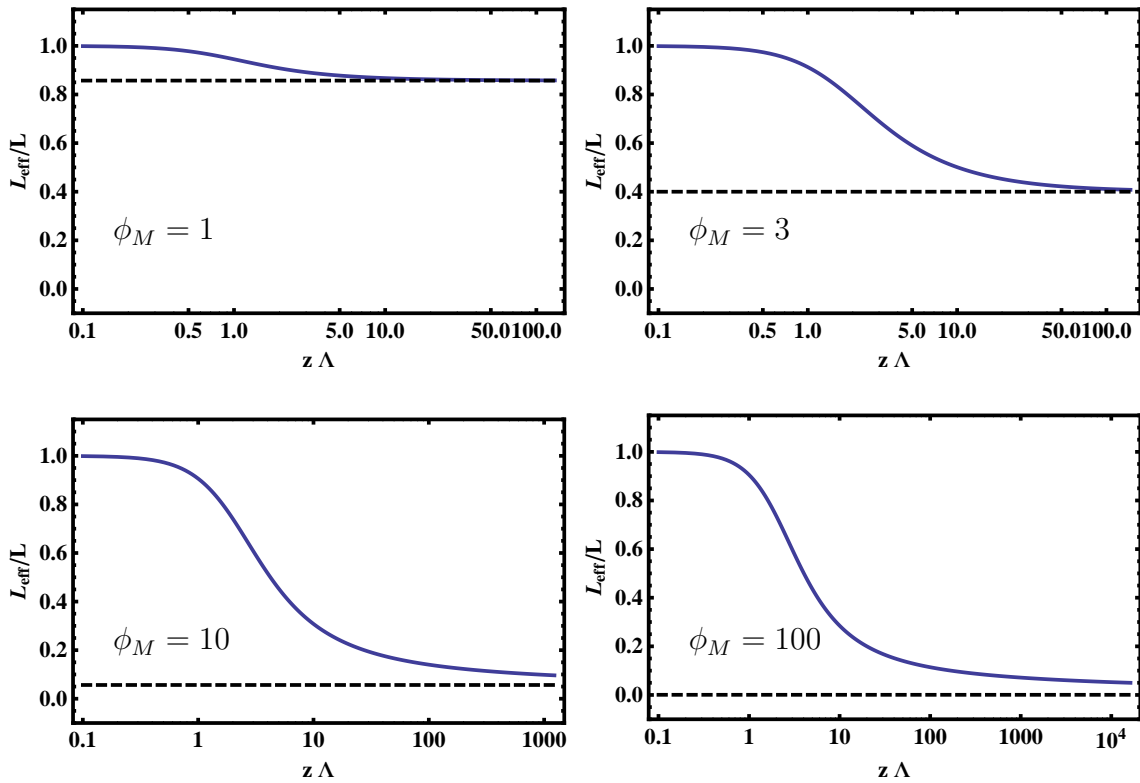**Figure 3.1:** L_{eff}/L as a function for z for different values of ϕ_M. In all panels, the dashed line shows the asymptotic infrared value of the effective AdS radius L_{IR}. Note the different scales of the horizontal axes in the different panels.

3.3 Thermodynamics and transport

3.3.1 Equations and numerical methods

We will now explore the thermal physics of the gauge theory dual to the gravitational model described in the previous section.[2] To do so, we will search for black brane solutions of the action (4.1). Finding the thermodynamics of a particular model amounts to finding the family of homogeneous black brane solutions parametrized by the temperature or, equivalently, by the value of the scalar field at the horizon ϕ_H. We will follow the method of the master function, introduced in ref. [94], to which we refer the reader for details.[3] Since for the background solution (4.11) the scalar field is a monotonic function of u, we may use the scalar field as a coordinate and express the metric as

$$ds^2 = e^{2A} \left(-h(\phi)d\tau^2 + d\mathbf{x}^2 \right) - 2e^{A+B} L \, d\tau d\phi \,, \qquad (3.28)$$

with $h(\phi)$ vanishing at $\phi = \phi_H$, the value of the scalar field at the horizon, i.e. $h(\phi_H) = 0$. The region outside the horizon corresponds to $0 < \phi < \phi_H$. For later convenience, we have expressed the metric in Eddington-Finkelstein form. With this ansatz, Einstein's equations take the form

$$A''(\phi) - A'(\phi)B'(\phi) + \frac{2}{3} = 0 \,,$$

$$4A'(\phi)h'(\phi) - B'(\phi)h'(\phi) + h''(\phi) = 0 \,, \qquad (3.29)$$

$$\frac{3}{2}A'(\phi)h'(\phi) + h(\phi)\left(6A'(\phi)^2 - 1\right) + 2e^{2B(\phi)}L^2 V(\phi) = 0 \,,$$

$$4A'(\phi) - B'(\phi) - \frac{e^{2B(\phi)}L^2 V'(\phi)}{h(\phi)} + \frac{h'(\phi)}{h(\phi)} = 0 \,.$$

A solution to these equations may be found in terms of a master function $G(\phi)$ defined as

$$G(\phi) = \frac{d}{d\phi} A(\phi) \,. \qquad (3.30)$$

---

[2]Previous studies of the thermodynamics of Einstein+scalar gravity include [91–93].

[3]Note that our normalisations of the scalar field and of the potential differ from those in [94].

Manipulating the set of equations (3.29), a non-linear equation for G was found in [94]:

$$\frac{G'(\phi)}{G(\phi) + \frac{4V(\phi)}{3V'(\phi)}} = \frac{d}{d\phi} \log\left(\frac{1}{3G(\phi)} - 2G(\phi) + \frac{G'(\phi)}{2G(\phi)} - \frac{G'(\phi)}{2\left(G(\phi) + \frac{4V(\phi)}{3V'(\phi)}\right)}\right) . \qquad (3.31)$$

Close to the boundary, $\phi \to 0$, the solution of this equation behaves as

$$G(\phi) = \frac{1}{\Delta - 4}\frac{1}{\phi} + \cdots , \qquad (3.32)$$

with Δ the scaling dimension of the dual operator. With our choice of potential (5.1) we have $\Delta = 3$. Using (3.29), the different metric coefficients are given by

$$A(\phi) = -\log\left(\frac{\phi}{\Lambda}\right) + \int_0^\phi d\tilde{\phi}\left(G(\tilde{\phi}) + \frac{1}{\tilde{\phi}}\right) , \qquad (3.33)$$

$$B(\phi) = \log\left(|G(\phi)|\right) + \int_0^\phi d\tilde{\phi}\frac{2}{3G(\tilde{\phi})} , \qquad (3.34)$$

$$h(\phi) = -\frac{e^{2B(\phi)}L^2\left(4V(\phi) + 3G(\phi)V'(\phi)\right)}{3G'(\phi)} . \qquad (3.35)$$

In these expressions, the constants of integration are fixed by requiring that, close to the boundary, the metric and scalar field may be expressed as in the expansions (3.18) and (3.19).

At the horizon, the condition $h(\phi_H) = 0$ together with the last two equations in (3.29) fix the value of $G(\phi_H)$. Starting from this fixed value, a power series solution close to the horizon may be found as

$$G(\phi) = -\frac{4V(\phi_H)}{3V'(\phi_H)} + \frac{2}{3}(\phi - \phi_H)\left(\frac{V(\phi_H)V''(\phi_H)}{V'(\phi_H)^2} - 1\right) + \mathcal{O}\left((\phi - \phi_H)^2\right) . \qquad (3.36)$$

One can easily find an arbitrary number of terms in the series expansion using an iterative automated *Mathematica* script that solves (3.31) order by order. This series will be used to set boundary conditions close to the horizon for the numerical resolution of (3.31), solved using `NDSolve[]` from *Mathematica*. For the thermodynamics computation it is enough with 10 terms in the near horizon expansion to obtain precise integrations of the master function $G(\phi)$. However, the computation of the QNM will require a substantially more precise background solution and we will use 45 orders. In this case, it is necessary to specify the potential and the value of ϕ_H to speed up the order by order solution.

From the metric coefficients, we can extract the Hawking temperature T and the entropy density s for every solution of the black brane:

$$LT = \frac{A(\phi_H) - B(\phi_H)}{4\pi} \, , \qquad s = \frac{2\pi}{\kappa_5^2} e^{3A(\phi_H)} \, . \tag{3.37}$$

The relation of the different metric coefficients with the master function leads to the following form for the temperature and entropy of the thermal state:

$$T = -\Lambda \frac{L^2 V(\phi_H)}{3\pi \phi_H} \exp \left\{ \int_0^{\phi_H} d\phi \left(G(\phi) + \frac{1}{\phi} + \frac{2}{3G(\phi)} \right) \right\} \, , \tag{3.38}$$

$$s = \frac{2\pi}{\kappa_5^2} \frac{\Lambda^3}{\phi_H{}^3} \exp \left\{ 3 \int_0^{\phi_H} d\phi \left(G(\phi) + \frac{1}{\phi} \right) \right\} \, . \tag{3.39}$$

These expressions are well suited for the determination of the two quantities from the numerical evaluation of the master equation (3.31). With them, we can find a couple of values $\{T, s\}$ for every solution labelled by ϕ_H, and build interpolation functions $s(T)$ that will be used to find the rest of thermodynamic variables like ϵ or p and the transport coefficients.

3.3.2 Results

In this section we review the results of the thermodynamics and transport properties of the plasmas obtained for several values of Φ_M. In Fig. 3.2 we plot the dimensionless quantity

$$s_R = \frac{\kappa_5^2}{2\pi^4 L^3} \frac{s}{T^3} \, , \tag{3.40}$$

as a function of the inverse temperature for two different values of ϕ_M. Since the theory is conformal both at the UV and at the IR, the high and low temperature behaviour of the entropy density must coincide with that of a relativistic conformal theory and scale as T^3. In particular, for a relativistic CFT, s/T^3 is proportional to the number of degrees of freedom in the theory, which for an $SU(N)$ gauge theory with matter in the adjoint representation scales as N^2. For example, for $\mathcal{N} = 4$ SYM

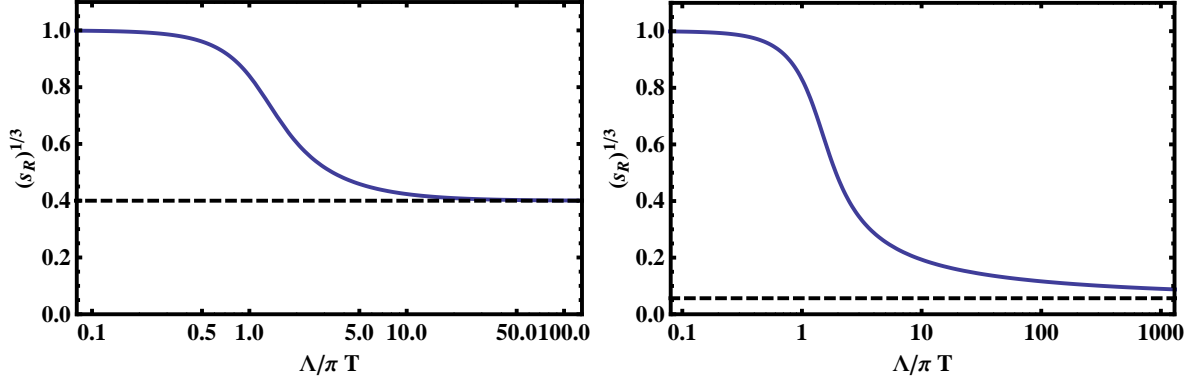$$\frac{s}{T^3} = \frac{\pi^2}{2} N^2, \tag{3.41}$$

Figure 3.2:   Ratio of entropy density to temperature for $\phi_M = 3$ (left) and $\phi_M = 10$ (right) as a function of the inverse temperature. The dashed line shows $L_{\mathrm{IR}/L}$.

but the precise coefficient depends on the specific theory. In terms of the parameters of the dual gravity description this quantity becomes

$$\frac{s}{T^3} = \frac{2\pi^4 L^3}{\kappa_5^2}. \tag{3.42}$$

In our bottom-up setup, the above argument allows us to *define* the number of degrees of freedom at the fixed points holographically in terms of the effective AdS radius. In particular, the quantity s_R should approach 1 at high temperature and $(L_{IR}/L)^3$ at low temperature, which is confirmed by the plots in figure 3.2.

Using standard thermodynamic relations and the fact that in our renormalisation scheme the vacuum pressure is zero we can determine the pressure and the energy density of the thermal system through. As expected, the results show the conformal behaviour for high and low temperatures (this is, $p = \epsilon/3$) and an intermediate region affected by the non-conformality (see fig. 3.3)

$$p = \int_0^T d\tilde{T}\, s(\tilde{T})\,, \qquad \epsilon + p = Ts\,. \tag{3.43}$$

Since the theory is not conformal, the trace of the stress tensor in the thermal ensemble does not vanish. Using the Ward identity (3.22), the energy density, the pressure and the scalar condensate at non-zero temperature are related through

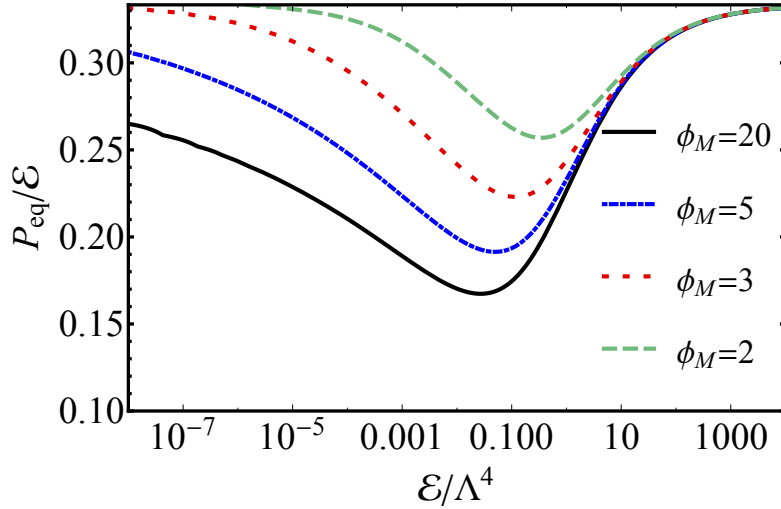$$\epsilon - 3p = \Lambda \langle \mathcal{O} \rangle_T\,. \tag{3.44}$$

Figure 3.3: Equilibrium pressure as a function of energy density for $\phi_M = 2\,,3\,,5\,,20$. The non-conformality effects are stronger for larger values of ϕ_M.

The thermal expectation value $\langle\mathcal{O}\rangle_T$ may be determined from the normalisable mode of the scalar field in the thermal background via equation (3.19). Since at $T = 0$ the scalar VEV vanishes (see (3.24)) this relation implies that $\epsilon = 3p$, as expected from the fact that the IR theory is conformal. At $T > 0$, however, $\langle\mathcal{O}\rangle_T \neq 0$, as shown in Fig. 3.4, and the expectation value of the trace of the stress tensor does not vanish. Note that, unlike at low temperatures, at which $\langle\mathcal{O}\rangle_T$ depends on ϕ_M, at high temperatures $\langle\mathcal{O}\rangle_T$ becomes independent of ϕ_M. This is easy to understand from the gravitational computation. At high temperatures the value of the scalar field at the horizon is small and, therefore, the physics is sensitive only to the small-field behaviour of the scalar potential, which is independent of ϕ_M. In this limit, the plots in Fig. 3.4 show that the VEV scales as $\langle\mathcal{O}\rangle_T \sim \Lambda T^2$.

Despite the fact that the trace of the stress tensor at high temperature does not vanish, the theory does behave as a conformal theory. From the gauge theory viewpoint this may be understood from the relative magnitude of the trace of the stress tensor compared to the energy density or the pressure: while at large T the latter quantities scale as T^4, the trace only grows as T^2. In Fig. 3.5 we show the temperature dependence of the ratio of the stress tensor to the enthalpy,

$$I = \frac{\epsilon - 3p}{\epsilon + p}\,, \tag{3.45}$$
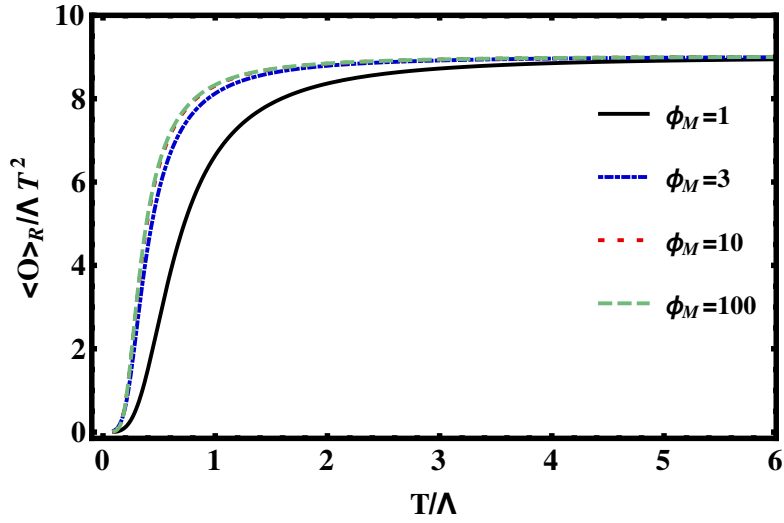
Figure 3.4: Temperature dependence of the VEV of the scalar operator $\langle \mathcal{O} \rangle_T$ for several values of ϕ_M. $\langle \mathcal{O} \rangle_R = \kappa_5^2 \langle \mathcal{O} \rangle_T / L^3$.
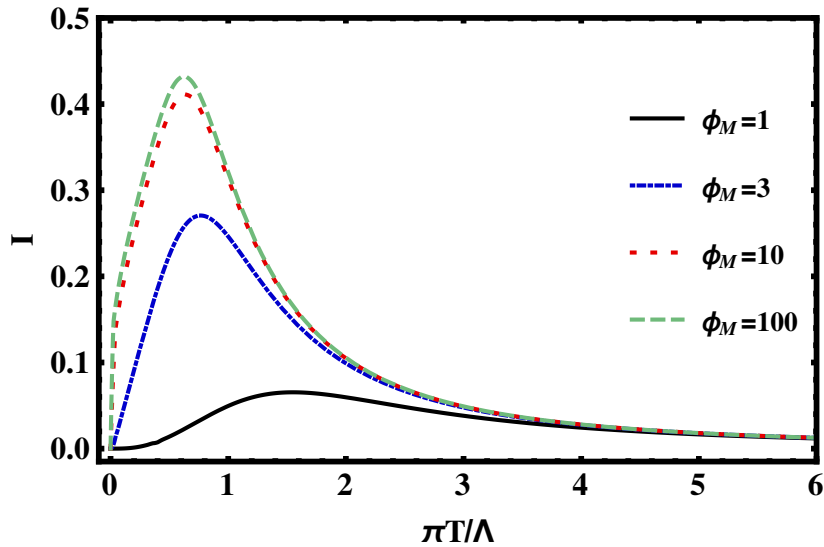
Figure 3.5: Ratio of the trace of the stress tensor to the enthalpy, I, as a function of T for different values of ϕ_M.

which in the thermal-QCD literature is sometimes referred to as the interaction measure. As anticipated, both at low and high temperatures this ratio vanishes, indicating that the theory becomes effectively conformal in these limits. At intermediate temperatures, the value of I is non-zero and depends on ϕ_M. As inferred from the behaviour of the entropy, the larger ϕ_M the larger the deviations from conformality in the thermodynamic properties of the theory. Because of this behaviour we may use I as a measure of the non-conformality of the theory.
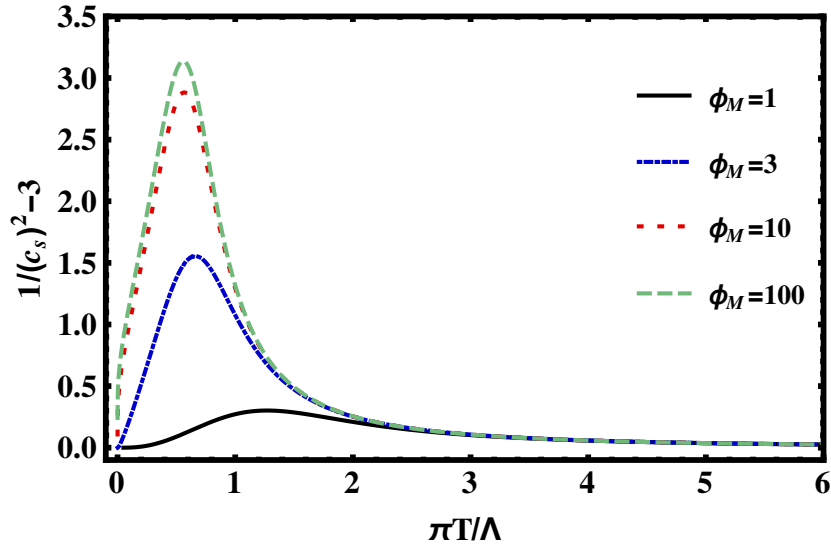
Figure 3.6: Inverse speed of sound square as a function of T for different values of ϕ_M.

Another way to quantify the non-conformal behaviour of the thermodynamics of the dual theory is the value of the speed of sound. Using thermodynamic identities, the square of the speed of sound may be determined from the inverse of the logarithmic derivative of the entropy,

$$\frac{1}{c_s^2} = \frac{d \log s}{d \log T} \,. \tag{3.46}$$

In Fig. 3.6 we show the temperature behaviour of the deviation of c_s from its conformal value, $c_s = 1/\sqrt{3}$, for different values of ϕ_M. The qualitative behaviour of this quantity is very similar to that of I. Both at high and low temperatures, the speed of sound approaches its conformal value. At intermediate temperatures we have $c_s^2 < 1/3$ and the deviation from the conformal value grows with ϕ_M.

The non-conformal behaviour already observed in the equation of state of the system is also reflected in the transport properties of the dual gauge theory plasma. Since this is isotropic, at leading order in gradients transport phenomena are controlled by only two coefficients, the shear viscosity η and the bulk viscosity ζ. Because of the universality of the shear viscosity to entropy ratio [16] in all theories with a two-derivative gravity dual, we have that this ratio in our model takes the same value as in the conformal $\mathcal{N} = 4$ theory, i.e. $\eta/s = 1/4\pi$. In contrast, the bulk viscosity, which would vanish identically in a CFT, is non-zero in our model. Following[4] [95] we determine the bulk viscosity by

---

[4]Note that our normalisation of the scalar field differs from that in [95].

studying the dependence of the entropy on the value of the scalar field at the horizon,[5]

$$\frac{\zeta}{\eta} = 4 \left(\frac{d \log s}{d \phi_H} \right)^{-2} . \tag{3.47}$$

The temperature dependence of this ratio is shown in Fig. 3.7 for different values of ϕ_M. The behaviour of this ratio is very similar to that of the interaction measure and the speed of sound: both at low and high temperatures the ratio of the two viscosities vanishes, while at intermediate temperatures $T \sim \Lambda$ it attains ϕ_M-dependent values that grow with ϕ_M. As in the case of $\epsilon - 3p$ and the interaction measure, the fact that the ratio of viscosities vanishes at high temperatures does not imply that the bulk viscosity itself vanishes. In fact, we have checked numerically that at high temperatures the bulk viscosity scales as $\zeta \sim \Lambda^2 T$. Nevertheless, the fact that the ratio of viscosities approaches zero shows that transport is effectively conformal, since the contribution to the hydrodynamic stress tensor of the bulk tensor is suppressed with respect to the shear one.[6]
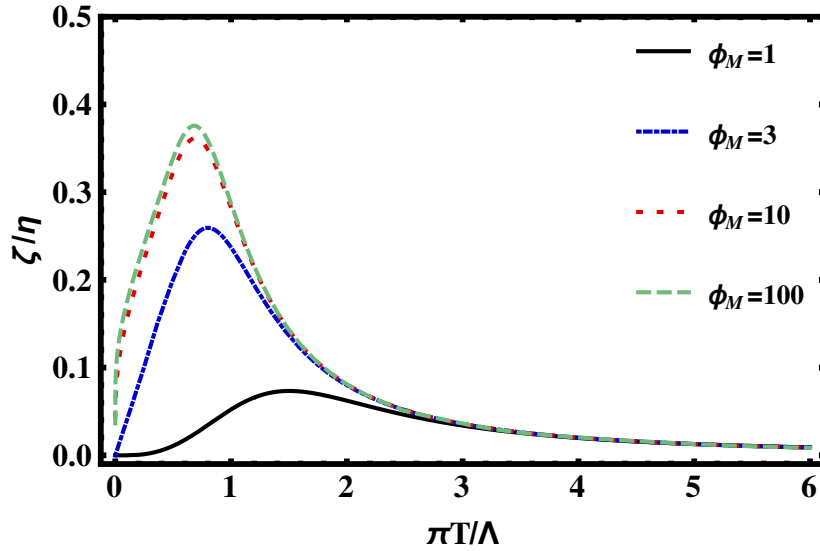
Figure 3.7: Ratio of bulk to shear viscosity as a function of temperature for different values of ϕ_M.

---

[5]We have cross-checked the result of this computation with a two-point function computation as in [96]. See also [97] for a general analysis of the bulk viscosity for Dp-brane solutions.

[6]Here we are implicitly assuming that the magnitude of the shear tensor is not parametrically suppressed with respect to the bulk one. Should the flow of the system be prepared such that the shear tensor identically vanishes, then transport would be dominated by the bulk tensor.
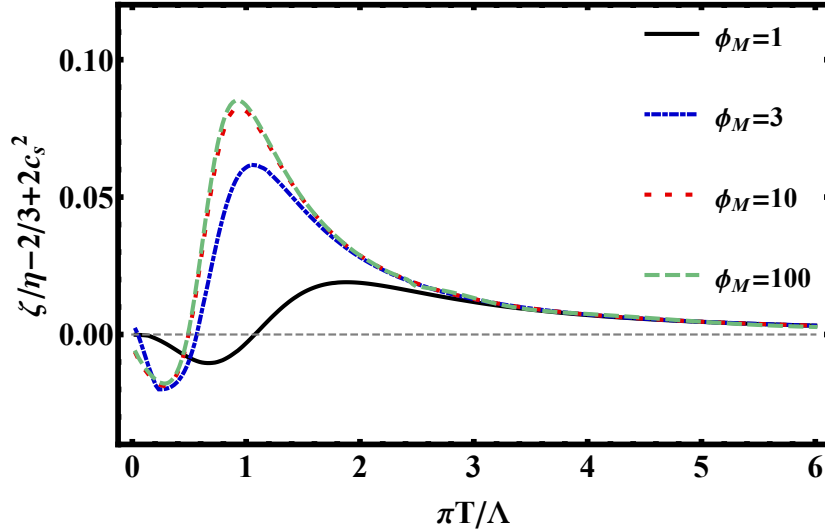
Figure 3.8: Violation of Buchel's bound at low temperatures.

It is interesting to note that the ratio of viscosities at low temperatures violates Buchel's bound

$$\frac{\zeta}{\eta} \geq 2\left(\frac{1}{3} - c_s^2\right) , \tag{3.48}$$

as illustrated in Fig. 3.8. Violations of this bound have been previously encountered in other models such as [94, 96, 98].

3.4 Quasi-normal modes and relaxation

3.4.1 Fluctuations and channels of dissipation

We now turn to the description of the off-equilibrium dynamics of our holographic model. We study the reaction of the system to small perturbations which drive it away from local equilibrium. On the gravity side this problem translates into the study of the relaxation of the black brane solutions constructed above when the different background fields are perturbed. As is well known, this relaxation process is controlled by an infinite set of discrete, damped modes known as QNMs. In this section we will determine the QNM frequencies of the system as a function of the temperature.

Since in our holographic model the scalar field backreacts on the geometry, metric fluctuations couple to fluctuations of the scalar field and they must all be considered

simultaneously. Denoting by $G^{(\mathrm{T})}$ the black brane metric in Eddington-Finkelstein coordinates (3.28), we will study fluctuations of the form

$$G^{(\mathrm{T})}{}_{MN} \to G^{(\mathrm{T})}{}_{MN} + h_{MN}, \qquad \phi \to \phi + \varphi. \tag{3.49}$$

The dynamics of h_{MN} and φ is governed by the linearised Einstein and scalar field equations on the background spacetime $G^{(\mathrm{T})}{}_{MN}$. We will use the value of the unperturbed scalar field ϕ as a coordinate in the holographic direction.

As is well known (see e.g. [35]) not all fluctuations are physical, since reparametrisation invariance leads to a gauge symmetry in the linearised equations of motion. In the presence of a scalar field, the linearised equations of motion are invariant under the transformation

$$h_{MN} \to h_{MN} + \nabla_M \chi_N + \nabla_M \chi_N, \qquad \varphi \to \varphi + \chi^M \nabla_M \phi, \tag{3.50}$$

with χ^M a spacetime-dependent vector field and ∇_M the covariant derivative in the background metric $G^{(\mathrm{T})}{}_{MN}$. Because of this symmetry, not all fluctuations are physical and the relaxation dynamics of the black brane is encoded in the spectrum of gauge invariant combinations of fields.[7]

Due to the nature of the linearized equations, the solutions considered in the QNM analysis have the form

$$h_{MN}(\phi, t, \mathbf{x}) = h_{MN}(\phi)e^{-i\omega + \mathbf{k} \cdot \mathbf{x}} \tag{3.51}$$

$$\varphi(\phi, t, \mathbf{x}) = \varphi(\phi)e^{-i\omega + \mathbf{k} \cdot \mathbf{x}}. \tag{3.52}$$

When plugged into the linerized equations along with the background solution, one obtains the equations that pose the eigenvalue problem for ω at each value of k. In this chapter, however, we will restrict the study to the relaxation of homogeneous disturbances of the plasma. This is equivalent to setting $k = 0$ in the fluctuation equations, and allows the use of the spectral method introduced in [37].

We will consider both isotropic and anisotropic perturbations and we will denote by z the direction of anisotropy. On the gravity side, these perturbations will depend on time and on the holographic radial coordinate. Under these conditions, there are only two independent sets of gauge invariant excitations of the plasma, which may be

---

[7]See [99] for a detailed classification of these fluctuations in the context of non-conformal theories.

parametrized by the following combination of fields[8]

$$\mathcal{Z}_{\text{aniso}} = e^{-2A} \left(h_{zz} - h_{aa} \right) , \tag{3.53}$$

$$\mathcal{Z}_{\text{bulk}} = \varphi - \frac{e^{-2A(\phi)}}{2A'(\phi)} h_{aa} , \tag{3.54}$$

where $h_{aa} = (h_{xx} + h_{yy})/2$. The first fluctuation, $\mathcal{Z}_{\text{aniso}}$, controls anisotropic perturbations that leave unaffected the expectation value of the scalar operator, the average pressure and the trace of the stress tensor. The non-conformal mode $\mathcal{Z}_{\text{bulk}}$ controls fluctuations that change the three pressures in an isotropic way and at the same time modify the expectation value of the scalar operator and the trace of the stress tensor. At non-zero spatial momentum these excitations would be coupled to one another and they would include the hydrodynamic modes. Our restriction to the space-independent sector implies that the energy density of the plasma is unchanged by the fluctuations (3.53)-(3.54), since in a homogeneous plasma conservation of the stress tensor reduces to $\partial_t \epsilon = 0$.

3.4.2 Equations and eigenvalue problem

Manipulating the linearised Einstein and Klein-Gordon equations and after a Fourier transform in time, the dynamics of the $\mathcal{Z}_{\text{aniso}}$ and $\mathcal{Z}_{\text{bulk}}$ modes are given by the equations

$$-i\omega \mathcal{L}_{\text{bulk}} \, \mathcal{Z}_{\text{bulk}} = \mathcal{R}_{\text{bulk}} \, \mathcal{Z}_{\text{bulk}} , \tag{3.55}$$

$$-i\omega \mathcal{L}_{\text{aniso}} \, \mathcal{Z}_{\text{aniso}} = \mathcal{R}_{\text{aniso}} \, \mathcal{Z}_{\text{aniso}} , \tag{3.56}$$

where $\mathcal{L}_{\text{bulk}}, \mathcal{L}_{\text{bulk}}, \mathcal{R}_{\text{aniso}}, \mathcal{R}_{\text{aniso}}$ are linear operators in the holographic direction given by

$$\mathcal{L}_{\text{aniso}} = \mathcal{L}_{\text{bulk}} = \frac{L e^{B-A}}{h(\phi)} \left(3A' + 2\frac{d}{d\phi} \right) , \tag{3.57}$$

$$\mathcal{R}_{\text{aniso}} = \frac{L^2 e^{2B} V'}{h} \frac{d}{d\phi} + \frac{d^2}{d\phi^2} , \tag{3.58}$$

$$\mathcal{R}_{\text{bulk}} = \mathcal{R}_{\text{aniso}} + \frac{\left[8h \left(6 \left(A' \right)^2 - 1 \right) - 3A' \left(L^2 e^{2B} \left(3A'V'' + 8V' \right) - 4h' \right) \right]}{9h \left(A' \right)^2} , \tag{3.59}$$

---

[8]Anisotropic fluctuations induced by $\mathcal{Z}_0 = h_{xy}$ are also possible and independent of the two modes listed in equations (3.53)-(3.54). However, we will not consider these fluctuations here because at zero spatial momentum the dynamics of $\mathcal{Z}_0$ is identical to that of $\mathcal{Z}_{\text{aniso}}$.

with A, B and h the numerically computed functions which determine the background, given by (3.33)-(3.35). The equation for the anisotropic fluctuation, $\mathcal{Z}_{\mathrm{aniso}}$, is that of a massless probe scalar field, while the equation for the bulk fluctuations $\mathcal{Z}_{\mathrm{bulk}}$ includes an explicit dependence on the potential. The discrete set of normalizable, in-falling solutions of this system of equations are the QNMs. The fact that the equations are linear in the frequency is a consequence of the Eddington-Finkelstein form of the thermal metric (3.28).

Following [37] we determine the QNMs and their associated frequencies using a spectral decomposition, which allows us to reduce the problem of finding the complex-valued spectrum of excitations to a generalised eigenvalue problem. When using the pseudo-spectral collocation points method, one can compute with very high precision the background functions only on grid points, and express the equations (3.56) in a matricial form like in (1.14). At this point one also needs to impose boundary conditions to obtain the desired QNM solutions. These are normalizability at the boundary (the value of the mode needs to go to zero) and "ingoingness" at the horizon, which is guaranteed by demanding regular functions in an Eddington-Finkelstein frame. To impose the condition at the boundary we simply substitute the first row of the operators $\mathcal{R}$ by a row of zeros, and the first row of $\mathcal{L}$ by a row of zeros with a one at the last slot. This way we will ensure that all modes fulfil $\mathcal{Z}[0] = 0$. For the $\mathcal{Z}_{bulk}$ equation we actually solve for $\phi\mathcal{Z}_{bulk}$ to be able to set the non-normalizable mode to 0.

Using *Wolfram Mathematica* we can easily solve generalized eigenvalue problems through the functions `Eigenvalues[]` and `Eigenvectors[]`. The outcome of the computation is a list of eigenvalues (QNM frequencies) for each gauge invariant combination and their respective radial profiles (eigenvectors). An added advantage to this method is that one only needs to compute the background metric coefficients (numerical integrations of G) in a set of points, which can be done with very high precision at small computational cost. For these particular computations we used a grids ranging from 100 to 120 points and a precision of at least 120 digits (to ensure no round off errors in the near to boundary points).

We have also double-checked the results for some representative frequencies with a direct integration of the fluctuation equations from the horizon. The fluctuations take values consistent with zero at the boundary for frequencies for which the spectral methods give eigenvalues see figure 3.9.
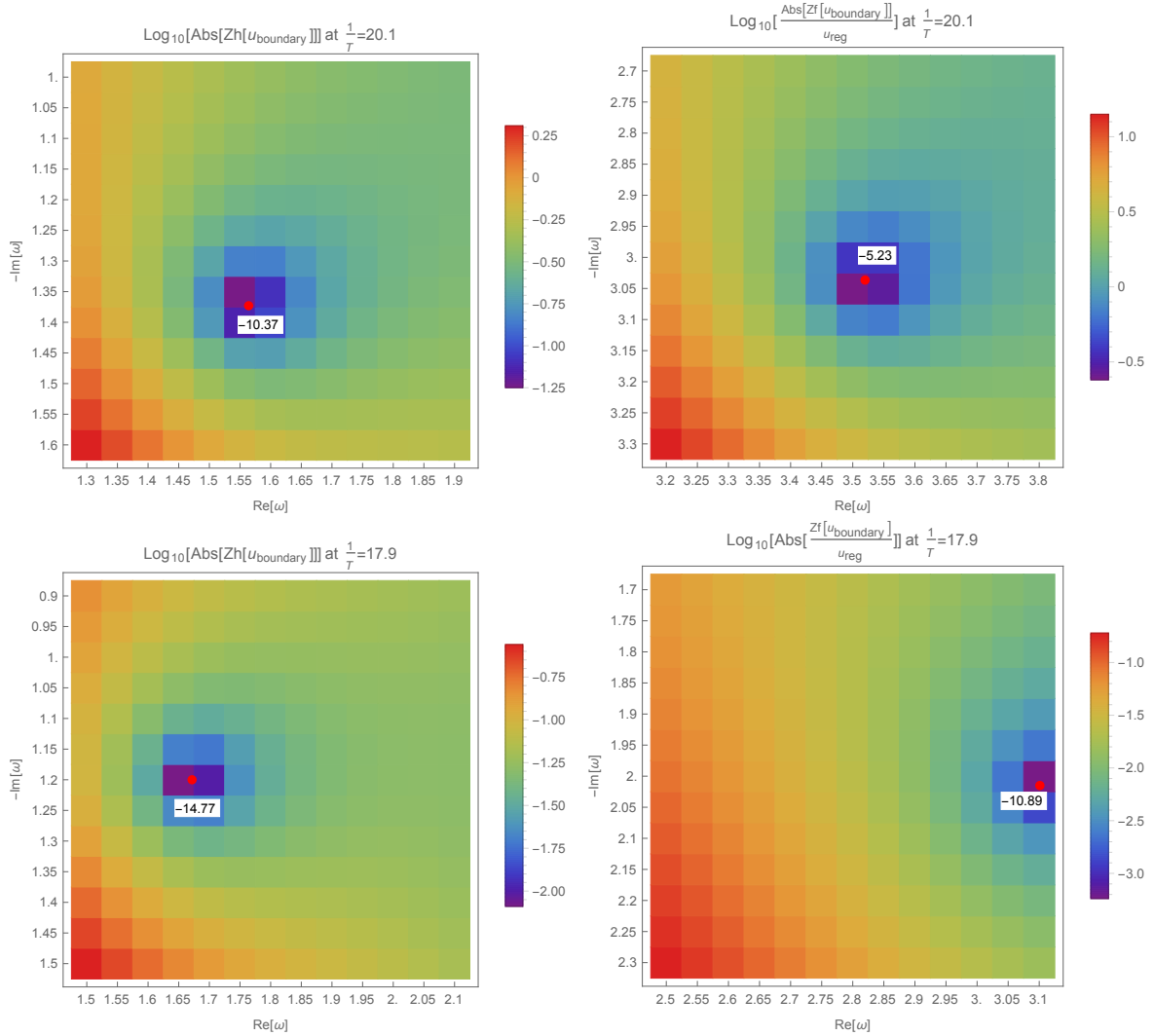
Figure 3.9: Heat-map on the parameter space of frequencies for the value at the boundary of the radial profiles of the gauge-invariant fluctuations, obtained by integrating the equations from the horizon. The top panels correspond to the theroy with $\phi_M = 1$, and the bottom ones to $\phi_M = 3$. At the same time, the left panels correspond to the $\mathcal{Z}_{aniso}$ and the right ones to $\mathcal{Z}_{bulk}$. The red dots indicate the values obtained with the spectral decomposition method and their residual at the boundary, which are zero up to 10 digits.

3.4.3 Results

The QNM frequencies depend on the temperature of the plasma. As the temperature changes, each of these complex frequencies follows some trajectory in the complex plane. In Fig. 3.10 we show these trajectories for the four lowest QNMs of the anisotropic perturbations $\mathcal{Z}_{\text{aniso}}$ for different values of ϕ_M. Each of the points on a given trajectory corresponds to a different value of the temperature. Note that in all panels these trajectories begin and end at the same value, indicated by the crosses, "$+$". The reason for this is that the $\mathcal{Z}_{\text{aniso}}$ fluctuations correspond in the gauge theory to fluctuations exclusively of the stress tensor (i.e. with no contribution of the scalar operator). Since the stress tensor is conserved, its dimension is exactly 4 both at the UV and at the IR fixed points regardless of the value of ϕ_M. In a CFT, this information of an operator alone would determine the spectrum of the dual QNMs. Since our theory approaches a CFT in the UV and in the IR, the QNMs associated to the pure-stress-tensor fluctuations $\mathcal{Z}_{\text{aniso}}$ approach the same limiting conformal values at high and low temperatures. In contrast, at intermediate temperatures all the QNM frequencies possess a smaller imaginary part than their conformal counterparts. The magnitude of this deviation depends on the non-conformality of the theory. For $\phi_M = 1$, when the non-conformal parameter I, defined in (3.45), is small at all temperatures, the complex plane trajectories of all modes remain close to the conformal value. As ϕ_M increases the excursion of all modes in the complex plane deviates more from the conformal values. Note, however, that these paths seem to saturate at very high value of the parameter ϕ_M. In particular, even though the change in the number of IR degrees of freedom differs by more than 3 orders of magnitude, the excursion in the complex plane of the simulations with $\phi_M = 10$ and $\phi_M = 100$ are very similar. This is in accordance with the small change in non-conformality observed in Fig. 3.5.

In Fig. 3.11 we show the complex-plane trajectories of the four lowest QNMs of the bulk mode $\mathcal{Z}_{\text{bulk}}$ as a function of temperature for different values of ϕ_M. In all panels, the blue "$+$" crosses show the QNMs of a probe scalar field in an AdS black brane background dual to a CFT scalar operator of dimension 3 [100]. Similarly, the red "$\square$" squares show the QNMs of a probe scalar field in an AdS black brane background dual to an operator of dimension Δ_{IR} given by (3.14). Since this dimension depends on ϕ_M, the position of the red "$\square$" squares changes from panel to panel. Based on our discussion of the $\mathcal{Z}_{\text{aniso}}$ QNMs above, one may expect that in the case of $\mathcal{Z}_{\text{bulk}}$ the trajectories begin at the blue crosses at high temperature and end at the red crosses at low temperature. However,
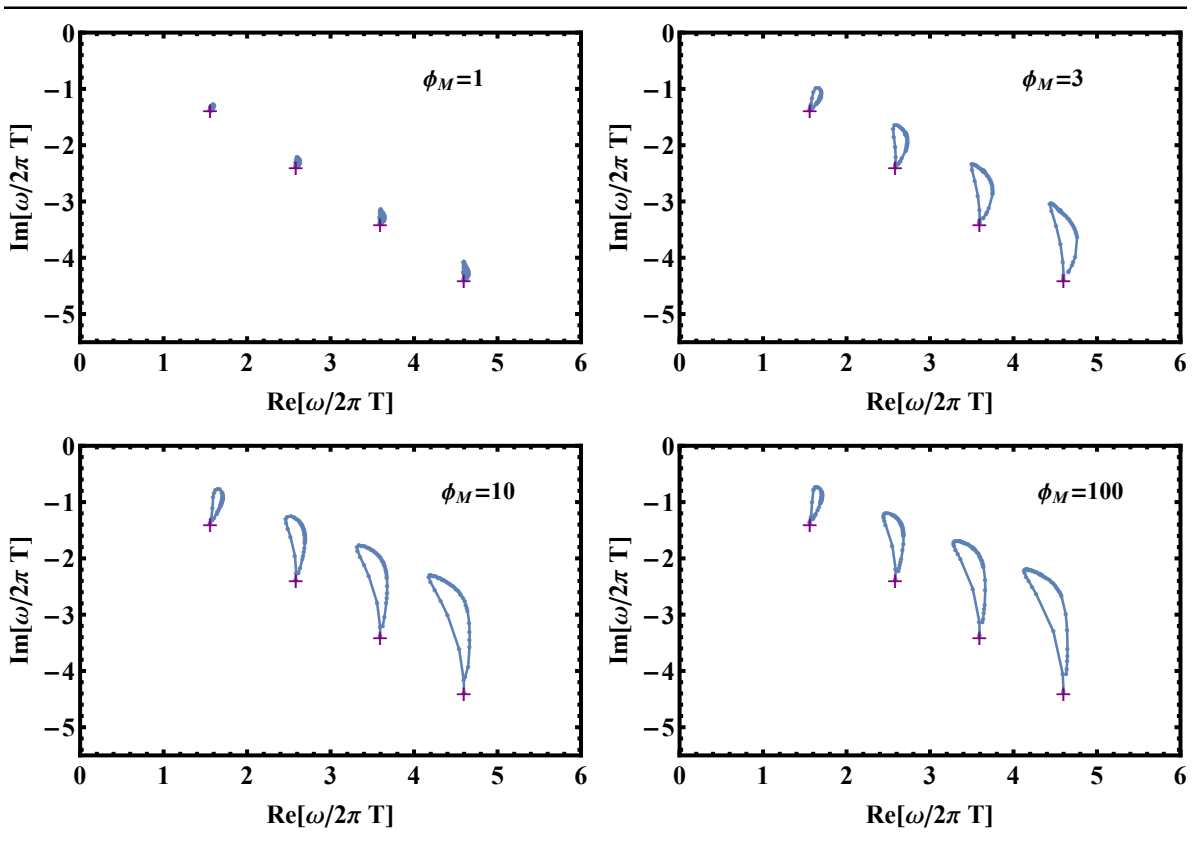
Figure 3.10: Complex plane trajectories of the four lowest QNMs of the $\mathcal{Z}_{\mathrm{aniso}}$-channel for different values of ϕ_M. The "+" crosses mark the position of the QNM of thermal AdS_5 in this channel. We only show the QNMs with positive real part of the frequency.

as we can see from Fig. 3.11, the trajectories in this case possess a more interesting structure.

In the upper left panel of Fig. 3.11 we show the trajectories for the $\phi_M = 1$ potential. For this value, the effective IR mass of the scalar is such that the first two QNMs of the ultraviolet probe scalar are closer to the real axis than the first QNM of the infrared probe scalar. This ordering determines the trajectories of the QNMs as a function of temperature. As shown in the plot, starting from the IR, the lowest QNM flows towards the closest UV mode in the complex plane, which in this case is the second UV mode. All IR modes follow similar trajectories in such a way that (at least as far as our numerics can resolve) the n-th IR mode flows to the $(n+1)$-th ultraviolet mode.[9] As a consequence, there are no available IR modes to which the lowest UV mode can flow into. Therefore, this mode decouples at low temperature, flowing deep intro the complex imaginary plane.

For the other values of ϕ_M displayed in Fig. 3.11, the positions of the IR and the UV modes alternate in the complex plane, but this does not mean that the flow induced by the temperature is a direct map between these two sets of modes. Even though for the remaining three panels the lowest QNM flows between the lowest modes of the IR and UV theories, in all panels there is always a mode that decouples from the spectrum, although that mode is different for each of the displayed values of ϕ_M. The origin of this decoupling is that, after a certain mode, the n-th IR mode flows to the $(n+1)$-th UV mode, interrupting the trajectory of the n-th UV mode. When this happens, we observe a phenomenon similar to level anti-crossing in quantum mechanics. We have checked that for $\phi_M = 1000$ (not shown) the complex-plane trajectories are almost identical to the $\phi_M = 100$ trajectories displayed in the bottom-right panel of Fig. 3.11. This suggests that the observed structure saturates at large ϕ_M and is captured by the $\phi_M = 100$ plot.

In Fig. 3.12 we show the temperature dependence of the imaginary (left) and real (right) parts of the first four quasi-normal frequencies for different values of ϕ_M. Each plot shows the QNM of the anisotropic (blue) and bulk (red) channels. As already discussed, both of these two sets of modes flow from their values in the UV fixed point to their values in the IR fixed point. As shown in the plots, the effective conformal behaviour of the QNMs at high temperature stops when the temperature becomes of order the source Λ. At higher temperatures, the temperature dependence of both the real and imaginary part of the modes is non-trivial, and it reflects the intricate trajectories in

---

[9]We have tested this behaviour for the first 8 QNMs.

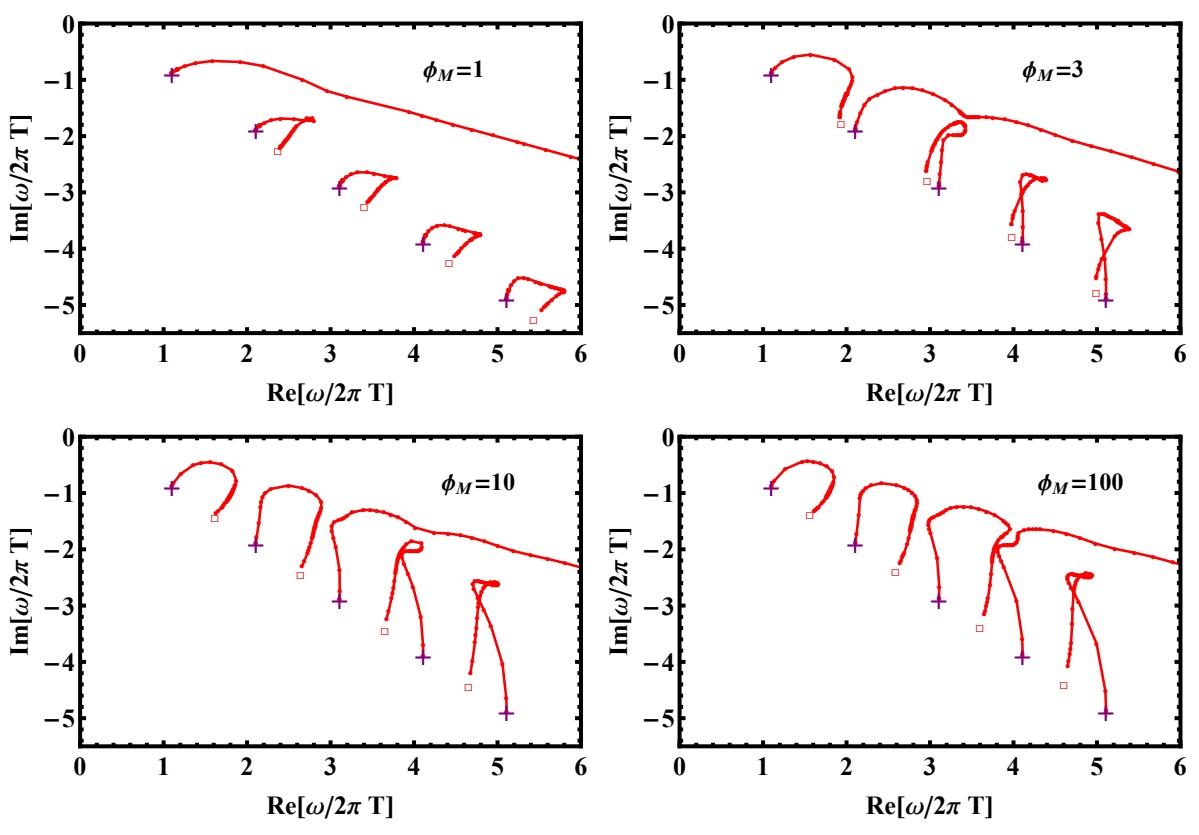**Figure 3.11:** Complex-plane trajectories of the four lowest QNMs of the $\mathcal{Z}_{\text{bulk}}$-channel for different values of ϕ_M. The "+" crosses ("□" squares) mark the position of the QNM of a probe scalar in an AdS black brane background dual to an operator of dimension $\Delta = 3$ ($\Delta = \Delta_{\text{IR}}$). We only show the QNMs with positive real part of the frequency.

the complex plane displayed in Fig. 3.11 and Fig. 3.10. These plots also show explicitly how the disappearance of one bulk QNM occurs at low temperature. The fact that this disappearance seems to be linear in all plots in Fig. 3.12 clarifies the temperature dependence of this mode. The observed constant slope implies that this quasi-normal frequency becomes temperature-independent at low temperature (we have explicitly checked this) and therefore it decouples from the IR theory.

As a final remark, we note that the numerical results displayed in Fig. 3.12 allow us to compare the magnitude of the different modes at the same temperature. As we will discuss in more detail in the next section, the imaginary part of the quasi-normal frequencies is related to the relaxation back to equilibrium of small plasma perturbations. It is interesting to note that the ordering of the imaginary parts of the anisotropic and bulk modes changes with temperature: while at high temperatures the imaginary part of the lowest bulk mode is smaller than that of the anisotropic mode, at low temperatures this order is reversed. This crossing of the imaginary parts of the lowest modes is present for all values of ϕ_M. Nevertheless, at $\phi_M = 1$ this effect is much more prominent, since for this ϕ_M the disappearing QNM is the lowest bulk mode at high temperature. In the next section we will discuss the consequences of this behaviour.

3.5 Discussion

The behaviour of the QNM with smallest imaginary part, dubbed the lowest QNM, is particularly relevant for understanding the off-equilibrium dynamics of theories with a gravity dual. At non-zero spatial momentum, the lowest QNM of metric perturbations is dual to hydrodynamic excitations of the dual theory. However, in the zero-spatial momentum limit we have considered, the residues of the hydrodynamic poles vanish. In this limit the relaxation back to equilibrium is controlled by the QNM frequencies, with the longest-lived excitation corresponding to the lowest QNM. We will refer to the inverses of the imaginary parts of the frequencies of the lowest QNMs in the different channels as relaxation times. In the non-conformal theory that we have studied, these important time scales have a very interesting behaviour.

As shown in Fig. 3.12, the relaxation time associated to the anisotropic and bulk channels have a non-trivial temperature dependence, as a consequence of non-conformality. To best understand the origin of this temperature dependence, following [37, 83] in Fig. 3.13 we show the imaginary part of the lowest QNM as a function of $\delta = 1/3 - c_s^2$ for the
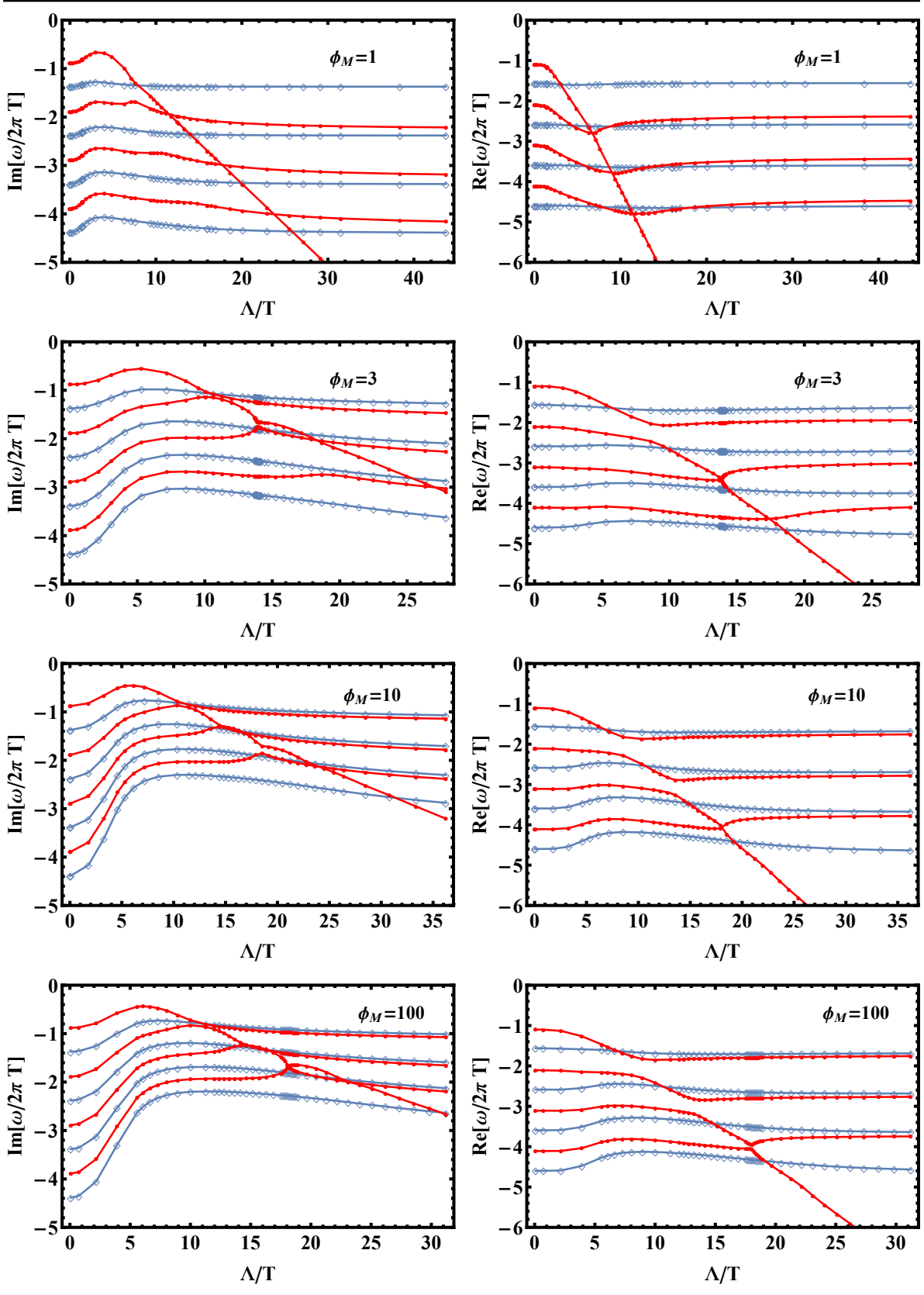
Figure 3.12: Temperature dependence of the real part (right) and the imaginary part (left) of the four lowest QNMs of the $\mathcal{Z}_{\text{bulk}}$-channel (red, closed symbols) and $\mathcal{Z}_{\text{aniso}}$-channel (open, blue symbols).
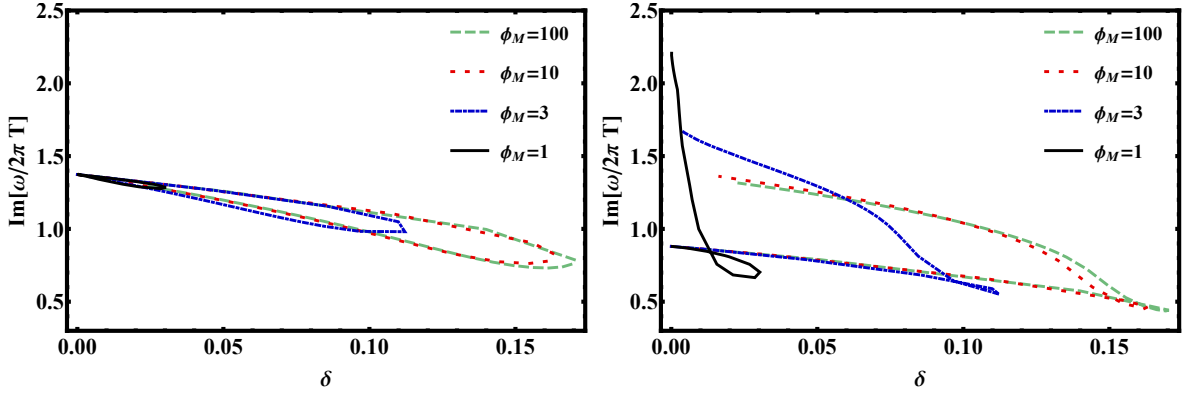
Figure 3.13: Dependence of the imaginary part of the lowest quasi-normal anisotropic (left) and bulk (right) modes on the speed of sound for different potentials. $\delta = 1/3 - c_s^2$.

anisotropic channel (left) and the bulk channel (right) for different values of ϕ_M. For the anisotropic channel, most of this dependence may be understood as a consequence of the change of the speed of sound, similarly to the holographic constructions analysed in [37, 83]. Although the inverse relaxation time is not just a common function of c_s for all models, up to small corrections a simple linear dependence of the imaginary part of the lowest anisotropic mode on $\delta = 1/3 - c_s^2$ provides a good estimate for the relaxation time in this channel. This simple approximate scaling does not work in the bulk channel, as shown in the right panel of Fig. 3.13. Unlike the anisotropic channel, the relaxation time is influenced significantly by the change in the scaling dimension of the scalar operator in the high and low temperature phases, which enters only indirectly into thermodynamic properties such as c_s. Therefore, the relaxation of strongly coupled gauge theories is, in general, not just controlled by thermodynamic properties, but additional microscopic dynamics of the theory may also be important to understand this complicated process.

The different behaviour of these time scales reflects the fact that the way in which the system relaxes depends on the way it is excited. To focus the discussion, we will restrict ourselves to generic excitations of the stress tensor of the system. Since in a CFT the trace of the stress tensor vanishes by symmetry, in a CFT this trace cannot be affected by fluctuations of the bulk mode. Since in addition the bulk mode is isotropic, it follows that the stress tensor itself in a CFT cannot be affected by the bulk mode. Because of this decoupling, the relaxation of small excitations of the stress tensor is controlled solely by the lowest mode of the anisotropic channel, given by the $\delta = 0$ intercept of Fig. 3.13 (left). In a non-conformal theory, however, this decoupling does not occur. Because of non-conformality, the fluctuations of the stress tensor and of the operator $\mathcal{O}$ mix. As an example, note that small isotropic variations of the pressure of the system, which at

finite momentum are part of the sound channel, excite the bulk mode, as it can be easily inferred from the Ward identity (3.44). More generally, the variation of the stress tensor associated to the two fluctuating channels (3.53)-(3.54) is given by

$$\Delta\epsilon = 0, \tag{3.60}$$

$$\Delta p_z = \frac{1}{3}\Lambda^4 \left(\mathscr{Z}^{(3)}_{\text{bulk}} + 4\mathscr{Z}^{(4)}_{\text{aniso}} \right), \tag{3.61}$$

$$\Delta p_\perp = \frac{1}{3}\Lambda^4 \left(\mathscr{Z}^{(3)}_{\text{bulk}} - 2\mathscr{Z}^{(4)}_{\text{aniso}} \right), \tag{3.62}$$

$$\Delta \langle \mathcal{O} \rangle = \Lambda^3 \mathscr{Z}^{(3)}_{\text{bulk}}, \tag{3.63}$$

where Δp_z and $\Delta p_\perp$ are the diagonal components of the stress tensor along the direction of the anisotropic perturbation and perpendicular to it, and $\mathscr{Z}^{(3)}_{\text{bulk}}$ and $\mathscr{Z}^{(4)}_{\text{aniso}}$ are the normalisable modes of the perturbations. These expressions show explicitly how both channels affect the dynamics of the pressure, while only the bulk channel affects the expectation value of the scalar operator. As a consequence, the relaxation of the stress tensor of the system will be dominated by the mode with the smallest imaginary part of the two sets of towers displayed in Fig. 3.12. As it can be seen in this plot, for all values of ϕ_M, relaxation is dominated by different modes at high and low temperatures. The competition between these two channels implies that the relaxation dynamics in our family of holographic models follows different paths at high and low temperatures.

The contributions of the anisotropic and the bulk modes to the stress tensor codify two different physical processes. As explained above, the anisotropic mode controls anisotropic perturbations of the pressure that leave unaffected the energy density, the expectation value of the scalar operator, the average pressure and the trace of the stress tensor. The bulk mode controls fluctuations that change the three pressures in an isotropic way and at the same time modify the expectation value of the scalar operator and the relation between the energy density and pressure given by the equation of state. The relaxation of a generic small stress tensor disturbance therefore requires two distinct process: the "isotropisation" of the system, which amounts to equating the diagonal spatial components of the stress tensor (pressures); and the "EoSization" of the system, with which we only refer to the process by which the trace of the stress tensor attains its equilibrium value. We have carefully defined these two terms to avoid any possible confusion with "thermalization", namely the process by which a system reaches perfect thermal equilibrium.

Consider first the case in which the bulk mode dominates the relaxation process, meaning that its associated lowest QNM decays faster than that associated to the anisotropic mode. In this case the system first relaxes the trace of the stress tensor, such that the pressures of the system no longer fluctuate independently, and only later equates the value of all the pressures to one another. In other words, the system first EoSizes and subsequently isotropizes. This is the behaviour of the holographic models at small values of ϕ_M, such as $\phi_M = 1, 3$, at low temperatures. Since in CFTs the trace of the stress tensor is fixed, this relaxation path is very similar to that in CFTs.

In contrast, consider now the opposite case in which relaxation is dominated by the anisotropic mode, meaning that its associated lowest QNM decays faster than that associated to the bulk mode. In this case the pressure of the system is first isotropized to a value that is not related to the energy density through the equation of state, and only later the subsequent dynamics of this isotropic stress tensor relaxes this value of the pressure to that dictated by the equation of state. At high temperatures, this is the path to equilibration followed by our models, which differs qualitatively from the conformal case.[10]

Finally, when the two relaxation times are comparable, as it is the case in the low temperature regime for large values of $\phi_M = 10, 100$, both of these processes occur simultaneously.

Our calculations are done at zero spatial momentum. At non-zero k the analysis is more complicated because the anisotropic mode splits into the shear, the tensor and the sound modes, and the latter mixes with the bulk mode. Nevertheless, in the coupled bulk-sound system it is still possible to distinguish between those excitations that change the trace of the stress tensor and those that do not. These coupled dynamics will of course modify the EoSization and the isotropization times that we have computed. However, by continuity this modification must be small for small k. Since the QNM frequencies are parametrically of order T, we therefore expect that their ordering will remain the same provided $k \ll T$.

Although the analysis of QNMs can only provide definite answers for the fate of small perturbations off-equilibrium, the rich structure exhibited in this relaxation process has implications for the dynamics of initial configurations that are far off-equilibrium. As we mentioned above, the numerical analyses of collisions in $\mathcal{N} = 4$ SYM yield

---

[10]Note that the right-hand side of (3.22) may suggest that $\Lambda \langle \mathcal{O} \rangle$ must be large in order to cause a significant violation of the equation of state, thus in possible conflict with the linear approximation. It would be interesting to explore this in a non-linear calculation.

hydrodynamisation times that are comparable to the relaxation times obtained via a QNM analysis. While the microscopic explanation of this observation is not understood, this experience has led the authors of [39] to suggest that the hydrodynamisation of non-conformal theories is basically controlled by the temperature of hydrodynamisation, with small (non-parametric) differences with respect to the conformal case. Following this reasoning, we may estimate how much longer the hydrodynamisation can be in the family of theories that we have studied. Given the mixing of the bulk and anisotropic modes, this longest relaxation is given by the absolute minimum of the (negative) imaginary part of the QNM sets which, as shown in Fig. 3.12, is always controlled by the bulk mode. Comparing with the relaxation of conformal theories $\tau_{\mathrm{conf}} = 0.73/2\pi T$, this maximal relaxation is $\tau_{\mathrm{max}}/\tau_{\mathrm{conf}} = 2.1,\ 2.5,\ 3.0,\ 3.15$ for $\phi_M = 1,\ 3,\ 10,\ 100$. These maxima occur at $T/\Lambda = 0.33,\ 0.19,\ 0.16,\ 0.16$ for each model respectively. It would be interesting to test explicitly whether the connection with the linearised analysis persists in full numerical simulations of shock collisions in our non-conformal backgrounds. In particular, this would allow the study of the impact of the different relaxation channels on the on-set of hydrodynamic behaviour.

Chapter 4

Shock-wave collisions in non-conformal theories

In order to make closer contact with the QGP at heavy ion colliders, it is important to understand the far from equilibrium dynamics and the relaxation process in non-conformal field theories. Recent hydrodynamic simulations showed that, indeed, one needs to take into account non-conformal effects to best match the data collected in the experiments[73]. Nevertheless, all far from equilibrium holographic studies of hydrodynamization until the publication this work (see e.g. [54, 55, 57, 80, 101, 102]) have been performed in conformal field theories. In this chapter we present the first holographic shock-wave collision simulation in a non-conformal set-up and study the subsequent hydrodynamization process.

As we discussed in chapter 3, one crucial difference between the two cases is that in non-conformal theories the equation of state, the relation between the energy density and the average pressure, is not fixed by symmetry, and hence it needs not be obeyed out of equilibrium. The relaxation process therefore involves an additional channel, namely the evolution of the energy density and the average pressure towards asymptotic values related by the equation of state. One of the purposes of of this work is to show that hydrodynamization can occur before EoSization. Additionally, this first example of holographic shock-wave collisions in a non-conformal will pave the way for future studies considering phase transitions and critical behaviour.

We will consider gravitational shock-wave collisions in the five-dimensional bottom-up model presented in chapter 3, consisting of gravity coupled to a scalar field with a non-trivial potential. The dual gravity solution describes a domain-wall geometry that interpolates between two AdS spaces. We emphasize that our choice of model is not

guided by the desire to mimic detailed properties of quantum chromodynamics but by simplicity. The UV fixed point guarantees that holography is on its firmest footing, since the bulk metric is asymptotically AdS; the IR fixed point guarantees that the solutions are regular in the interior; and turning on a source for a relevant operator is the simplest way to break conformal invariance.

The numeric code used for the evolutions presented in this chapter is written in C, and it was elaborated in a collective effort by the members of the collaboration.

4.1 The set-up

4.1.1 Model and vacuum solution

We recall the action for our Einstein-scalar model,

$$S = \frac{2}{\kappa_5^2} \int d^5x \sqrt{-g} \left[\frac{1}{4}\mathcal{R} - \frac{1}{2} \left(\nabla \phi \right)^2 - V(\phi) \right] . \tag{4.1}$$

The dynamic equations resulting from it read

$$\mathcal{R}_{\mu\nu} - \frac{\mathcal{R}}{2} g_{\mu\nu} = 8\pi T_{\mu\nu} , \tag{4.2}$$

$$\Box \phi = \frac{\partial V}{\partial \phi} , \tag{4.3}$$

where

$$8\pi T_{\mu\nu} = 2\partial_\mu \phi \partial_\nu \phi - g_{\mu\nu} \left(g^{\alpha\beta} \partial_\alpha \phi \partial_\beta \phi + 2V(\phi) \right) , \tag{4.4}$$

and κ_5 is the five-dimensional Newton constant. The potential $V(\phi)$ sets the details of the dual gauge theory; we choose the same simple potential as in chapter 3 characterised by a single parameter, ϕ_M, which reads

$$L^2 V(\phi) = -3 - \frac{3}{2}\phi^2 - \frac{1}{3}\phi^4 + \left(\frac{1}{2\phi_{\mathrm{M}}^4} + \frac{1}{3\phi_{\mathrm{M}}^2} \right) \phi^6 - \frac{1}{12\phi_{\mathrm{M}}^4}\phi^8 . \tag{4.5}$$

Note that $V(\phi)$ is negative, possesses a maximum at $\phi = 0$ and a minimum at $\phi = \phi_M > 0$. We will set L = 1 throughout, but we will sometimes write L explicitly in some expressions

and plots to prevent ambiguity. The dynamic equations (4.4) are the ones we will solve in a characteristic formulation to simulate the shock-wave collisions.

The gravitational waves we will collide propagate in the vacuum solution of the theory. To compute this vacuum state one needs to first set an ansatz for the solution, in the same way we did in chapter 3. In this case, however, it is convenient to use the holographic coordinate $u_{FG} = 1/r_{FG}$ for computational purposes. In Fefferman-Graham coordinates, the solution with translation invariance and no horizon can be written in the following form,

$$ds^2 = \frac{du_{FG}^2}{u_{FG}^2} + e^{2A_{FG}(u_{FG})}\eta_{\mu\nu}\,dx^\mu dx^\nu \, , \tag{4.6}$$

being $A_{FG}(u_{FG})$ and $\phi(u_{FG})$ the non-trivial fields characterising the solution. The computation of the vacuum state can be simplified when the potential is derived from a super-potential as

$$V(\phi) = -\frac{4}{3}W(\phi)^2 + \frac{1}{2}W'(\phi)^2 \, , \tag{4.7}$$

which for the potential selected (4.5) will be

$$L\,W(\phi) = -\frac{3}{2} - \frac{\phi^2}{2} + \frac{\phi^4}{4\phi_M^2} \, . \tag{4.8}$$

Using the coordinate u_{FG}, the scalar profile $\phi(u_{FG})$ and the metric coefficient $A_{FG}(u_{FG})$ can be obtained from the first order equations

$$-u_{FG}^2 \frac{d\,A_{FG}}{du_{FG}} = -\frac{2}{3}W, \quad -u_{FG}^2 \frac{d\,\phi}{du_{FG}} = \frac{\partial W}{\partial \phi} \, , \tag{4.9}$$

and normalizability boundary conditions. Luckily enough, the equations have an analytic solution for the super-potential chosen,

$$e^{2A_{FG}} = \frac{\phi_0^2}{\phi^2}\left(1 - \frac{\phi^2}{\phi_M^2}\right)^{\frac{\phi_M^2}{6}+1} e^{-\frac{\phi^2}{6}} \, , \tag{4.10}$$

$$\phi = \frac{\phi_0\,u_{FG}}{\sqrt{1 + \frac{\phi_0^2}{\phi_M^2}u_{FG}^2}} \, , \tag{4.11}$$

where ϕ_0 is an arbitrary constant that controls the magnitude of the non-normalizable mode of the scalar field, and is equal to Λ of chapter 3. In this chapter, we use a different name for this constant to emphasize the gravitational description and make contact with the code details explained in the following section. We recall that the presence of this source breaks conformal invariance explicitly.

4.1.2 Gauge theory quantities

Henceforth we will omit the expectation value signs and work with the rescaled quantities following the usual conventions used in the literature,

$$(\mathcal{E}, J_{\mathcal{E}}, P_{x^i}, \mathcal{V}) = \tfrac{\kappa_5^2}{2L^3}(-T_t^t, T_t^z, T_{x^i}^{x^i}, \mathcal{O})\,. \tag{4.12}$$

In these variables the Ward identity takes the form

$$\mathcal{E} - 3\bar{P} = \Lambda\mathcal{V}\,, \tag{4.13}$$

where

$$\bar{P} = \frac{1}{3}\sum_i P_{x^i} \tag{4.14}$$

is the average pressure. Out of equilibrium the average pressure is not determined by the energy density because the scalar expectation value $\mathcal{V}$ fluctuates independently. In contrast, in equilibrium $\mathcal{V}$ is determined by the energy density and the Ward identity becomes the equation of state

$$\bar{P} = P_{\text{eq}}(\mathcal{E})\,, \tag{4.15}$$

with

$$P_{\text{eq}}(\mathcal{E}) = \tfrac{1}{3}\left[\mathcal{E} - \Lambda\mathcal{V}_{\text{eq}}(\mathcal{E})\right]\,. \tag{4.16}$$

4.1.3 Shockwave metric

In the Fefferman-Graham frame it is possible to find a quasi-analytic solution for a single travelling shockwave on a vacuum background. The metric form will simply correspond

to the vacuum metric (4.6) plus the addition of the term $f(u_{FG})h(x_\pm)dx_\pm^2$,

$$ds^2 = \frac{du_{FG}^2}{u_{FG}^2} + f(u_{FG})h(x_\pm)dx_\pm^2 + e^{2A_{FG}(u_{FG})}\left(-dx_+dx_- + d\mathbf{x}_\perp^2\right), \qquad (4.17)$$

where $x_\pm = z \pm t$, z is the direction of propagation of the shock-wave, and $\mathbf{x}_\perp$ are the perpendicular directions to it. The function $h(x_\pm)$ is an arbitrary function for the waveform.

The propagation of the shockwave at the speed of light will not alter the vacuum profiles of $A_{FG}(u_{FG})$ and $\phi(u_{FG})$, and thus the only remaining function to be fully determine the solution will be $f(u_{FG})$. Unfortunately, the equation for $f(u_{FG})$ is a not-so-simple second order differential equation (an ODE) coming from the Einstein's equations which solution can only be obtained numerically,

$$-f\left[2\left(u_{FG}^2\frac{\partial^2 A_{FG}}{\partial u_{FG}^2} + u_{FG}\frac{\partial A_{FG}}{\partial u_{FG}}\right) + 4\left(-u_{FG}\frac{\partial A_{FG}}{\partial u_{FG}}\right)^2\right] + u_{FG}^2\frac{\partial^2 f}{\partial u_{FG}^2} + u_{FG}\frac{\partial f}{\partial u_{FG}} = 0.$$
$$(4.18)$$

From the differential equation one can derive an equivalent integral expression, equally unable to give an analytic form for $f(u_{FG})$,

$$f(u_{FG}) = 4\, e^{2A_{FG}(u_{FG})} \int_0^{u_{FG}} \frac{d\tilde{u}}{\tilde{u}}\, e^{-4A_{FG}(\tilde{u})}. \qquad (4.19)$$

An additional difficulty for the computation of the function $f(u_{FG})$ is that it grows exponentially with u_{FG}. However, this can be solved by computing the redefined function $g(u_{FG}) = e^{2A_{FG}(u_{FG})}f(u_{FG})$—deduced from inspecting (4.19)—which takes values between 0 and 1. In this case, we have chosen a simple Runge-Kutta 4 method to solve the equation.

As a final remark, we note that when solving equation (4.19) order by order close to the boundary, we see that $f(u_{FG})$ behaves as

$$f(u_{FG}) = u_{FG}^2 + \frac{u_{FG}^4\phi_0^2}{9} + \mathcal{O}\left(u_{FG}^6\right). \qquad (4.20)$$

With this expression, the metric (4.17), and the vacuum profile of the scalar field (4.11), one obtains from (3.20)-(3.21) the dual gauge theory quantities of such a shockwave,

namely

$$\mathcal{E} = P_L = \pm J_{\mathcal{E}} = h(x_\pm)\,, \qquad P_T = 0\,, \qquad \mathcal{V} = 0\,, \qquad (4.21)$$

where P_L is the longitudinal pressure (along the z-direction), and P_T the transverse pressure (along the transverse directions $\mathbf{x}_\perp$).

4.2 Numerical procedure

In this section we detail the formalism and the numerical procedure used to evolve the shock-wave collisions in this set-up. This procedure shares many features with the pure gravity simulations and the baryon charged collisions, although there are important differences we will stress in the text.

4.2.1 Evolution equations

We follow the notation of [54] and begin by recalling the 5D Bondi-Sachs metric (1.18) (also dubbed as Eddington-Finkelstein)

$$ds^2 = -A dt^2 + \Sigma^2 \left(e^B d\boldsymbol{x}_\perp^2 + e^{-2B} dz^2 \right) + 2dt(dr + F dz)\,, \qquad (4.22)$$

where A, B, Σ, and F are functions of the radial coordinate r, time t and z. The shocks will be propagating along z, and $\boldsymbol{x}_\perp$ denotes the two perpendicular directions $\boldsymbol{x}_\perp = x_1, x_2$. Note that t is a null time coordinate (usually called v in EF coordinates): $t = \text{const}$ surfaces are null, and not spacelike.

Written in this form, the metric is invariant under the following transformation

$$
\begin{aligned}
r &\to \bar{r} = r + \xi(t,z) \\
\Sigma &\to \bar{\Sigma} = \Sigma \\
B &\to \bar{B} = B \\
A &\to \bar{A} = A + 2\partial_t \xi(t,z) \\
F &\to \bar{F} = F - \partial_z \xi(t,z)
\end{aligned}
\qquad . \qquad (4.23)
$$

Upon plugging the metric (4.22) in (4.2) the resulting system conveniently obeys a particular nested structure, comprising of a sequence of radial ODEs at each $t = \text{const}$ null slice that can be solved in order, see e.g. [45] and references therein.

The equations of motion for our present case are given by

$$\Sigma'' = -\frac{1}{6}\Sigma\left(3\left(B'\right)^2 + 4\left(\phi'\right)^2\right), \tag{4.24a}$$

$$\Sigma^2 F'' = \Sigma\left(6\tilde{\Sigma}B' + 4\tilde{\Sigma}' + 3F'\Sigma'\right) + \Sigma^2\left(3\tilde{B}B' + 2\tilde{B}' + 4\tilde{\phi}\phi'\right) - 4\tilde{\Sigma}\Sigma', \tag{4.24b}$$

$$12\Sigma^3\dot{\Sigma}' = e^{2B}\left[\Sigma^2\left(4\tilde{B}F' - 4\left(\tilde{\tilde{B}} + \tilde{\phi}^2\right) - 7\tilde{B}^2 + 2\tilde{F}' + \left(F'\right)^2\right)\right.$$
$$\left. + 2\Sigma\left(\tilde{\Sigma}\left(F' - 8\tilde{B}\right) - 4\tilde{\tilde{\Sigma}}\right) + 4\tilde{\Sigma}^2\right] - 8\Sigma^2\left(\Sigma^2 V(\phi) + 3\dot{\Sigma}\Sigma'\right), \tag{4.24c}$$

$$6\Sigma^4\dot{B}' = e^{2B}\left[\Sigma^2\left(-\tilde{B}F' + \tilde{B}^2 + \tilde{\tilde{B}} - 2\tilde{F}' + 4\tilde{\phi}^2 - \left(F'\right)^2\right)\right.$$
$$\left. + \Sigma\left(\tilde{\Sigma}\left(\tilde{B} + 4F'\right) + 2\tilde{\tilde{\Sigma}}\right) - 4\tilde{\Sigma}^2\right] - 9\Sigma^3\left(\dot{\Sigma}B' + \dot{B}\Sigma'\right), \tag{4.24d}$$

$$3\Sigma'\Sigma^2\dot{\phi} = -e^{2B}\Sigma\left(2\tilde{B}\tilde{\phi} - \tilde{\phi}F' + \tilde{\tilde{\phi}}\right) + e^{2B}\tilde{\Sigma}\tilde{\phi} + \Sigma^3\left(-\left(V'(\phi) - 2\dot{\phi}'\right)\right) + 3\dot{\Sigma}\Sigma^2\phi', \tag{4.24e}$$

$$6\Sigma^4 A'' = 3e^{2B}\left(\Sigma^2\left(4\left(\tilde{\tilde{B}} + \tilde{\phi}^2\right) + 7\tilde{B}^2 - \left(F'\right)^2\right) + 8\Sigma\left(2\tilde{B}\tilde{\Sigma} + \tilde{\tilde{\Sigma}}\right) - 4\tilde{\Sigma}^2\right)$$
$$+ 2\Sigma^4\left(-9\dot{B}B' + 4V(\phi) - 12\dot{\phi}\phi'\right) + 72\dot{\Sigma}\Sigma^2\Sigma', \tag{4.24f}$$

$$2\Sigma^2\dot{F}' = -\Sigma^2\left(2B'\left(\tilde{A} + 2\dot{F}\right) + 2\tilde{A}' + 6\dot{B}\tilde{B} + 4\dot{\tilde{B}} + 8\dot{\phi}\tilde{\phi} + A'F'\right)$$
$$+ 2\Sigma\left(\Sigma'\left(\tilde{A} + 2\dot{F}\right) - 6\dot{B}\tilde{\Sigma} - 4\dot{\tilde{\Sigma}} - 3\dot{\Sigma}F'\right) + 8\dot{\Sigma}\tilde{\Sigma}, \tag{4.24g}$$

$$6\Sigma^2\ddot{\Sigma} = e^{2B}\left(\Sigma\left(2\tilde{B}\left(\tilde{A} + 2\dot{F}\right) + \tilde{\tilde{A}} + 2\tilde{\dot{F}}\right) + \tilde{\Sigma}\left(\tilde{A} + 2\dot{F}\right)\right)$$
$$+ \Sigma^2\left(3\dot{\Sigma}A' - \Sigma\left(3\dot{B}^2 + 4\dot{\phi}^2\right)\right), \tag{4.24h}$$

where, for any function g, $\tilde{g} \equiv (\partial_z - F\partial_r)\, g$, $g' \equiv \partial_r g$, and

$$d_+ g \equiv \dot{g} \equiv \left(\partial_t + \frac{A}{2}\partial_r\right)g. \tag{4.25}$$

Note that these are all of the general form

$$\left[\alpha_g(r,t,z)\partial_{rr} + \beta_g(r,t,z)\partial_r + \gamma_g(r,t,z)\right]g(r,t,z) = -S_g(r,t,z), \tag{4.26}$$

where $g = \Sigma,\ F,\ d_+\Sigma,\ d_+B,\ d_+\phi,\ A,\ d_+F$. These are solved imposing reflecting boundary conditions at the AdS boundary $u = 1/r = 0$, which take the form

$$A(u,t,z) = \frac{1}{u^2} + \frac{2\xi(t,z)}{u} - 2\partial_t\xi(t,z) + \xi(t,z)^2 - \frac{2\phi_0^2}{3} + \phi_0\partial_t\phi_2(t,z) + u^2 a_4(t,z)$$
$$- \frac{2}{3}u^3(3a_4(t,z)\xi(t,z) + \partial_z f_2(t,z)) + O(u^4) \tag{4.27a}$$

$$B(u,t,z) = u^4 b_4(t,z) + O(u^5) \tag{4.27b}$$

$$\Sigma(u,t,z) = \frac{1}{u} + \xi(t,z) - \frac{\phi_0^2 u}{3} + \frac{1}{3}\phi_0^2 u^2 \xi(t,z)$$
$$+ \frac{1}{54}\phi_0 u^3 \left(-18\phi_0\xi(t,z)^2 - 18\phi_2(t,z) + \phi_0^3\right) + O(u^4) \tag{4.27c}$$

$$F(u,t,z) = \partial_z\xi(t,z) + u^2 f_2(t,z)$$
$$+ u^3 \left(\frac{4}{15}\left(\phi_0\partial_z\phi_2(t,z) - 6\partial_z b_4(t,z)\right) - 2f_2(t,z)\xi(t,z)\right) + O(u^4) \tag{4.27d}$$

$$\phi(u,t,z) = \phi_0 u - \phi_0 u^2 \xi(t,z) + u^3 \left(\phi_0\xi(t,z)^2 + \phi_2(t,z)\right)$$
$$+ u^4 \left(-\phi_0\xi(t,z)^3 - 3\xi(t,z)\phi_2(t,z) + \partial_t\phi_2(t,z)\right) + O(u^5) \tag{4.27e}$$

$$d_+B(u,t,z) = -2u^3 b_4(t,z) + O(u^4) \tag{4.27f}$$

$$d_+\Sigma(u,t,z) = \frac{1}{2u^2} + \frac{\xi(t,z)}{u} + \frac{1}{2}\xi(t,z)^2 - \frac{\phi_0^2}{6}$$
$$+ \frac{1}{36}u^2 \left(18a_4(t,z) + 18\phi_0\phi_2(t,z) - 5\phi_0^4\right) + O(u^3) \tag{4.27g}$$

$$d_+\phi(u,t,z) = -\frac{\phi_0}{2} + u^2 \left(\frac{\phi_0^3}{3} - \frac{3}{2}\phi_2(t,z)\right) + O(u^3) \tag{4.27h}$$

$$d_+F(u,t,z) = \partial_{tz}\xi(t,z) - u f_2(t,z) + O(u^2) \tag{4.27i}$$

The function $\xi(t,z)$ encodes our residual gauge freedom, whereas functions $a_4(t,z)$ and $f_2(t,z)$ are constrained to obey

$$\partial_t a_4 = -\frac{4}{3}\left(\partial_z f_2 + \phi_0\partial_t\phi_2\right), \tag{4.28a}$$

$$\partial_t f_2 = \frac{1}{4}\left(-\partial_z a_4 - 8\partial_z b_4 + \frac{4}{3}\phi_0\partial_z\phi_2\right), \tag{4.28b}$$

with b_4 read from B through (4.27b) and both ϕ_2 and $\partial_t\phi_2$ read from ϕ through (4.27e). At this point is worth to recall that the fall-off coefficients for the dynamic variables in EF coordinates are not the same as the ones in FG, but related through simple relations.

In particular

$$\phi_0 \phi_{2FG} = \phi_{2EF} - \frac{1}{6}\phi_0^3 \tag{4.29}$$

To solve the resulting system we follow the general approach of [42, 54], with some important differences that we will outline in the following sections.

4.2.2 Expectation values from evolution variables

With the near-boundary behaviours above, together with the Fefferman-Graham expansions (3.18) and (3.19), one finds the coordinate transformation relating the falloff coefficients in each frame. With these, and the expectation values (3.20) and (3.21), one can write the expressions for the gauge theory values in terms of our evolution variables (b_4, a_4, f_2, ϕ_2) as

$$\mathcal{E} = -\left(\frac{3}{4}a_4 + \phi_0\phi_2 + \frac{9 - 7\phi_M^2}{36\phi_M^2}\phi_0^4 \right), \tag{4.30}$$

$$P_L = -\frac{a_4}{4} - 2b_4 + \frac{\phi_0\phi_2}{3} + \left(-\frac{5}{108} + \frac{1}{4\phi_M^2} \right)\phi_0^4, \tag{4.31}$$

$$P_T = -\frac{a_4}{4} + b_4 + \frac{\phi_0\phi_2}{3} + \left(-\frac{5}{108} + \frac{1}{4\phi_M^2} \right)\phi_0^4, \tag{4.32}$$

$$J_{\mathcal{E}} = f_2, \tag{4.33}$$

$$\mathcal{V} = -2\phi_2 + \frac{\phi_0^3}{3} - \frac{\phi_0^3}{\phi_M^2}, \tag{4.34}$$

where P_L and P_T are the longitudinal and transverse pressures.

4.2.3 Gauge fixing

We start with the procedure to fix the residual gauge freedom (4.23). A convenient choice is treating $\xi(t, z)$ as another evolved variable and choosing its evolution equation by requiring that the apparent horizon position lie at some constant radial coordinate $r = r_h$. We thus want to impose

$$\Theta|_{r=r_h} = 0, \qquad \partial_t \Theta|_{r=r_h} = 0, \tag{4.35}$$

at all times, where Θ is the expansion of outgoing null geodesics for metric (4.22). At surfaces $r = \text{const}$, Θ is given by

$$\Theta = -\frac{1}{2}e^{2B}F\left(3F\partial_r\Sigma - 2\partial_z\Sigma\right) + e^{2B}\Sigma\left(2F\partial_z B + \partial_z F\right) - 3\Sigma^2 d_+\Sigma. \tag{4.36}$$

A simple way to impose conditions (4.35) numerically is the following

$$\left(\partial_t\Theta + \kappa\Theta\right)|_{r=r_h} = 0\,, \tag{4.37}$$

where κ is a positive parameter typically chosen to be 1. The advantage of imposing such a condition is that it's constructed to drive the $\Theta = 0$ surface back to $r = r_h$ whenever numerical errors accumulate. This turns out to work very well in practice.

Equation (4.37), when expanded, gives us an equation for $\partial_t\xi$ of the form

$$\left[\alpha_\xi(t,z)\partial_{zz} + \beta_\xi(t,z)\partial_z + \gamma_\xi(t,z)\right]\partial_t\xi(t,z) = -S_\xi(t,z)\,, \tag{4.38}$$

to be evaluated at $r = r_h$. This is a second order linear ODE in the coordinate z, which we solve imposing periodicity in z.

4.2.4 Field redefinitions and evolution algorithm

To integrate the resulting system subject to the boundary conditions (4.27), it is very convenient to introduce $u = 1/r$ as our radial coordinate and redefine the evolved variables so that the divergent pieces at $u = 0$ are absent.

Motivated by (4.27), we make the following definitions

$$B(u,t,z) \equiv u^4 B_{g_1}(u,t,z) \tag{4.39a}$$

$$\equiv B_{g_2}(u,t,z) \tag{4.39b}$$

$$\Sigma(u,t,z) \equiv \frac{1}{u} + \xi(t,z) - u\frac{\phi_0^2}{3} + u^2\frac{\phi_0^2}{3}\xi(t,z) + u^3\Sigma_{g_1}(u,t,z) \tag{4.39c}$$

$$\equiv \frac{1}{u} + \xi(t,z) + \Sigma_{g_2}(u,t,z) \tag{4.39d}$$

$$F(u,t,z) \equiv \partial_z\xi(t,z) + u^2 F_{g_1}(u,t,z) \tag{4.39e}$$

$$\equiv \partial_z\xi(t,z) + F_{g_2}(u,t,z) \tag{4.39f}$$

$$A(u,t,z) \equiv \frac{1}{u^2} + \frac{2\xi(t,z)}{u} - 2\partial_t\xi(t,z) + \xi(t,z)^2 - \frac{2\phi_0^2}{3} + u^2 A_{g_1}(u,t,z) \tag{4.39g}$$

$$\equiv \frac{1}{u^2} + \frac{2\xi(t,z)}{u} - 2\partial_t\xi(t,z) + \xi(t,z)^2 - \frac{2\phi_0^2}{3} + A_{g_2}(u,t,z) \qquad (4.39\text{h})$$

$$\phi(u,t,z) \equiv u\phi_0 - u^2\phi_0\xi(t,z) + u^3\phi_0^3\phi_{g_1}(u,t,z) \qquad (4.39\text{i})$$

$$\equiv \phi_0\phi_{g_2}(u,t,z) \qquad (4.39\text{j})$$

$$d_+\Sigma(u,t,z) \equiv \frac{1}{2u^2} + \frac{\xi(t,z)}{u} + \frac{\xi(t,z)^2}{2} - \frac{\phi_0^2}{6} + u^2\dot\Sigma_{g_1}(u,t,z) \qquad (4.39\text{k})$$

$$\equiv \frac{1}{2u^2} + \frac{\xi(t,z)}{u} + \frac{\xi(t,z)^2}{2} - \frac{\phi_0^2}{6} + \dot\Sigma_{g_2}(u,t,z) \qquad (4.39\text{l})$$

$$d_+B(u,t,z) \equiv u^3\dot B_{g_1}(u,t,z) \qquad (4.39\text{m})$$

$$\equiv \dot B_{g_2}(u,t,z) \qquad (4.39\text{n})$$

$$d_+\phi(u,t,z) \equiv -\frac{\phi_0}{2} + u^2\phi_0^3\dot\phi_{g_1}(u,t,z) \qquad (4.39\text{o})$$

$$\equiv -\frac{\phi_0}{2} + \dot\phi_{g_2}(u,t,z) \qquad (4.39\text{p})$$

$$d_+F(u,t,z) \equiv \partial_{tz}\xi(t,z) + u\dot F_{g_1}(u,t,z) \qquad (4.39\text{q})$$

$$\equiv \partial_{tz}\xi(t,z) + \dot F_{g_2}(u,t,z) \qquad (4.39\text{r})$$

Our equations are then rewritten in terms of the "g_1" and "g_2" variables above. g_1 variables are adapted to the AdS boundary $u = 0$. The corresponding resulting equations, however, are extremely long and carry terms with large powers of the coordinate u. Upon trying to solve this system in the whole grid, numerical errors were pilling up very early on in the evolution, quickly spoiling convergence of the solution. We then decided to make use of the system g_1 only in the vicinity of $u \sim 0$ (grid1, spanning $u \in [0, u_0]$) — where a much simpler series expanded version of the aforementioned equations was used — and another grid (grid2, spanning $u \in [u_0, u_h]$) was introduced where the much simpler system of equations g_2 was used instead.

Our numerical grid thus consists of a double grid in the u direction $u \in [0, u_0] \cup [u_0, u_h]$, where u_0 is typically chosen to be 0.1, and $u_h = 1/r_h$ is typically chosen to be 2 or 3. We integrate the g_1 equations with boundary conditions given by (4.27) in grid1; we then read off the integrated values at $u = u_0$ and use these as boundary conditions for integrating the g_2 equations in grid2. Note, however, that we also need to deal with the junction point u_0 in our u-dependent hyperbolic equations $\partial_t B(u,t,z)$ and $\partial_t \phi(u,t,z)$, given by equation (4.25).

We are now in possession of all the necessary equations for the evolution procedure. The evolution algorithm is then as follows:

1. at any given time t_n (which can be the initial time after having performed the transformation (4.23) that puts the apparent horizon at constant u) we know $B(u, t_n, z)$, $\phi(u, t_n, z)$, $\xi(t_n, z)$, $a_4(t_n, z)$ and $f_2(t_n, z)$;

2. successively solve the elliptic equations (4.24) (or rather, the corresponding system obtained in terms of the redefined "g_1" and "g_2" functions) in the order $\Sigma_{g_{1,2}}$, $F_{g_{1,2}}$, $\dot{\Sigma}_{g_{1,2}}$, $\dot{B}_{g_{1,2}}$, $\dot{\phi}_{g_{1,2}}$, $A_{g_{1,2}}$, which are a sequence of radial ODEs subjected to the boundary conditions (4.27);

3. equation (4.38) is solved to get $\partial_t \xi(t_n, z)$ and afterwards $\partial_t B_{g_{1,2}}(t_n, u, z)$ and $\partial_t \phi_{g_{1,2}}(t_n, u, z)$ can be obtained through equation (4.25) with (4.39g) and (4.39h);

4. obtain $\partial_t a_4(t_n, z)$ and $\partial_t f_2(t_n, z)$ through (4.28) and, together with the already obtained $\partial_t \xi(t_n, z)$, $\partial_t B_{g_{1,2}}(u, t_n, z)$, $\partial_t \phi_{g_{1,2}}(u, t_n, z)$, advance all these quantities to time t_{n+1} with a Runge-Kutta procedure or equivalent.

5. GOTO 1.

4.2.5 Discretization

Equations (4.24) are written in a form that decouples the coordinates u and z (the collision axis) and can therefore be solved as ODEs in the u direction for each point in z. For this reason, both coordinates can be treated separately. The z direction is discretized on a uniform grid where periodic boundary conditions are imposed, while along the u direction we make use of two grids, grid1 spanning $[0, u_0]$ and grid2 spanning $[u_0, u_h]$. Both u grids are *Lobatto-Chebyshev* grids with $N_u + 1$ points, the collocation points are given by

$$X_i = -\cos\left(\frac{\pi\, i}{N_u}\right) \qquad (i = 0, 1, \ldots, N_u)\,, \tag{4.40}$$

are defined in the range $[-1 : +1]$, and can be mapped to our *physical* grid by

$$u_i = \frac{u_R + u_L}{2} + \frac{u_R - u_L}{2} X_i \qquad (i = 0, 1, \ldots, N_u)\,, \tag{4.41}$$

where u_L and u_R are the limits of each of the grids.

As the differential equations are solved in u for each z point, the only important operation performed in the z direction are the partial derivatives present in the equa-

tions (4.24). To evaluate these we use a fourth-order accurate (central) finite difference approximation. Also in this direction, we find spurious high-frequency noise common to any finite differencing schemes. In order to remove it we add numerical dissipation to damp these modes. We have therefore implemented $N = 3$ Kreiss-Oliger dissipation [103] whereby, after each time step, all our evolved quantities $f \in \{B_{g_{1,2}}, \phi_{g_{1,2}}, a_4, f_2, \xi\}$ are added a term of the form

$$D_{\mathrm{KO}} f_i \equiv \frac{\sigma}{64} \left(f_{i-3} - 6 f_{i-2} + 15 f_{i-1} - 20 f_i + 15 f_{i+1} - 6 f_{i+2} + f_{i+3} \right), \qquad (4.42)$$

where i labels the grid point in the z direction and σ is a tuneable dissipation parameter which must be smaller than 1 for stability, and which we have typically fixed to be 0.2. This procedure effectively works as a low-pass filter.

In the radial direction u, the use of the Chebyshev-Lobatto grid allow us to use pseudo-spectral collocation methods (PSC) [104]. These methods are based in the approximation of our solutions in a basis of known functions, Chebyshev polynomials $T_n(X)$ in our case, but, in addition to the spectral basis, we have an additional *physical* representation and therefore we can performed operations in one basis or the other depending of our necessities. Thanks to the trigonometric representation of the Chebyshev polynomials, we can use the Fast Fourier Algorithm (FFT) for changing from one basis to the other. One of the uses of these method is high accuracy interpolation of any function f to values of u not present in our grid. This can be computed using the standard spectral representation of the function

$$f(u) = \sum_{k=0}^{N} \hat{f}_k \, T_k(X(u)), \qquad (4.43)$$

where $\hat{f}_k$ are the coefficients of the spectral basis that are computed from the values of the function in the collocation points through the FFT.

As we mentioned previously, the radial equations for solving the metric coefficients can be written in the form

$$\left[\alpha_g(u, t, z) \partial_{uu} + \beta_g(u, t, z) \partial_u + \gamma_g(u, t, z) \right] g(u, t, z) = -S_g(u, t, z),$$

where, again, g represents the metric coefficients previously mentioned. Once our coordinate is discretized, the differential operator becomes an algebraic one acting over

the values of the functions in the collocation points taking the form

$$\left[\alpha_g^i(t,z)\mathcal{D}_{uu}^{ij} + \beta_g^i(t,z)\mathcal{D}_u^{ij} + \gamma_g^i(u,t,z)\right] g^j(t,z) = -S_g^j(t,z),$$

where $\mathcal{D}_{uu}$, $\mathcal{D}_u$ represent the derivative operator for a Lobatto-Chebyshev grid in the physical representation and i, j indices in the u coordinate. We now construct the operator defined inside the brackets and then invert it to solve the function g. Boundary conditions are imposed by replacing full rows in this operator by the values we need to fix. In the general case, for a second order operator we replace the lines $j = 0$, $j = N$ by the value of the function and its derivative at $u = 0$ in the case of the grid1 and at $u = u_0$ in the case of grid2. At grid1, we obtain the boundary conditions from (4.27); at grid2 these are read off from the obtained values at grid1.

Another useful feature of the spectral methods is the possibility of filtering. As we did with the dissipation in the direction z, we can damp high order modes but in this case directly in the spectral representation. After each time step, we apply an exponential filter to the spectral coefficients of our u-dependent evolved quantities $\hat{f} \in \{\hat{B}_{g_{1,2}}, \hat{\phi}_{g_{1,2}}\}$. The complete scheme is

$$\{f_i\} \xrightarrow{FFT} \left\{\hat{f}_k\right\} \longrightarrow \left\{\hat{f}_k \, e^{-\alpha(k/N_u)^{\gamma N_u}}\right\} \xrightarrow{FFT} \{f_i\} \tag{4.44}$$

where α and γ are tuneable parameters which we typically fix to $\alpha = 36.0437$, $\gamma = 8$. This effectively dampens the coefficients of the higher order Chebyshev polynomials.

4.2.6 Initial data

Our chosen formulation of Einstein's equations, known as the characteristic formulation, allows one to specify the initial data needed for an evolution through freely setting the functions $B(u,z)$, $\phi(u,z)$, $\xi(z)$, $a_4(z)$ and $f_2(z)$. For our intended applications, we wish to have initial data resembling an ultra-relativistic projectile, such as the shockwave metric in AdS. The starting point to construct such initial data is thus the shockwave metric in FG coordinates (4.17). Once the function $f(u_{FG})$ therein is computed, one can proceed to transform the metric to the EF frame (4.22) in which the numerical integration is performed. Owing to the fact that both the FG and the EF metrics have an explicit Killing vector, one can use the following ansatz for the coordinate transformation

between the two frames

$$
\begin{aligned}
\mathbf{x}_\perp^{\mathrm{FG}} &= \mathbf{x}_\perp^{\mathrm{EF}}, & u_{FG} &= u + \lambda_1(u, t+z), \\
x_+ &= t + z + \lambda_2(u, t+z), & x_- &= t - z + \lambda_3(u, t+z),
\end{aligned}
\tag{4.45}
$$

for a left-moving shock [42]. The differential equations for the transformation functions $\lambda_1(u, z)$, $\lambda_2(u, z)$, and $\lambda_3(u, z)$ are obtained by simply taking the slots g_{uu}, g_{ut}, and g_{uz} from the equation

$$
g^{\mathrm{EF}} = \Lambda g^{\mathrm{FG}} \Lambda^T.
\tag{4.46}
$$

Equivalently, one might use the fact that the EF coordinate u is a non-affine parameter for ingoing null geodesics

$$
\partial_u^2 k^\mu(u) + \Gamma^\mu_{\alpha\beta} \partial_u k^\alpha(u) \partial_u k^\beta(u) = F(u) \partial_u k^\mu,
\tag{4.47}
$$

where $k^\mu(u)$ is the parametrized geodesic, and $F(u) = \frac{-2}{25u}$ is a non-affinity function set to meet the desired EF frame with $g_{tr} = 1$. The geodesic equations have the advantage of being explicitly depending on $t + z$ and therefore its solution reduces to a set of ODEs parametrised by the boundary point z for $t = 0$. We thus write our initial data for a left-moving shock with width ω and height $\frac{\mu^3}{\sqrt{2\pi}\omega}$ as

$$
h(z) = \frac{\mu^3}{\sqrt{2\pi}\omega} e^{-\frac{(z-z_0)^2}{2\omega^2}},
\tag{4.48}
$$

$$
\mathcal{E}(z) = \mathcal{E}_0 + h(z),
\tag{4.49}
$$

$$
f_2(z) = h(z),
\tag{4.50}
$$

$$
\phi(u, z) = \frac{\phi_0 u_{FG}}{\sqrt{1 + \frac{u_{FG}^2}{3\phi_0}\left(\phi_0^3 - 6\phi_2\right)}},
\tag{4.51}
$$

$$
e^{3B(u,z)} = \frac{e^{2A_{FG}(u_{FG})}}{\frac{\partial_z \lambda_1^2}{u_{FG}^2} - (\partial_z \lambda_2 + 1)(\partial_z \lambda_3 - 1) e^{2A_{FG}(u_{FG})} + (\partial_z \lambda_2 + 1)^2 f(u_{FG}) h(z)},
\tag{4.52}
$$

where u_{FG}, $\lambda_{1,2,3}$ are functions of u and z obtained from (4.45). $\mathcal{E}$ is the energy density of the boundary field theory and $\mathcal{E}_0$ the corresponding background value (which we typically set to $\mathcal{E}_0 = 0.02 \frac{\mu^3}{\sqrt{2\pi}\omega}$). Having chosen $\mathcal{E}_o$, we know the solution in the absence of shocks (with $B = 0$), and its corresponding z-independent ϕ_2 value, the equilibrium value for the specified energy density. With the above construction, we set ϕ_2 to its equilibrium value (for the given background energy density $\mathcal{E}_0$), and set a_4 trivially set

from (4.30) and (4.49). Function $\xi(z)$ is then set by imposing that the apparent horizon lie at constant u coordinate, and we are ready to start the evolution.

4.3 Code tests

We implement the above construction in a standalone C code, where we use the GSL library to solve the linear system (4.24), and use a fourth-order Adams-Bashforth method to integrate the functions $B(u, z)$, $\phi(u, z)$, $a_4(z)$, $f_2(z)$ and $\xi(z)$ forward in time, using the procedure outlined in section 4.2.4. The code is trivially parallelised with OpenMP. The resulting code is remarkably fast, being able to evolve an standard configuration with $12 + 48$ u-points and $\Delta z = L/20$ (400 z-points) from $t/L = 0$ to $t/L = 1$ in 3 minutes using two cores Intel i7-4820K CPU @ 3.70GHz.

4.3.1 Quasi-normal modes

As a first test to the code and our numerical implementation we have recovered some quasi-normal frequencies reported chapter 3. For these tests, we evolved a $\phi_{\mathrm{M}} = 10$ z-independent configuration where the energy density was set to $\mathcal{E}/\phi_0^4 = 0.379686$. a_4 and ϕ_2 were initialised to their corresponding equilibrium values, whereas B and ϕ were set to

$$B = 0.1u^8 \,, \tag{4.53}$$

$$\phi = \phi_0 u + \phi_2 u^3 \,, \tag{4.54}$$

Since this configuration is not in equilibrium, b_4 and ϕ_2 will oscillate and relax, allowing us to compute the quasi-normal modes (QNM) of the system.

Gravitational set-ups containing a single scalar field will typically show two scalar, independent and gauge invariant types of perturbations, each one with its own tower of modes. Hence, the system will have two independent channels to relax to equilibrium. In the model studied in this work, the two channels control independently the fluctuations of the anisotropy and the trace of the stress-energy tensor of the dual plasma respectively. Since b_4 only contributes to the anisotropy and ϕ_2 only to the trace, their fluctuations will be governed by different towers of modes. Therefore, the frequencies extracted from

b_4 should match the anisotropy tower frequencies' and the ones from ϕ_2 should match the trace, or "bulk", tower.
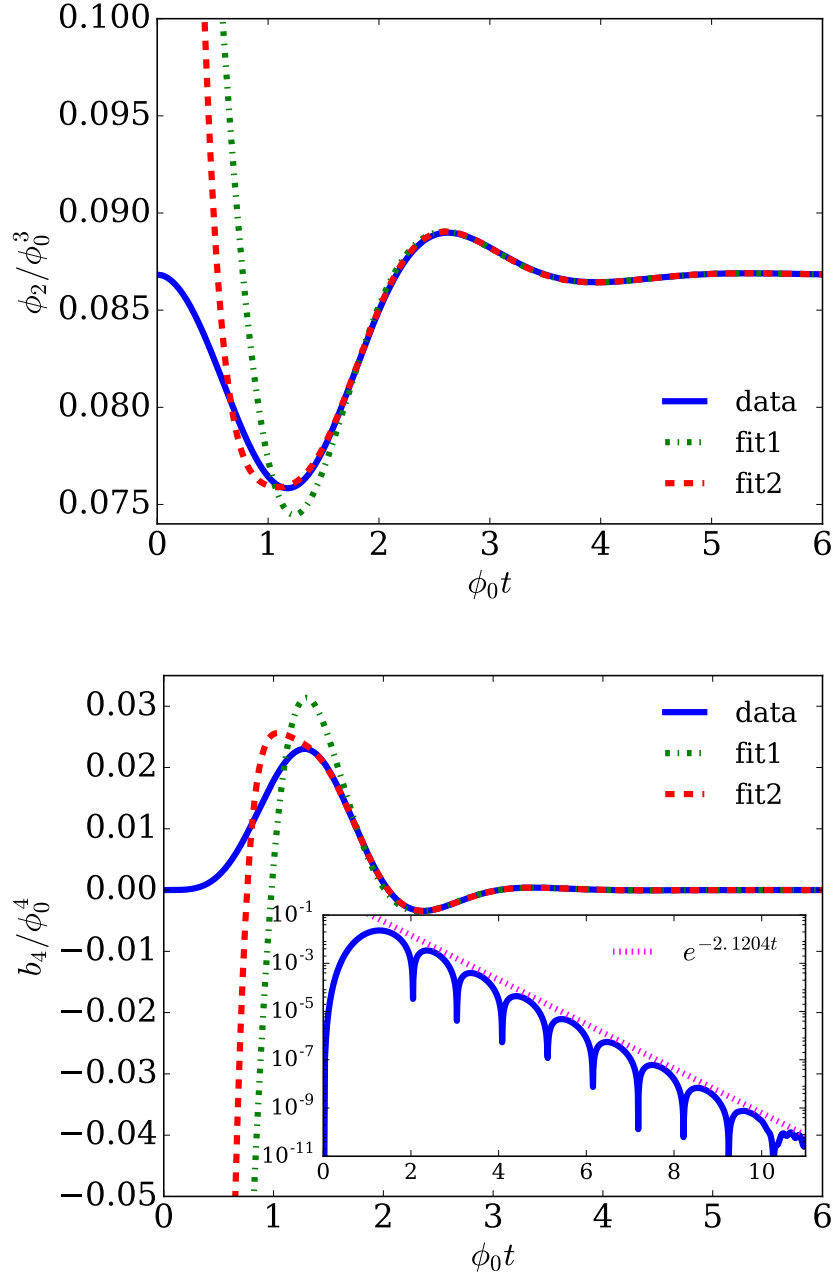

Figure 4.1: ϕ_2 and b_4 as functions of time for a z-independent configuration with $\phi_{\mathrm{M}} = 10$, $\mathcal{E}/L^4 = 0.379686$, with initial data as specified in (4.53). Blue full line corresponds to data from the code, green dash-dotted line correspond to a fit to the data using one QNM, red dashed line corresponds to a fit using two QNMs as explained in the text.

In figure 4.1, we have fitted numerical data with damped sinusoidals of the form

$$f(t) = C + A_1 e^{-\omega_i^{(1)} t} \cos\left(\omega_r^{(1)} t + \varphi_1\right) + A_2 e^{-\omega_i^{(2)} t} \cos\left(\omega_r^{(2)} t + \varphi_2\right). \tag{4.55}$$

In order to recover the frequencies we employed the following strategy. First, we look for the lowest frequency mode; for that, we set $A_2 = 0$ in equation (4.55) and fit this function to our numerical data. We perform a series of fits to the data, each fit starting at a later time: we start by using the whole signal, then use only the portion $t \in [1, \infty[$ (say) of the signal, then only the portion $t \in [2, \infty[$ and so on. The frequencies $\omega^{(1)}$ thus obtained in each fit eventually convergence to some value, the longest lived mode, which we are able to isolate through this process. We then fix the C, A_1, $\omega_r^{(1)}$, $\omega_i^{(1)}$, φ_1 fitting parameters obtained; the corresponding fit is labelled "fit1" in figure 4.1. Having fixed these parameters we then repeat the process using equation (4.55), where this time we *only* allow for the A_2, $\omega_r^{(2)}$, $\omega_i^{(2)}$, φ_2 parameters to vary. We thus obtain the frequencies $\omega^{(2)}$; the final resulting fit is labelled "fit2" in figure 4.1.

The results obtained with this procedure are displayed in figure 4.1. For the non-conformal mode (left panel) we have obtained

$$L\omega_r^{(1)} = 2.31305, \qquad\qquad L\omega_i^{(1)} = 1.26432, \tag{4.56}$$

$$L\omega_r^{(2)} = 4.03, \qquad\qquad L\omega_i^{(2)} = 2.93, \tag{4.57}$$

which are to be compared with $L\omega^{(1)} = 2.313106 + 1.264367i$, $L\omega^{(2)} = 4.108 + 2.93141i$ obtained in [1]. For the anisotropic mode (right panel), we have obtained

$$L\omega_r^{(1)} = 3.03932, \qquad\qquad L\omega_i^{(1)} = 2.12048, \tag{4.58}$$

$$L\omega_r^{(2)} = 4.9, \qquad\qquad L\omega_i^{(2)} = 3.6, \tag{4.59}$$

which are to be compared with $L\omega^{(1)} = 3.03944 + 2.120404i$, $L\omega^{(2)} = 4.934 + 3.7393i$ obtained in [1].

We emphasise that the numbers from [1] and those of this section were obtained in a completely independent way, and the excellent agreement between them (of up to 0.004% for the lowest frequency) validates both the code presented herein as well as the method of [1].
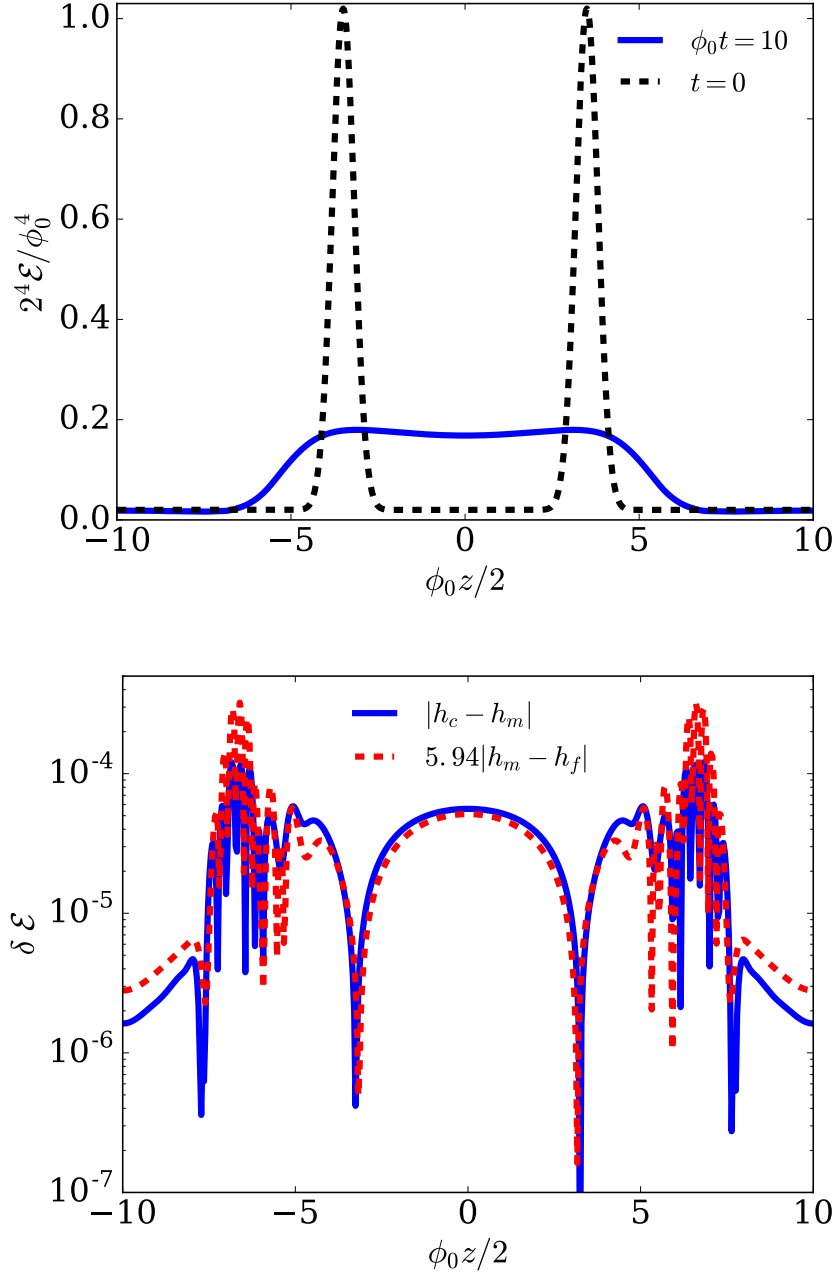
Figure 4.2: Energy density at $t = 10L$ (top panel) and correspondent convergence analysis (bottom panel) for the configuration a typical configuration. We plot the absolute differences between the coarse and medium resolution (blue solid line) and the medium and fine (red dashed line) resolution run. The latter has been re-scaled by the factor $Q = 5.94$ expected for fourth order convergence.

4.3.2 Convergence analysis

Numerical simulations using finite differencing techniques typically approximate the continuum solution of the problem with an error that depends polynomially on the grid spacing h,

$$f = f_h + O(h^n)\,. \tag{4.60}$$

Different numerical implementations will give different convergence orders n. In our case, since we make use of fourth order finite difference stencils, we expect to see $n = 4$. One simple way to check for consistency of a code is evolving the same configuration with coarse, medium and fine resolution, h_c, h_m and h_f. One can then compute a convergence factor given by

$$Q \equiv \frac{f_{h_c} - f_{h_m}}{f_{h_m} - f_{h_f}} = \frac{h_c^n - h_m^n}{h_m^n - h_f^n}\,, \tag{4.61}$$

where f_h is a chosen evolved variable obtained with numerical resolution h. Since in the radial direction we make use of pseudo-spectral methods, our error will be dominated by the resolution used in z direction, to which the grid spacing h alludes to. For the analysis done in this section we therefore always make use of the same resolution in the radial direction.

We have correspondingly evolved the configuration with $h_c = L/20$, $h_m = L/30$ and $h_f = L/40$; the expected convergence factor expected for fourth order convergence would therefore be $Q \approx 5.94$. The results obtained for the energy density at $t = 10L$ can be seen in figure 4.2, where the differences $|f_{h_m} - f_{h_f}|$ have been amplified by $Q = 5.94$. The results show fourth-order convergence. We have further verified that the values obtained for our medium resolution run are within $\sim 0.4\%$ of the fourth-order Richardson-extrapolated ones, giving us an estimate of the error incurred in the simulation.

4.4 Results

Using the code detailed in section 4.2 one can simulate shock-wave collisions and explore the parameter space of theories, temperatures for the final plasma, and the projectile features. Unlike in the conformal case, in which the physics only depends on the dimensionless "thickness" $\mu\omega$ [55], in the present models the physics depends also on

the initial transverse energy density in units of the source, μ/Λ. We simulate collisions of $1/2$-shocks and $1/4$-shocks in the terminology of [55] ($\mu\omega = 0.30$ and $\mu\omega = 0.12$, respectively) for several different values of μ/Λ. We then extract the boundary stress tensor and we focus on its value at mid-rapidity, $z = 0$, as a function of time.[1] We choose $t = 0$ as the time at which the two shocks would have exactly overlapped in the absence of interactions [55].

We define the hydrodynamization time, t_{hyd}, as the time beyond which both pressures are correctly predicted by the constitutive relations of first-order viscous hydrodynamics,

$$P_L^{hyd} = P_{eq} + P_\eta + P_\zeta \,, \tag{4.62}$$

$$P_T^{hyd} = P_{eq} - \frac{1}{2}P_\eta + P_\zeta \,, \tag{4.63}$$

with a 10% accuracy, so that

$$\frac{\left| P_{L,T} - P_{L,T}^{hyd} \right|}{\bar{P}} < 0.1 \,. \tag{4.64}$$

In (4.62) we have denoted by P_η and P_ζ the shear and the bulk contributions to the hydrodynamic pressures, respectively, which are proportional to the corresponding viscosities. The different coefficients in front of P_η in these two equations reflect the tracelessness of the shear tensor. We define the EoSization time, t_{EoS}, as the time beyond which the average pressure coincides with the equilibrium pressure with a 10% accuracy, meaning that

$$\frac{\left| \bar{P} - P_{eq} \right|}{\bar{P}} < 0.1 \,. \tag{4.65}$$

We expect on physical grounds that increasing the initial energy in the shocks increases the energy deposited in, and hence the hydrodynamization temperature of, the resulting plasma. We have confirmed that, indeed, T_{hyd}/Λ increases monotonically with μ/Λ. On the gravity side this means that, for sufficiently large (small) μ/Λ, the horizon forms in the UV (IR) region of the solution, where the geometry is approximately AdS. As a consequence, in these two limits the plasma formation and subsequent relaxation proceed approximately as in a CFT. In contrast, for $\mu \sim \Lambda$ the relaxation of the plasma takes

---

[1] We employ as a regulator a background thermal bath with an energy density between 0.8% and 2.5% of that at the centre of the initial shocks. We simulate each collisions with several different regulators and extrapolate to zero regulator.

place in the most non-conformal region where the bulk viscosity effects are largest. In this intermediate region we see several effects that are absent in a CFT.

First, hydrodynamization times are longer than in a CFT. This is illustrated by the dashed, red curve in Fig. 4.3 (bottom) whose maximum, indicated by the first vertical line from the left, is 2.5 times larger than the conformal result, which is indicated by the horizontal line.[2] As expected, at high T_{hyd}/Λ we see that $t_{hyd}T_{hyd}$ asymptotically approaches its conformal value (we have checked that at $T_{hyd}/\Lambda = 4.8$ the difference is 0.5%). We expect the same to be true at low T_{hyd}/Λ.[3] The increase in the hydrodynamization time is qualitatively consistent with the increase in the lifetime of non-hydrodynamic quasi-normal modes found in [1, 37, 39, 83–86, 105]. A heuristic explanation on the gravity side comes from realizing that the larger the non-conformality, the steeper the scalar potential becomes. As the plasma expands and cools down, the horizon "rolls down the potential". It is therefore intuitive that steeper potentials make it harder for the non-hydrodynamic perturbations of the horizon to decay.

Second, the equation of state is not obeyed out of equilibrium. This is illustrated in Fig. 4.4 (bottom) for a collision of 1/4-shocks with $\mu/\Lambda = 0.94$, for which the hydrodynamization temperature is $T_{hyd}/\Lambda = 0.24$. We see that the equilibrium and the average pressures are not within 10% of one another until a time $t_{EoS} = 9.6/\Lambda = 2.4/T_{hyd}$. This is further illustrated in Fig. 4.3 (bottom), which shows the dependence of the EoSization time on the hydrodynamization temperature for 1/2-collisions. We see that for sufficiently large μ/Λ the EoSization time becomes negative, meaning that the average and the equilibrium pressures differ by less than 10% even before the shocks collide. The reason is simply that in these cases the energy density in the Gaussian tails in front of the shocks, which start to overlap at negative times, becomes much higher than Λ. At these energy densities the physics becomes approximately conformal and the equation of state becomes approximately valid as a consequence of this symmetry. An analogous argument implies that t_{EoS} should also become negative for collisions with sufficiently small μ/Λ.[3]

Third, hydrodynamization can take place before EoSization. Indeed, we see in Fig. 4.3 (bottom) that $t_{hyd} < t_{EoS}$ for collisions for which the hydrodynamization temperature is between the first and the fourth vertical line. Comparing with Fig. 4.3 (top) we see that at these two temperatures the viscosity-to-entropy ratios are $\zeta/s = 0.025$ and $\zeta/s = 0.017$,

---

[2]This value differs from that in [55] because [55] used a 20% criterion to define t_{hyd}.

[3]Although we have not been able to verify this explicitly because simulations in this regime become increasingly challenging, Fig. 4.3(bottom) is consistent with this expectation.
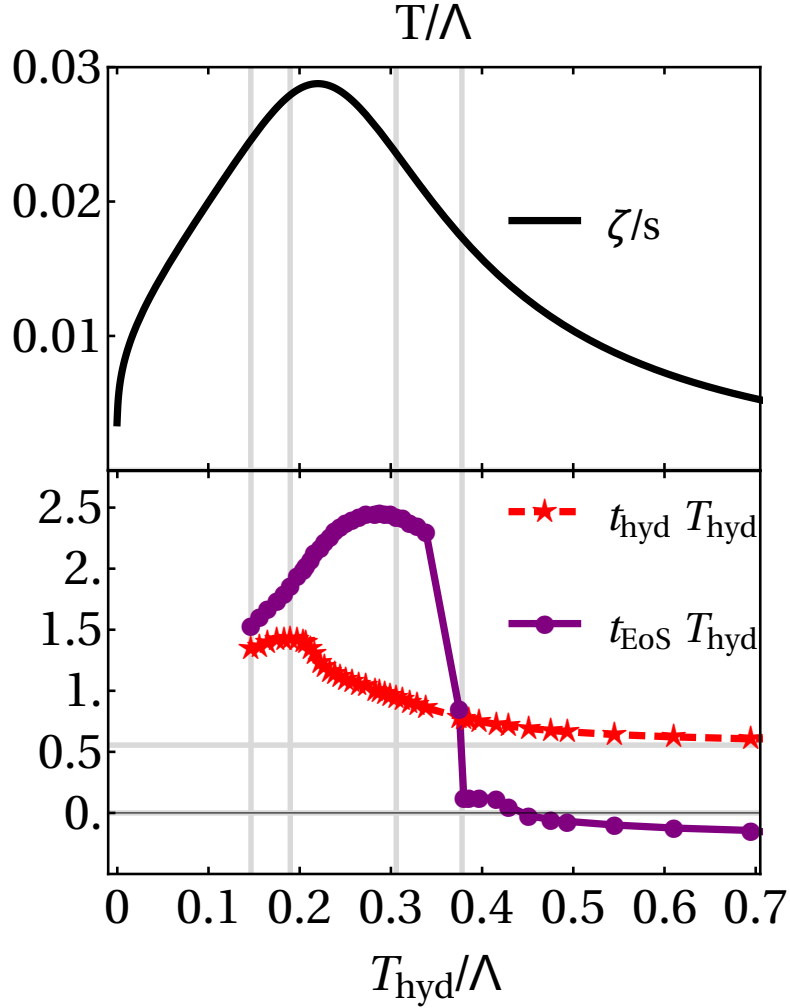
Figure 4.3: (Top panel) Bulk viscosity over entropy density as a function of temperature. (Bottom panel) Hydrodynamization and EoSization times as a function of the hydrodynamization temperature for collisions of $1/2$-shocks. The vertical grid lines lie at $T/\Lambda = \{0.15, 0.19, 0.31, 0.38\}$ and mark, respectively, the lowest value of T_{hyd}/Λ that we have simulated, the maximum of $t_{hyd}T_{hyd}$, the point with the largest ratio of t_{EoS}/t_{hyd}, and the intersection between the two curves. The bulk viscosity at these temperatures is $\zeta/s = \{0.025, 0.028, 0.023, 0.017\}$. The top horizontal line indicates the result in a CFT, $t_{hyd}T_{hyd} = 0.56$.[2]
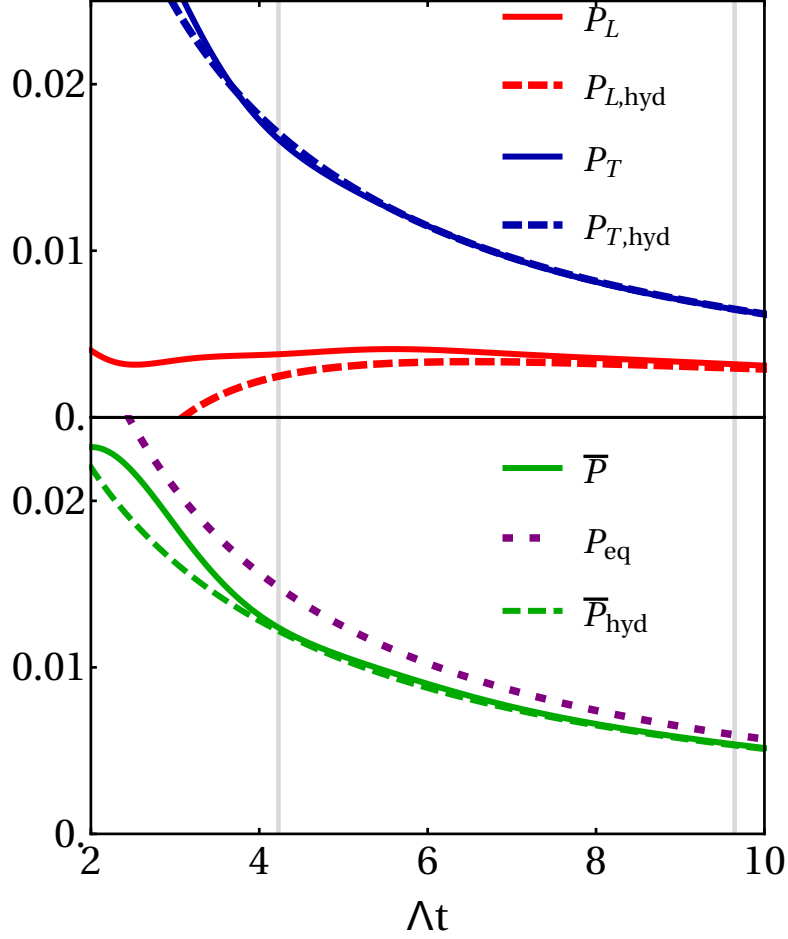
Figure 4.4: Longitudinal, transverse and average pressures, their hydrodynamic approxima-
tions, and the equilibrium pressure extracted from the equation of state, all in
units of Λ^4, for a collision of $1/4$-shocks with $\mu/\Lambda = 0.94$. The hydrodynamization
temperature is $T_{hyd}/\Lambda = 0.24$. Because the transverse pressure hydrodynamizes
much faster than the longitudinal one, P_T and P_T^{hyd} are virtually on top of one
another for the times shown. Hydrodynamization and EoSization take place at
$t_{hyd}\Lambda = 4.2$ and $t_{EoS}\Lambda = 9.6$, respectively, as indicated by the vertical lines. At
t_{hyd} the difference between $\bar{P}$ and   is 18%, whereas the difference between $\bar{P}$ and
$\bar{P}_{hyd}$ is 2%. At t_{EoS} the difference between P_L and P_L^{hyd} is 3%. The P_T/P_L ratio
is 4.4 at t_{hyd} and 1.9 at t_{EoS}.

respectively. Note that the first value of ζ/s would decrease if we were to consider the lower temperature at which we expect that the two curves in Fig. 4.3 (bottom) will have a second crossing. Also, note that the ordering of t_{hyd} and t_{EoS} depends on the accumulated effect of the bulk viscosity along the entire history of the collision. Notwithstanding these caveats, we will take the value $\zeta/s = 0.025$ as a conservative estimate of the minimum bulk viscosity needed to have $t_{hyd} < t_{EoS}$ for $1/2$-collisions. The maximum value of the ratio t_{EoS}/t_{hyd} for $1/2$-collisions is $t_{EoS}/t_{hyd} = 2.56$.

Regardless of the ordering of t_{EoS} and t_{hyd}, these times are always shorter than the isotropization time beyond which P_L and P_T differ from one another by less than 10%. This is apparent in Fig. 4.4.

4.5 Discussion

Eqs. hydro imply that the hydrodynamic viscous correction to the equilibrium pressure is controlled by the bulk viscosity alone, since

$$\bar{P}_{hyd} = P_{eq} + P_\zeta \,, \tag{4.66}$$

whereas the viscous deviation from isotropy is controlled by the shear viscosity alone, since

$$P_L^{hyd} - P_T^{hyd} = \tfrac{3}{2} P_\eta \,. \tag{4.67}$$

We see from bulk that the reason why hydrodynamization can take place before EoSization is because hydrodynamics becomes applicable at a time when bulk-viscosity corrections are still sizeable. This is illustrated in Fig. 4.4 by the fact that hydrodynamics provides an excellent prediction (within 2%) for $\bar{P}$ at t_{hyd}, whereas at this time $\bar{P}$ and P_{eq} still differ by 18%. The above statement is the analog of the fact that hydrodynamization can take place before isotropization because hydrodynamics becomes applicable at a time when shear-viscosity corrections are still sizeable [54]. In our model the bulk viscosity is rather small compared to the shear viscosity, since $\zeta/\eta = 4\pi\zeta/s \simeq 0.35$ at the temperature at which ζ attains its maximum value. Presumably this is the reason why the difference between P_L and P_T at t_{hyd} in Fig. 4.4 is much larger than that between $\bar{P}$ and P_{eq}.

Our results indicate that relaxation in non-conformal theories follows two qualitatively different paths depending on the bulk viscosity. If $\zeta/s \lesssim (\zeta/s)_{\text{cross}}$ then EoSization

precedes hydrodynamization, whereas for $\zeta/s \gtrsim (\zeta/s)_{\text{cross}}$ the order is reversed. Although we may take the cross-over value $(\zeta/s)_{\text{cross}\sim 0.025}$ obtained from $1/2$-collisions as representative, we emphasize that this depends not just on the model but on the specific flow under consideration. For example, we expect $(\zeta/s)_{\text{cross}}$ to take a smaller value for $1/4$-collisions since in this case the gradients are larger than for $1/2$-collisions [55]. Note that along either of these paths, correlation functions, such as two point functions, may still differ from their thermal values, as explicitly demonstrated in [106, 107].

Heavy ion collisions provide an excellent laboratory in which to study experimentally these two paths to relaxation. Indeed, although at very high temperatures the deconfined phase of QCD is approximately conformal, with very small values of ζ/s, estimates of this ratio indicate that, in the vicinity of the critical temperature, T_c, a fast rise takes place to values as large as $\zeta/s \simeq 0.3$ [108]. Despite the fact that ζ/s is only sizeable in a relatively narrow region around T_c, it has been shown to have an important effect on the late-time hydrodynamic description of the QGP created at RHIC and the LHC [73, 109–117]. Our results suggest that the value of ζ/s may also have an impact on the early-time process of hydrodynamization. This may be investigated by comparing collisions of different systems with varying energies. For most central collisions at top RHIC or LHC energies, the initial temperature is well above T_c and hydrodynamization proceeds as in a conformal theory. However, in peripheral collisions or in central collisions at lower energies, such as those at the RHIC energy scan, the hydrodynamization temperature is reduced and the corresponding bulk viscosity may be sufficiently large to delay EoSization until after hydrodynamization. Another exciting possibility is to consider collisions of smaller systems, such as $p - Pb$, $d - Au$, ${}^3He - Au$ or $p - p$ collisions. As it has been recently discovered, these systems also show strong collective behaviour [118–122, 122, 123] that is well described by hydrodynamic simulations [74–76, 124–128] that include non-zero values of the bulk viscosity (see [129] for a review of collective effects in this type of collisions). As stressed in [126], the temperature range explored by these smaller systems is narrowly concentrated around T_c. These makes them ideal candidates with which to explore the effect of transport coefficients, in particular of the bulk viscosity. The comparison between the early-time dynamics of these small systems and heavy ion collision is an excellent framework in which to explore the different relaxation paths uncovered here.

Chapter 5

Phase transitions and instabilities

5.1 Background

5.1.1 Transitions and critical point

When considering physics at zero baryonic density, the phase structure of QCD is limited to a confining region and an asymptotic free plasma separated by a rapid cross-over (with the first evidence of it coming from the lattice [130]). However, upon adding the baryonic chemical potential (μ_b) into the phase diagram, the diversity of phases and transitions accessible increases dramatically (see [131, 132] for recent reviews on the topic). Although the nature of the phase diagram is only conjectured for most of its parameter space, there are some regions in where calculations are possible. For instance, lattice QCD and chiral effective theories can give information of the nature of the transitions at the axes of the phase diagram; thanks to them we know there is a cross-over in the T axis, and a first order phase transition on the μ_b one (see fig. 5.1). The presence of this two kinds of transition motivates the existence of a critical point at a high T but also high μ_b. Unfortunately, the existing heavy ion colliders have long been unable to access high enough densities necessary to observe the critical point and its exotic properties. It is because of this, that the construction – or reconditioning – of synchrotrons able to achieve such densities started already some years ago, and the first preliminary results have been given by RHIC [133].

Due to the strong interactions and the large chemical potential, the traditional techniques used for QCD calculations find insurmountable difficulties around the critical point. Once again, the gauge/gravity correspondence can provide computational tools
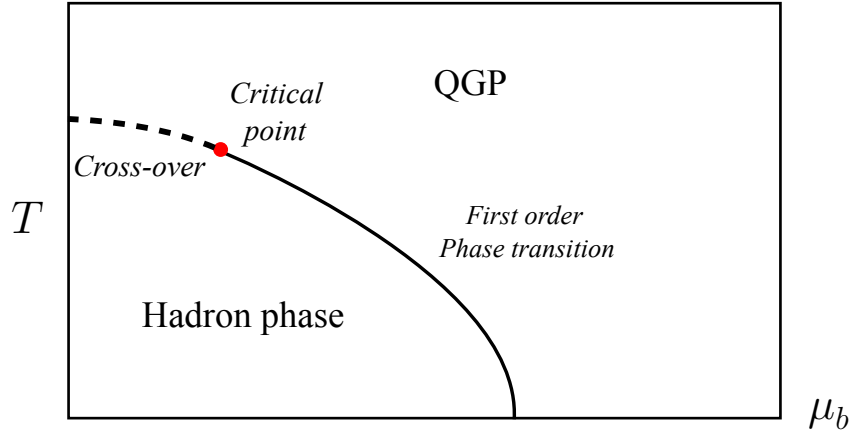
Figure 5.1: Schematic QCD phase diagram for the lower baryonic density region.

at regimes other approaches fail. It is important to keep in mind that holography does offer toy models that are not QCD, and that these are only probed at very large coupling. Following the bottom-up approach, holography has already been used to provide gravitational duals to gauge theories with a critical point [134, 135]. The recreation of a critical point requires both a non-trivial RG flow and the presence of a conserved current, which can be achieved by combining models such as the ones presented in chapters 2 and 3. One of the ultimate goals of this program would be to provide realistic shock-wave collisions close to the critical point, and make contact with the future experiments. Nevertheless, a previous step necessary to understand the effects of transitions in the dynamics will be using simpler models with no conserved currents, but showing phase transitions.

In this chapter we will show that the model presented in chapter 3 can indeed contain first and second order phase transitions, added to the cross-over already described. To observe such transitions one needs to consider imaginary values for the parameter present in the potential, ϕ_M. In addition, we will explore the spinoidal instabilities present in these models, which can be seen in the gravity side of the duality as Gregory-Laflamme instabilities. Finally, and perhaps is the most surprising result, we will show that the final end-point of these instabilities are inhomogeneous states well described with second order hydrodynamics.

5.1.2 Hydrodynamics

Hydrodynamics is one of the most successful theories in physics, capable of describing the dynamics of very different systems over an enormous range of length scales. Traditionally, it is thought of as an effective theory for the conserved charges of a system, constructed as a derivative expansion around local thermal equilibrium. From this perspective hydrodynamics is only expected to be valid when these gradient corrections are small compared to all the microscopic scales. However, in recent years it has been discovered that the regime of validity is actually much broader.

From an experimental viewpoint, hydrodynamics has been extremely successful at describing the post-collision dynamics of the drops of matter produced in ultra-relativistic collisions of large nuclei at RHIC[136–138] and the LHC[139–141, 141]. Although the size of these drops is just a few times larger than the relevant microscopic scale, multi-particle correlations in these collisions are well described by hydrodynamics [11, 12, 142–146], provided one assumes that the latter is valid in the presence of large gradients [147]. Also, the recent finding of similar correlations in even smaller proton-proton collisions [123, 148, 149] provides a strong indication that hydrodynamics is applicable even at a baryonic scale [74, 75, 125, 150]. From a theoretical viewpoint, studies of non-abelian gauge theories have shown that hydrodynamics is valid for systems with large gradients both at strong [2, 54, 55, 78, 102] and weak coupling [20, 151].

In this chapter we use the gauge/string duality to test the validity of hydrodynamics in a theory with a first-order thermal phase transition. We place the theory on a cylinder in a variety of homogeneous, unstable initial states. We use the gravity description to follow their evolution until they settle down to some static, inhomogeneous final state. We then compare the time evolution and the final configurations to the hydrodynamic prediction. Recent related work includes [36, 82, 152].

The formalism and numeric code used for the evolution in this chapter are the exact same as the ones used in chapter 4.
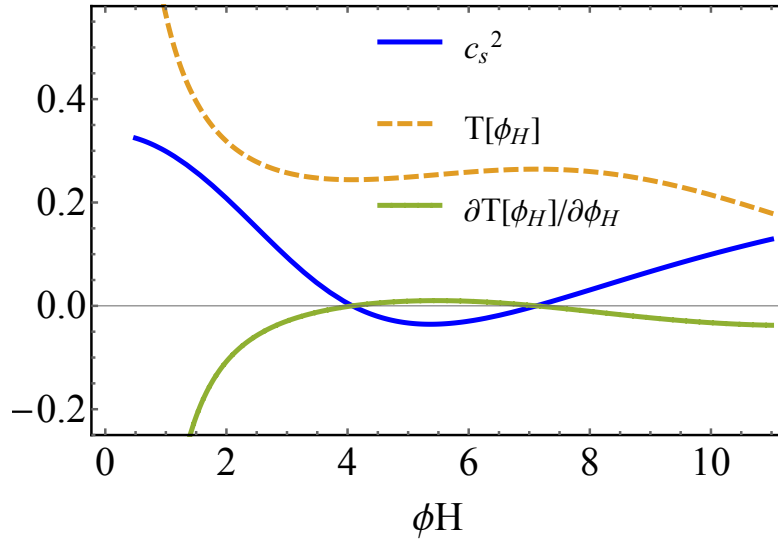
Figure 5.2: Example of multivaluation for the T function in terms of the scalar ϕ_H for the model $\phi_M = 2.3i$. Also depicting the speed of sound.

5.2 A twist to the non-conformal model

5.2.1 Extension of the parameter space

We begin by recalling the one-parameter family of potentials used in the two previous chapters,

$$L^2 V = -3 - \frac{3}{2}\phi^2 - \frac{1}{3}\phi^4 + \frac{1}{3\phi_M^2}\phi^6 + \frac{1}{2\phi_M^4}\phi^6 - \frac{1}{12\phi_M^4}\phi^8 . \tag{5.1}$$

with L the asymptotic curvature radius, and now ϕ_M taking purely imaginary values (note that it only appears in even powers). This is exactly the potential of chapter 3 and 4 except for the effective sign reversal of the fourth term in V. This difference has dramatic implications for the thermodynamics of the gauge theory, which we extract from the homogeneous black brane solutions of the gravity model using the same method as in chapter 3. In particular, the gauge theory can now possess a phase transition, as signalled by the multiplicity of black brane solutions with a particular temperature (see fig. 5.2, where the temperature is depicted in function of the black brane labelling variable ϕ_H).   The thermodynamics of imaginary ϕ_M models connects smoothly with the ones of the models explored in chapter 3. In fact, the parameter that manifests this continuity in the model family is $1/\phi_M^2$ rather than ϕ_M. The models with very large ϕ_M smoothly connect with the ones with imaginary ϕ_M and very large $|\phi_M|$. Taking $1/\phi_M^2$
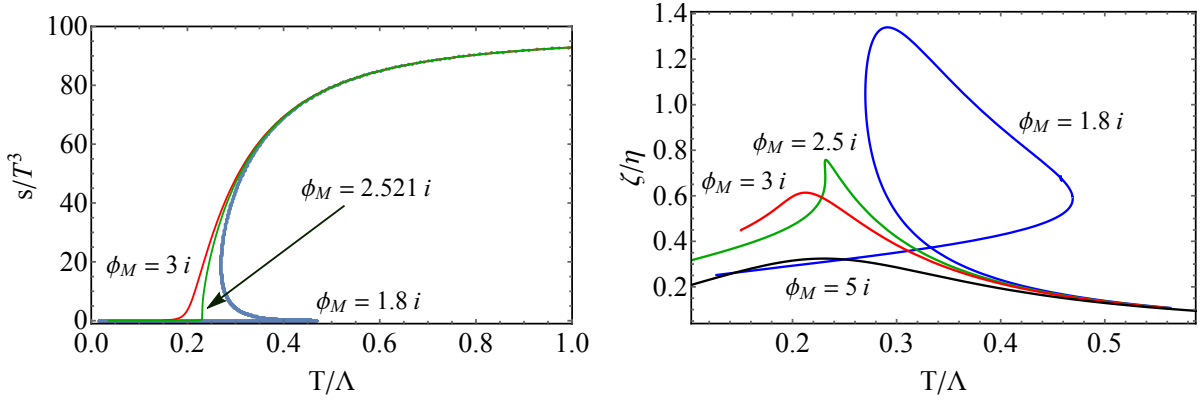
Figure 5.3: Left panel: S/T^3 in terms of the temperature. For models with $Im[\phi_M] < 2.512$ the system encounters a phase transition instead of a cross-over. Right panel: bulk viscosity over shear viscosity, a proxy for the non-conformality of the system. The maximum of this function increases with $Im[\phi_M]$

increasingly negative increases the steepness of the cross-over and the non-conformality effects until the models encounter a (second order) phase transition at $\phi_M = 2.521i$ (see fig 5.3). For models with $Im[\phi_M] < 2.512$, the phase transition is first order.

5.2.2 The $\phi_M = 2.3i$ case

In this chapter we will focus on the model given by $\phi_M = 2.3i$, a model with a first order phase transition in where the different phases are not separated by many orders of magnitude. The phase structure of this model is concisely captured in fig. 5.4. States on the dashed red curve are locally thermodynamically unstable since the specific heat is negative, $c_v = d\mathcal{E}/dT < 0$. In this region the speed of sound, $c_s^2 = s/c_v$, becomes imaginary. The global stability of the states is given by the free energy; the states with lowest F are the ultimately stable ones (see fig. 5.5). The existence of a locally unstable range of energies leads to a dynamical, spinodal instability (see e.g. [153]) whereby the amplitude of small sound excitations grows exponentially with a momentum-dependent growth rate dictated by the sound dispersion relation:

$$\Gamma(k) \simeq |c_s| \, k - \frac{1}{2T} \left(\frac{4}{3} \frac{\eta}{s} + \frac{\zeta}{s} \right) k^2 , \tag{5.2}$$

where η and ζ are the shear and bulk viscosities. In our model $\eta/s = 1/4\pi$ [16] and we compute ζ numerically following [95].
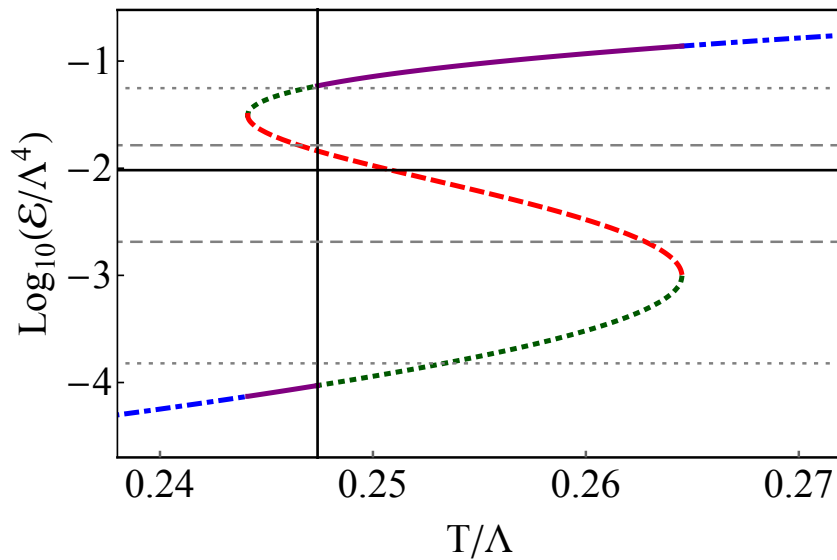
Figure 5.4: Energy density versus temperature for the gauge theory dual to (4.1). At high and low T there is only one phase shown in dashed-dotted blue. The preferred phase in the multivalued region is shown in solid purple. The dotted green curve is metastable. The dashed red curve is locally unstable. The black vertical line indicates $T_c = 0.247\Lambda$. The top (bottom) dashed, grey horizontal line indicates the highest (lowest) average energy density that we have considered. The top (bottom) dotted, grey horizontal line indicates the maximum (minimum) value of the energy in the corresponding final states. The solid, black horizontal line is the state for which we show specific results.
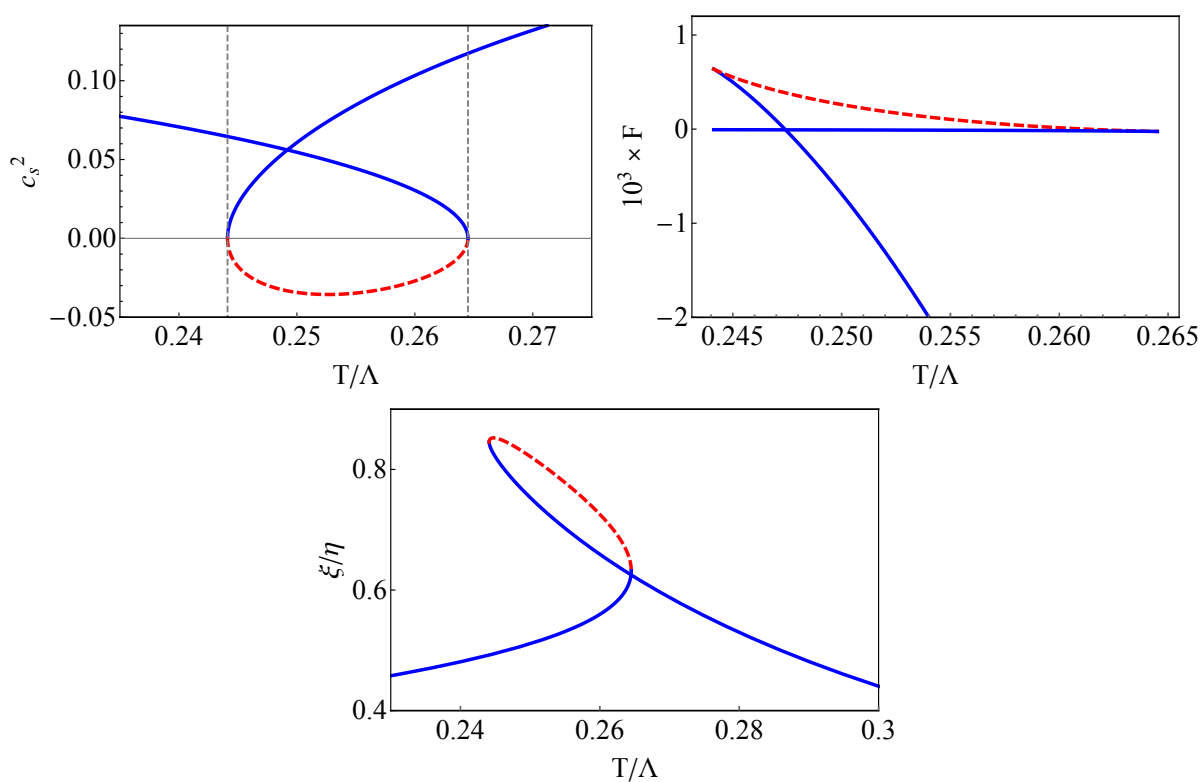
Figure 5.5: Top left panel: speed of sound in terms of T. The negative values of c_s^2 signal the presense of an instability in the range of temperatures for $\phi_M = 2.3i$. Top right panel: free energy in terms of T for the same model. In red dashed it is depicted the locally unstable branch in both plots. Bottom panel: bulk viscosity, proxy for non-conformality.

5.3 Inhomogeneous horizon

To investigate the fate of the spinodal instability we compactify the gauge theory direction z on a circle of length $L \simeq 57/\Lambda$. This infrared cut-off reduces the number of unstable sound modes to a finite number. We then consider a set of homogeneous, unstable initial states with energy densities in the range $\mathcal{E}/\Lambda^4 \simeq (0.002, 0.016)$, as indicated by the grey, dashed horizontal lines in Fig. 5.4. For concreteness we will show results for the state with $\mathcal{E}/\Lambda^4 \simeq 0.0096$, whose temperature and entropy density are $T_i \simeq 0.251\Lambda$ and $s_i = 0.037\Lambda^3$. To trigger the instability, we introduce a small z-dependent perturbation in the energy density corresponding to a specific Fourier mode on the circle. For concreteness we will show results for the case with $k = 3(2\pi/L) \simeq 1.3 T_i$. This mode is unstable with positive growth rate $\Gamma = 0.0247\,\Lambda$ according to (5.2). For numerical simplicity we impose homogeneity along the transverse directions.

On the gravity side the sound-mode instability may be viewed [154–156] as a Gregory-Laflamme instability [157]. To initiate the evolution we choose to introduce, on top of a thermal homogeneous solution, a sinusoidal perturbation in the a_4 coefficient of amplitude 10^{-4} times the equilibrium value. We follow it by numerically evolving the Einstein-plus-scalar equations – using the same code as in chapter 4 – until the system settles down to a state with an inhomogeneous Killing horizon with constant temperature $T_f = 0.250\Lambda$. Note that this is close but not identical to T_i or T_c.   From the dynamical
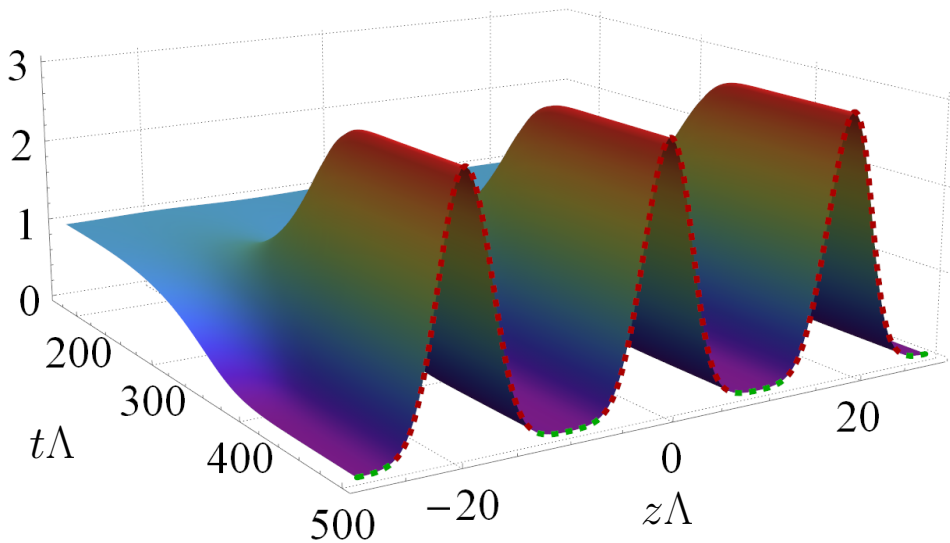

Figure 5.6:   Energy density in units of $\Lambda^4/10^{-2}$ for the initial state indicated by the solid, black horizontal line in Fig. 5.4, perturbed by the third Fourier mode. The color coding on the final-time slice is the same as in Fig. 5.4.
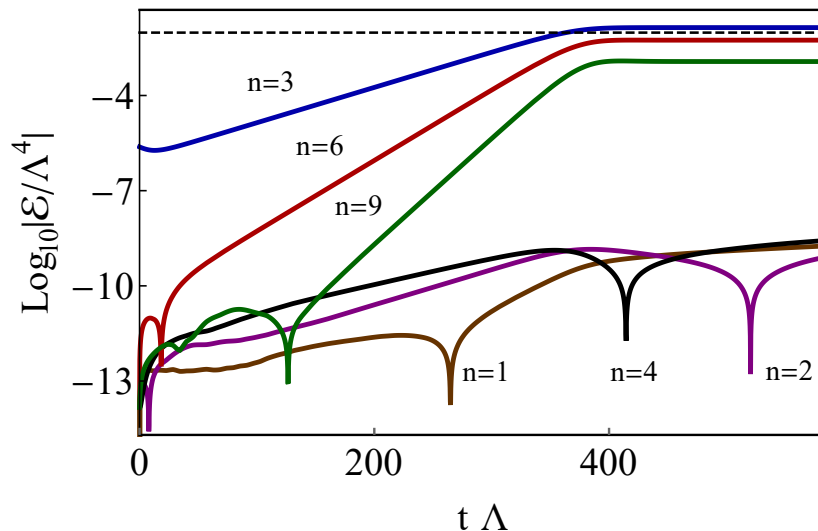
Figure 5.7: Time evolution of some Fourier modes of the energy density $\mathcal{E}$. The dashed horizontal line is the average energy density.

metric we extract the boundary stress tensor. The result for the energy density is shown in Fig. 5.6. The time dependence of the amplitudes of several modes of the energy density is shown in Fig. 5.7. The $n = 3$ mode grows with a rate that agrees with (5.2) within 4%. Resonant behavior makes the modes with $n = 6, 9, \ldots$ grow at a rate that is roughly the corresponding multiple of the $n = 3$ rate. Numerical noise makes some non-multiples of the $n = 3$ mode (of which only three are shown in the figure) grow too. At late times the non-linear dynamics stops the growth of all these modes and the system settles down to a static, inhomogeneous configuration consisting of three identical domains. The fact that their size is comparable to the inverse temperature, $\Delta z = L/3 \simeq 0.4/T_f$, is our first indication that spatial gradients are large.

In Fig. 5.8 we show the final entropy density as extracted from the area of the horizon. The fact that s is not constant proves that the horizon itself (not just the boundary energy density) is inhomogeneous. We see in the figure that s is very well estimated by a point-wise application of the equation of state to the final energy density of Fig. 5.6, suggesting that the evolution is quasi-adiabatic. This is confirmed by the fact the final average entropy density is only 1% larger than the initial one.
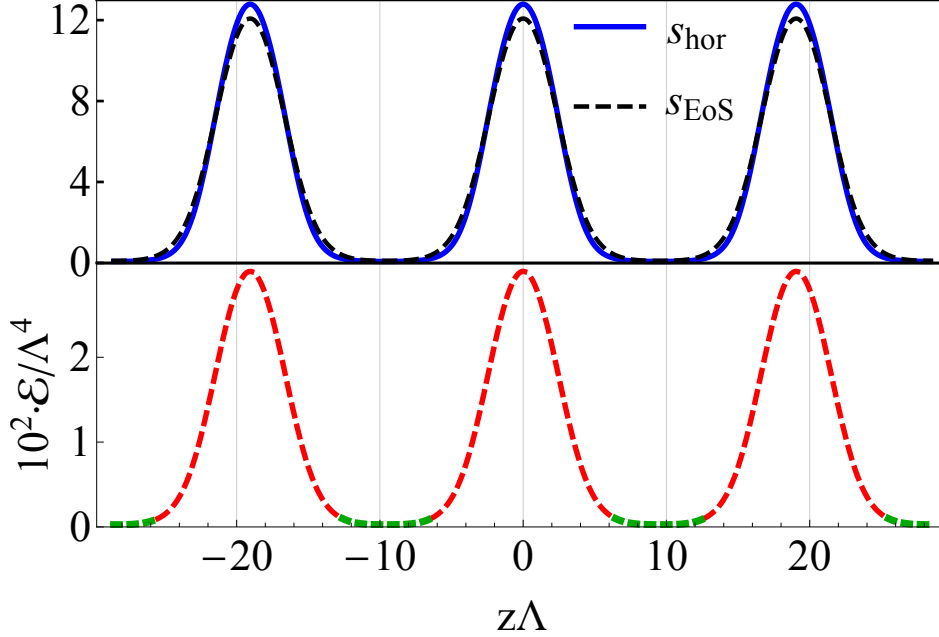
Figure 5.8: Top: final entropy density extracted from the area of the horizon (continuous, blue curve) and estimated from the equation of state (dashed, black curve), in units of $\Lambda^3/100$. Bottom: energy profile of the final state.

5.4 Hydrostatic final sate

Previous holographic studies have established that hydrodynamics can describe the evolution of the stress tensor in the presence of large gradients. Here we investigate whether it can also describe the static inhomogeneous configuration at the endpoint of the spinodal instability.

In the hydrodynamic approximation the stress tensor is expanded in spatial gradients in the local fluid rest frame. Up to second order, the constitutive relations are

$$T_{\mu\nu}^{\text{hyd}} = T_{\mu\nu}^{\text{ideal}} - \eta\,\sigma_{\mu\nu} - \zeta\,\Pi\,\Delta_{\mu\nu} + \Pi_{\mu\nu}^{(2)} \tag{5.3}$$

where, in the fluid rest frame, $T_{\mu\nu}^{\text{ideal}} = \text{Diag}\{\mathcal{E}, P_{\text{eq}}(\mathcal{E})\}$, $P_{\text{eq}}(\mathcal{E})$ is the equilibrium pressure of the homogeneous states shown in Fig. 5.4, $\sigma_{\mu\nu}$ and Π are the sheer and bulk stresses, and $\Delta_{\mu\nu}$ is the projector onto the spatial directions. The tensor $\Pi_{\mu\nu}^{(2)}$ contains all the second-order terms. In a non-conformal theory this tensor contains thirteen $\mathcal{E}$-dependent second-order transport coefficients and its explicit expression may be found in [158]. A subset of these coefficients for the model of [1] has been computed in [159].

In a static configuration the fluid three-velocity field is identically zero, the stress tensor is diagonal, both $\sigma_{\mu\nu}$ and Π vanish, and the leading gradient corrections are those in $\Pi_{\mu\nu}^{(2)}$. This tensor also simplifies since only two independent second-order terms survive in this limit. In the Landau frame, the constitutive relations reduce to

$$
\begin{aligned}
P_L^{\mathrm{hyd}} &= P_{\mathrm{eq}}(\mathcal{E}) + c_{\mathrm{L}}(\mathcal{E})(\partial_z \mathcal{E})^2 + f_{\mathrm{L}}(\mathcal{E})(\partial_z^2 \mathcal{E}) \,, & (5.4) \\
P_T^{\mathrm{hyd}} &= P_{\mathrm{eq}}(\mathcal{E}) + c_{\mathrm{T}}(\mathcal{E})(\partial_z \mathcal{E})^2 + f_{\mathrm{T}}(\mathcal{E})(\partial_z^2 \mathcal{E}) \,. & (5.5)
\end{aligned}
$$

The statement that hydrodynamics describes the final states is the statement that the corresponding pressures are given by these equations with second-order transport coefficients $c_{\mathrm{L,T}}(\mathcal{E})$ and $f_{\mathrm{L,T}}(\mathcal{E})$ that depend on the local energy density but *not* on any other details of the final states. We have verified this state independence by varying both the average energy densities within the range shown in Fig. 5.4 and the length of the circle L.

Equivalently, a hydrodynamic description of the final states means that, once $c_{\mathrm{L,T}}(\mathcal{E})$ and $f_{\mathrm{L,T}}(\mathcal{E})$ have been extracted from a given state (or computed microscopically), they can be used to predict the pressures of a different state given its energy density profile. This is illustrated in Fig. 5.9, where we compare the true pressures obtained from the gravity side for the end state of Fig. 5.6 with the hydrodynamic predictions (5.4) and (5.5) based on coefficients extracted from a different state. It is remarkable that hydrodynamics works despite the fact that the second-order terms in these equations are as large as the equilibrium pressure, as can be seen in the figure from the difference between the continuous gray curve and the true pressures. This is particularly dramatic for the longitudinal pressure, P_L, which must be z-independent since, in a static state, conservation of the stress tensor reduces to $\partial_z T^{zz} = 0$. While the equilibrium contribution to P_L inherits z dependence from the energy density, this modulation is precisely compensated by the second-order contribution. We conclude that the second-order gradients sustain the inhomogeneous state.

Taking the applicability of hydrodynamics one step further, we can use it to predict all other static, inhomogeneous configurations. Time independence implies that P_L must be constant, which in the hydrodynamic approximation reduces to a second-order, non-linear differential equation for $\mathcal{E}(z)$ via (5.4). This depends on two integration constants that
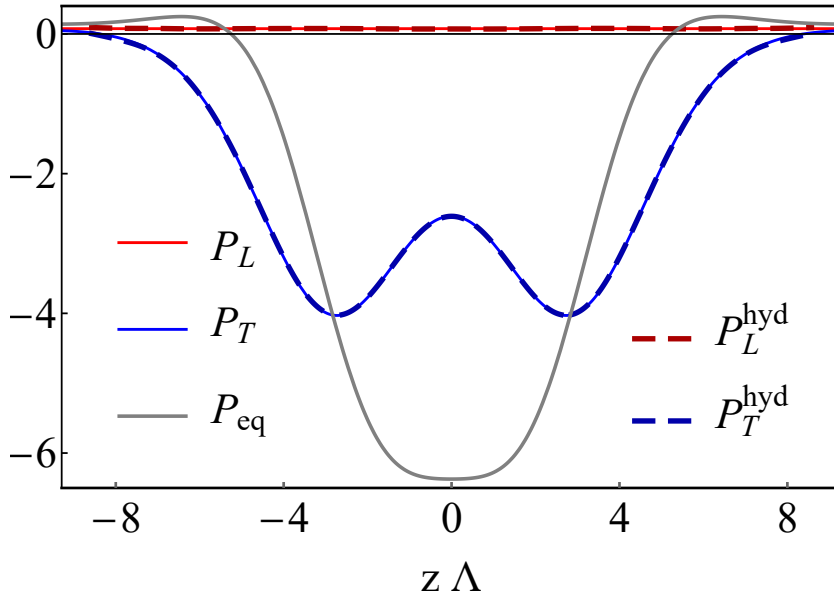
Figure 5.9: Pressures of the end state of Fig. 5.6, in units of $\Lambda^4/10^4$. The true pressures deviate significantly from the P_{eq} but are in excellent agreement with the hydrodynamic predictions (5.4)-(5.5).

can be traded for the length of the circle (more precisely, the size of the domains) and the average energy density. Once $\mathcal{E}(z)$ is known P_T is predicted by (5.5).

5.5 Hydrodynamic evolution

The second-order coefficients that we have extracted also control the dynamical evolution of the instability. However, unlike in the static final configuration, during the dynamical evolution there are non-zero momentum fluxes, leading to a small but non-vanishing three-velocity field. To approximate the full time evolution by hydrodynamics it is thus necessary to include the first-order shear and bulk tensor contributions in (5.3). Similarly, while the systems evolves there are additional second-order gradients beyond those considered in Eqs. (5.4) and (5.5). However, these additional second-order terms are quadratic in the velocity field and can be consistently neglected.

In Fig. 5.10 we show the time evolution of the pressures at $z\Lambda = 0$. The very early time behavior is the exponential decay of the quasi-normal modes (QNM) that are excited by the perturbation that we introduce to trigger the instability. After this short time, the predictions of second-order hydrodynamics match the true pressures. Second-order terms become increasingly important as the instability saturates, where

the first-order approximation, let alone the equilibrium pressure, fails to predict the true pressures while the second-order approximation continues to do so accurately. We conclude that hydrodynamics with large second-order gradients describes the evolution and the saturation of the spinodal instability.
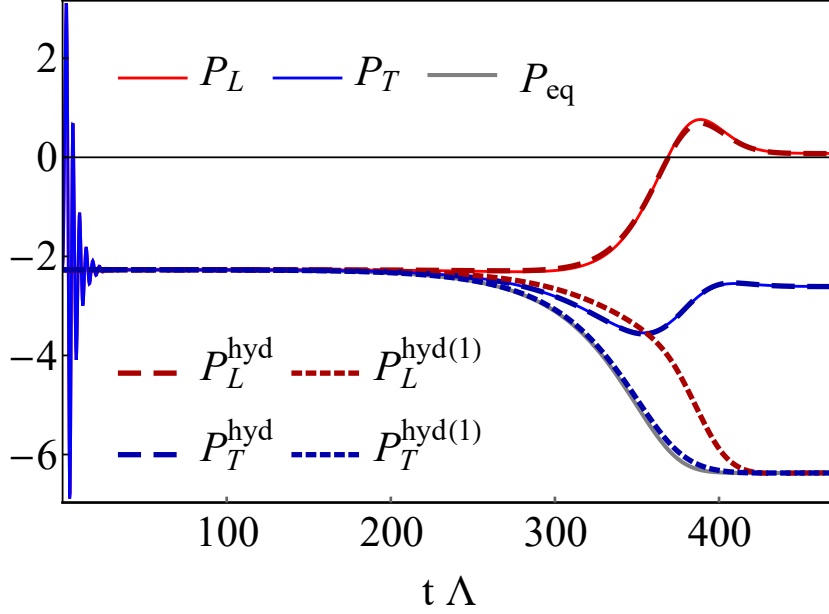

Figure 5.10: Time evolution of the pressures at $\Lambda z = 0$, in units of $\Lambda^4/10^4$. $P^{\mathrm{hyd}(1)}$ denotes the hydrodynamic pressure with only first-order terms included, whereas P^{hyd} includes these plus the second-order terms of Eqs. (5.4) and (5.5).

5.6 Discussion

We have uncovered a new example of the applicability of hydrodynamics to systems with large gradients. As in other known examples, part of the reason behind this success is the relaxation of the non-hydrodynamic QNMs at the relevant time scales of the evolution, as in the early transient behaviour observed in Fig. 5.10. The analysis of the exponential decay of these modes reveals that this process occurs over a time $\Gamma_{\mathrm{QNM}} \sim c\,\pi T$ with $c \simeq 3.4$, consistent with [39]. In contrast, for the unstable hydrodynamic mode, assuming $\zeta/\eta \sim 1$ and $\eta/s = 1/4\pi$, (5.2) yields the typical growth rate $\Gamma \sim |c_s|^2\,\pi T$, which in our case is suppressed with respect to Γ_{QNM} by the small value of $|c_s| \simeq 0.03$. Although this argument may explain why hydrodynamics provides a good description at intermediate times, once the QNMs have decayed, it remains surprising that it also describes the late-time evolution and the final state, where the spatial gradients are large. Moreover,

it suggests that it would be interesting to explore other values of the parameter ϕ_M for which the first-order transition becomes stronger and $|c_s|$ can become of order unity.

Our static inhomogeneous configurations do not describe the separation of the system into two stable phases. For example, the maxima of the end state of Fig. 5.6 do not lie in the green stable branch but in the red unstable branch of Fig. 5.4. Presumably, the reason is that, if the available average energy density is small, the cost of the necessary gradients for the peaks to reach the green stable branch makes the corresponding configuration disfavored. Similar considerations seem to be responsible for the fact that the final state of Fig. 5.6 exhibits three identical domains. More generally, our studies indicate that the number of domains in the final state is correlated with, but not exclusively determined by, the Fourier mode that is used to trigger the initial instability. In particular, entropy considerations may play a role, since final states on circles of equal length with the same average energy density but different number of domains have different entropies. It would be interesting to perform an exhaustive analysis to determine all the possible static, inhomogeneous states of the system by means of the gravitational and/or the hydrostatic descriptions.

Chapter 6

Summary and conclusions

The gauge/gravity duality has proven to be a very useful tool in the understanding of quantum field theories outside the perturbative regime. In particular, holography has been able to shed light not only on generic mechanisms of strongly coupled theories, but also on processes potentially occurring in experimental set-ups, such as the heavy ion collisions. Experimental observations as small viscosities or fast hydrodynamization find a natural explanation when the problem is expressed in terms of gravity and black holes. Despite the successes, however, it is important to bear in mind that holography provides computational tools for toy models rather than for QCD itself, and that these models are usable only under certain assumptions. Nature is very often far more nuanced than the models physicists use to describe it. In the case of heavy ion experiments and QCD there are many features that are commonly coarse grained in the holographic computations. For instance, non-trivial RG flows or baryon currents have not been included in the holographic models until very recently, although these are very relevant to experiments, and fundamental in critical phenomena.

In this thesis we present a series of works on the topics field theory and heavy ion collisions that use applied holography and numeric GR as computational tools. The unifying factor among them is that they consider gravitational set-ups beyond pure gravity to describe the physics of conserved currents, non-trivial RG flows and phase transitions.

- In chapter 2 we use an Einstein-Maxwell set-up to compute the collision of two shock-waves with a conserved current and the hydrodynamization of the subsequent plasma. This conserved current is used to model the baryonic charge deposition by rapidity, observed in the experiments. The simulations are done with and without

including the backreaction of the Maxwell field into the metric, which corresponds to the quenched approximation for the effects of the baryon charge on the gluons.

The results for the rapidity profiles of the charge deposition show that there is a strong dependence on the features of the initial projectiles, as it was already seen previously for the energy profiles in [55]. The distributions of the charge follow closely the ones for the energy, which implies a significant stopping of the baryon fraction in this holographic collisions. The outcome from the simulations agrees qualitatively with the experiments trend for low and moderate energy collisions, but seems to fail to recover the data of high energy experiments. The mismatch might be explained by the simplicity of the set-up used, with no fine structure in the projectiles, or the very large coupling assumption, which for the very initial states might not be correct. Regarding the effects of backreacting the charge into the metric, the results show that they are small and linear in the value of the coupling constant

- In chapter 3 we present a one parameter family of holographic non-conformal models. By adding a scalar field with a polynomial potential to the pure gravity set-up we can achieve a non-trivial RG flow between two fixed points in the dual field theory. In this work we compute the thermodynamics and the quasi-normal modes spectra for the homogeneous states, being the latter of the main results of the chapter.

  The inclusion of the scalar field in the gravitational set-up adds an extra channel by which the system can thermalize back to equilibrium. The other main result presented in this chapter is the changing in the preferred channel of equilibration depending on the temperature. The reason for this is the switch in the ordering of the imaginary part of the lowest quasi-normal modes with the temperature. At very high temperatures, the equilibration process is dominated by the "bulk" mode, consisting of fluctuations of the operator dual to the scalar field. Conversely, at low temperatures the last mode to thermalize is the pressure anisotropy mode.

- In chapter 4 we present the first holographic shock-wave collisions in a non-conformal model. To do so, we use the model introduced in chapter 3. In non-conformal models the average pressure in equilibrium is not fixed by symmetry, but by the equation of state. Out of equilibrium the average pressure might take any value, giving a new probe for the equilibration of the system. When the plasma's average pressure is well approximated by the equation of state value, we say that the system has "EoSized".

The main result of this work is the realization that the hydrodynamization might happen before the system has EoSized. This means that the system's stress-energy tensor is well described by hydrodynamics well before the average pressure is by the equation of state. This result is even more remarkable when noticing that the equation of state is an ingredient of the hydrodynamic constitutive expression.

- Finally, in chapter 5 we explore a holographic model that can contain phase transitions. This model is the same as the one presented in chapter 3, but now taking pure imaginary numbers for the controlling parameter.

In an effort to understand the instabilities present in models with phase transitions, we trigger and evolve a spinoidal instability to its inhomogeneous end state. This is done by adding a small perturbation to a uniform black brane in the locally unstable branch, triggering a Gregory-Laflamme type instability in the gravity side. The most remarkable result found in the simulation is that both the evolution and the final result are well described by second order hydrodynamics.

Capítol 7

Resum en Català

7.1 Què ens ha dut fins aquí

La teoria quàntica de camps (QFT n'és l'acrònim en anglès) és a la vegada un gran èxit i un problema obert de la física contemporània. Gràcies a ella, s'han pogut entendre l'estructura i interaccions que regeixen el món subatòmic, i d'aquesta manera predir amb precisió un gran nombre de fenòmens fonamentals. Malauradament, però, el control que tenim sobre les QFTs es restringeix genèricament al règim en el qual hom pot utilitzar expansions pertorbatives. Fora d'aquest règim hi trobem multitud de casos pels que no se'n té una comprensió completa, com son el sistemes fortament interactuants. En aquesta categoria s'hi troben els nuclis atòmics, els superconductors, els super-fluids i el plasma de quarks i gluons (QGP), sistemes per als quals només en tenim un enteniment limitat a situacions en equilibri, o amb un alt grau de simetria. Per tal de poder comprendre aquests sistemes, així com també per assolir una comprensió vertadera de les teories quàntiques de camps, seran necessaris noves tècniques i formalismes.

Un cas paradigmàtic de teoria quàntica de camps amb fases fortament acoblades és la cromodinàmica quàntica (QCD), la teoria que descriu la força nuclear forta. Amb l'objectiu d'entendre en profunditat la QCD i la seva dinàmica, és va iniciar a la dècada de 1970 el programa de col·lisions de ions pesants. Aquest programa experimental té com a objectiu crear, mitjançant acceleradors de partícules, fases de QCD de-confinades i estudiar-ne les seves propietats. Paral·lelament als experiments, s'han anat desenvolupant marcs teòrics per poder explicar els resultats experimentals com son QCD al "lattice", la hidrodinàmica o l'holografia. Malgrat tot, encara s'està molt lluny d'obtenir una explicació completa de la dinàmica fora de l'equilibri observada en les col·lisions.

Entre els nous formalismes utilitzats per a descriure sistemes fortament acoblats, com les col·lisions d'ions pesants, hi ha la dualitat "gauge/string" , que fou descoberta l'any 1997 i és coneguda popularment com a holografia. La dualitat "gauge/string" és una correspondència entre dues teories – una teoria gauge i una teoria de cordes – que permet fer càlculs en una de les dues teories per mitjà de la seva dual. Tot i el gran potencial de l'holografia, és important no oblidar que no es coneix el dual gravitatori de QCD i que un s'ha de conformar en fer fer càlculs per a teories similars a aquesta. La correspondència es pot fer servir per relacionar un plasma fortament acoblat i el seu dual, forats negres en un espai asimptòticament anti-de-Sitter (AdS), on els càlculs resulten factibles. Així, per simular la col·lisió d'ions pesants s'evoluciona numèricament la col·lisió d'ones gravitatòries en AdS, i la subseqüent relaxació del seu horitzó d'esdeveniments.

7.2 Contingut de la tesi

En aquesta tesi s'hi presenten un seguit de treballs emmarcats en el camp de l'holografia aplicada, on s'hi considera dinàmica en models més enllà de gravetat pura.

7.2.1 Col·lisions amb càrrega bariònica

Per facilitar els càlculs que comporta l'evolució numèrica, en la majoria dels casos es treballa amb el model hologràfic més simple possible: gravetat pura. Aquesta elecció comporta, però, limitacions importants. L'únic observable accessible en una col·lisió en gravetat pura és el tensor energia-moment. La física de corrents conservats, com el corrent bariònic, queda fora de l'abast d'aquestes simulacions.

En el capítol 2 s'hi mostra la primera simulació de col·lisions fent servir l'acció d'Einstein-Maxwell per al dual gravitatori. Això ens permet estudiar la dinàmica d'un corrent conservat i modelar el comportament de la càrrega bariònica en les col·lisions d'ions reals, observable en els experiments.

7.2.2 Estudi prop de l'equilibri per a models no conformes

La teoria gauge dual a gravetat pura no és QCD sinó $\mathcal{N} = 4$ Super Yang-Mills, una teoria conforme que té similituds importants amb QCD i que s'utilitza com a "toy model"

d'aquesta. Tanmateix, el poder predictiu d'aquest model està limitat a molt altes energies, on QCD és quasi conforme. A temperatures més baixes QCD mostra el seu caràcter no conforme en fenòmens com els canvis de fase i el confinament, i $\mathcal{N} = 4$ SYM deixa de ser-ne una bona aproximació.

Una manera de trencar la simetria conforme en la teoria gauge és afegir un camp escalar en el seu dual gravitatori. En el capítol 3 s'hi presenta i estudia un model de gravetat i camp escalar amb un potencial que fa que la teoria gauge dual tingui un punt fix a l'ultraviolat i un altre a l'infraroig. Entre els dos punts fixos s'hi situa un rang de temperatures on es trenca la simetria conforme i s'hi poden observar En aquest capítol també s'hi presenta el calcul dels modes quasi-normals sobre branes negres estàtiques, que corresponen a les fluctuacions al voltant d'estats termals en equilibri per al plasma dual. Una de les conclusions extreta d'aquest càlcul és que el sistema canvia de canal de dissipació preferit depenent de la temperatura.

7.2.3 Col·lisions en models no conformes

En el capítol 4 es fa servir la família de models no conformes presentada en el capítol 3 per computar col·lisions d'ones de xoc. Aquestes simulacions resulten en un model més aproximat als experiments de col·lisions d'ions reals, on la dinàmica succeïx en presència de viscositat de volum.

En aquest model el valor de la traça del tensor energia moment és proporcional al valor esperat de l'operador dual al camp escalar, que no està fixat per simetria. Això ens proporciona un observable que mesura l'equilibri local i que s'afegeix a la isotropia de pressions i la hidrodinamització pròpiament dita. Un dels resultats més sorprenents de les simulacions és que la hidrodinamització pot succeir molt abans de l'equilibració de la traça.

7.2.4 Transicions de fase i inestabilitats

En l'últim capítol de la tesi s'hi presenta una extensió en l'espai de paràmetres per a la família de models no conformes presentada en el capítol 3. Si hom pren valors imaginaris per al paràmetre que controla la no-conformalitat del model, aquest mostra un cross-over cada cop més pronunciat fins arribar a una transició de fase. Motivat per l'espai de

fases de QCD, en aquest capítol s'hi estudia la dinàmica del model amb presència d'una transició de fase.

En les transicions de fase de primer ordre hi ha una interval d'energies per al qual els estats d'equilibri no són estables. Fent servir el codi numèric presentat en el capítol 4, evolucionem l'inestabilitat present en aquestes fases i constatem que tant l'estat final com l'evolució en sí està ben descrita per hidrodinàmica de segon ordre.

Bibliography

[1] M. Attems, J. Casalderrey-Solana, D. Mateos, I. Papadimitriou, D. Santos-Oliván, C. F. Sopuerta et al., *Thermodynamics, transport and relaxation in non-conformal theories*, *JHEP* **10** (2016) 155, [1603.01254].

[2] M. Attems, J. Casalderrey-Solana, D. Mateos, D. Santos-Oliván, C. F. Sopuerta, M. Triana et al., *Holographic collisions in non-conformal theories*, *JHEP* **01** (2017) 026, [1604.06439].

[3] J. Casalderrey-Solana, D. Mateos, W. van der Schee and M. Triana, *Holographic heavy ion collisions with baryon charge*, *JHEP* **09** (2016) 108, [1607.05273].

[4] M. Attems, Y. Bea, J. Casalderrey-Solana, D. Mateos, M. Triana and M. Zilhao, *Phase Transitions, Inhomogeneous Horizons and Second-Order Hydrodynamics*, 1703.02948.

[5] M. Attems, J. Casalderrey-Solana, D. Mateos, D. Santos-Oliván, C. F. Sopuerta, M. Triana et al., *Paths to equilibrium in non-conformal collisions*, 1703.09681.

[6] D. J. Gross and F. Wilczek, *Ultraviolet behavior of non-abelian gauge theories*, *Phys. Rev. Lett.* **30** (Jun, 1973) 1343–1346.

[7] U. W. Heinz, *From SPS to RHIC: Breaking the barrier to the quark gluon plasma*, *AIP Conf. Proc.* **602** (2001) 281–292, [hep-ph/0109006].

[8] J.-Y. Ollitrault, *Anisotropy as a signature of transverse collective flow*, *Phys. Rev.* **D46** (1992) 229–245.

[9] BRAHMS collaboration, I. G. Bearden et al., *Nuclear stopping in Au + Au collisions at s(NN)**(1/2) = 200-GeV*, *Phys. Rev. Lett.* **93** (2004) 102301, [nucl-ex/0312023].

[10] P. Kovtun, *Lectures on hydrodynamic fluctuations in relativistic theories*, *J. Phys.* **A45** (2012) 473001, [1205.5040].

[11] D. Teaney, J. Lauret and E. V. Shuryak, *A Hydrodynamic description of heavy ion collisions at the SPS and RHIC*, `nucl-th/0110037`.

[12] M. Luzum and P. Romatschke, *Conformal Relativistic Viscous Hydrodynamics: Applications to RHIC results at s(NN)**(1/2) = 200-GeV*, *Phys. Rev.* **C78** (2008) 034915, [`0804.4015`].

[13] D. T. Son and A. O. Starinets, *Viscosity, Black Holes, and Quantum Field Theory*, *Ann. Rev. Nucl. Part. Sci.* **57** (2007) 95–118, [`0704.0240`].

[14] T. Schäfer and D. Teaney, *Nearly Perfect Fluidity: From Cold Atomic Gases to Hot Quark Gluon Plasmas*, *Rept. Prog. Phys.* **72** (2009) 126001, [`0904.3107`].

[15] G. Policastro, D. T. Son and A. O. Starinets, *The Shear viscosity of strongly coupled N=4 supersymmetric Yang-Mills plasma*, *Phys. Rev. Lett.* **87** (2001) 081601, [`hep-th/0104066`].

[16] P. Kovtun, D. T. Son and A. O. Starinets, *Viscosity in strongly interacting quantum field theories from black hole physics*, *Phys. Rev. Lett.* **94** (2005) 111601, [`hep-th/0405231`].

[17] S. Borsanyi, Z. Fodor, C. Hoelbling, S. D. Katz, S. Krieg and K. K. Szabo, *Full result for the QCD equation of state with 2+1 flavors*, *Phys. Lett.* **B730** (2014) 99–104, [`1309.5258`].

[18] L. Keegan, A. Kurkela, P. Romatschke, W. van der Schee and Y. Zhu, *Weak and strong coupling equilibration in nonabelian gauge theories*, *JHEP* **04** (2016) 031, [`1512.05347`].

[19] T. Epelbaum and F. Gelis, *Pressure isotropization in high energy heavy ion collisions*, *Phys. Rev. Lett.* **111** (2013) 232301, [`1307.2214`].

[20] A. Kurkela and Y. Zhu, *Isotropization and hydrodynamization in weakly coupled heavy-ion collisions*, *Phys. Rev. Lett.* **115** (2015) 182301, [`1506.06647`].

[21] J. Casalderrey-Solana, H. Liu, D. Mateos, K. Rajagopal and U. A. Wiedemann, *Gauge/String Duality, Hot QCD and Heavy Ion Collisions*, `1101.0618`.

[22] A. Mukhopadhyay, F. Preis, A. Rebhan and S. A. Stricker, *Semi-Holography for Heavy Ion Collisions: Self-Consistency and First Numerical Tests*, *JHEP* **05** (2016) 141, [`1512.06445`].

[23] J. D. Bekenstein, *Black holes and entropy*, *Phys. Rev.* **D7** (1973) 2333–2346.

[24] S. W. Hawking, *Particle Creation by Black Holes*, *Commun. Math. Phys.* **43** (1975) 199–220.

[25] G. 't Hooft, *A Planar Diagram Theory for Strong Interactions*, *Nucl. Phys.* **B72** (1974) 461.

[26] J. M. Maldacena, *The Large N limit of superconformal field theories and supergravity*, *Int. J. Theor. Phys.* **38** (1999) 1113–1133, [`hep-th/9711200`].

[27] E. Witten, *Anti-de Sitter space and holography*, Adv. Theor. Math. Phys. **2** (1998) 253–291, [`hep-th/9802150`].

[28] S. S. Gubser, I. R. Klebanov and A. M. Polyakov, *Gauge theory correlators from noncritical string theory*, *Phys. Lett.* **B428** (1998) 105–114, [`hep-th/9802109`].

[29] H. Nastase, *Introduction to AdS-CFT*, `0712.0689`.

[30] S. de Haro, S. N. Solodukhin and K. Skenderis, *Holographic reconstruction of space-time and renormalization in the AdS / CFT correspondence*, *Commun. Math. Phys.* **217** (2001) 595–622, [`hep-th/0002230`].

[31] I. Papadimitriou and K. Skenderis, *AdS / CFT correspondence and geometry*, *IRMA Lect. Math. Theor. Phys.* **8** (2005) 73–101, [`hep-th/0404176`].

[32] I. Papadimitriou, *Holographic Renormalization of general dilaton-axion gravity*, *JHEP* **08** (2011) 119, [`1106.4826`].

[33] G. T. Horowitz and V. E. Hubeny, *Quasinormal modes of AdS black holes and the approach to thermal equilibrium*, *Phys. Rev.* **D62** (2000) 024027, [`hep-th/9909056`].

[34] D. T. Son and A. O. Starinets, *Minkowski space correlators in AdS / CFT correspondence: Recipe and applications*, *JHEP* **09** (2002) 042, [`hep-th/0205051`].

[35] P. K. Kovtun and A. O. Starinets, *Quasinormal modes and holography*, *Phys. Rev.* **D72** (2005) 086009, [`hep-th/0506184`].

[36] U. Gürsoy, A. Jansen and W. van der Schee, *New dynamical instability in asymptotically anti–de Sitter spacetime*, *Phys. Rev.* **D94** (2016) 061901, [`1603.07724`].

[37] R. A. Janik, G. Plewa, H. Soltanpanahi and M. Spalinski, *Linearized nonequilibrium dynamics in nonconformal plasma*, *Phys. Rev.* **D91** (2015) 126013, [1503.07149].

[38] S. Grozdanov and A. O. Starinets, *Second-order transport, quasinormal modes and zero-viscosity limit in the Gauss-Bonnet holographic fluid*, 1611.07053.

[39] A. Buchel, M. P. Heller and R. C. Myers, *Equilibration rates in a strongly coupled nonconformal quark-gluon plasma*, *Phys. Rev. Lett.* **114** (2015) 251601, [1503.07114].

[40] M. P. Heller, D. Mateos, W. van der Schee and M. Triana, *Holographic isotropization linearized*, *JHEP* **09** (2013) 026, [1304.5172].

[41] F. Pretorius, *Evolution of binary black hole spacetimes*, *Phys. Rev. Lett.* **95** (2005) 121101, [gr-qc/0507014].

[42] P. M. Chesler and L. G. Yaffe, *Numerical solution of gravitational dynamics in asymptotically anti-de Sitter spacetimes*, *JHEP* **1407** (2014) 086, [1309.1439].

[43] H. Bondi, M. G. J. van der Burg and A. W. K. Metzner, *Gravitational waves in general relativity. 7. Waves from axisymmetric isolated systems*, *Proc. Roy. Soc. Lond.* **A269** (1962) 21–52.

[44] R. K. Sachs, *Gravitational waves in general relativity. 8. Waves in asymptotically flat space-times*, *Proc. Roy. Soc. Lond.* **A270** (1962) 103–126.

[45] J. Winicour, *Characteristic evolution and matching*, *Living Rev.Rel.* **1** (1998) 5, [gr-qc/0102085].

[46] P. Grandclement and J. Novak, *Spectral methods for numerical relativity*, *Living Rev. Rel.* **12** (2009) 1, [0706.2286].

[47] J. Boyd, *Chebyshev and Fourier Spectral Methods: Second Revised Edition*. Dover Books on Mathematics. Dover Publications, 2001.

[48] P. M. Chesler and L. G. Yaffe, *Horizon formation and far-from-equilibrium isotropization in supersymmetric Yang-Mills plasma*, *Phys. Rev. Lett.* **102** (2009) 211601, [0812.2053].

[49] R. A. Janik and P. Witaszczyk, *Towards the description of anisotropic plasma at strong coupling*, *JHEP* **09** (2008) 026, [0806.2141].

[50] J. F. Fuini and L. G. Yaffe, *Far-from-equilibrium dynamics of a strongly coupled non-Abelian plasma with non-zero charge density or external magnetic field*, *JHEP* **07** (2015) 116, [`1503.07148`].

[51] T. Andrade, J. Casalderrey-Solana and A. Ficnar, *Holographic Isotropisation in Gauss-Bonnet Gravity*, *JHEP* **02** (2017) 016, [`1610.08987`].

[52] R. A. Janik and R. B. Peschanski, *Asymptotic perfect fluid dynamics as a consequence of Ads/CFT*, *Phys. Rev.* **D73** (2006) 045013, [`hep-th/0512162`].

[53] D. Grumiller and P. Romatschke, *On the collision of two shock waves in AdS(5)*, *JHEP* **08** (2008) 027, [`0803.3226`].

[54] P. M. Chesler and L. G. Yaffe, *Holography and colliding gravitational shock waves in asymptotically AdS_5 spacetime*, *Phys. Rev. Lett.* **106** (2011) 021601, [`1011.3562`].

[55] J. Casalderrey-Solana, M. P. Heller, D. Mateos and W. van der Schee, *From full stopping to transparency in a holographic model of heavy ion collisions*, *Phys. Rev. Lett.* **111** (2013) 181601, [`1305.4919`].

[56] W. van der Schee and B. Schenke, *Rapidity dependence in holographic heavy ion collisions*, *Phys. Rev.* **C92** (2015) 064907, [`1507.08195`].

[57] J. Casalderrey-Solana, M. P. Heller, D. Mateos and W. van der Schee, *Longitudinal Coherence in a Holographic Model of Asymmetric Collisions*, *Phys. Rev. Lett.* **112** (2014) 221602, [`1312.2956`].

[58] C. Ecker, D. Grumiller, P. Stanzer, S. A. Stricker and W. van der Schee, *Exploring nonlocal observables in shock wave collisions*, *JHEP* **11** (2016) 054, [`1609.03676`].

[59] S. Grozdanov and W. van der Schee, *Coupling constant corrections in holographic heavy ion collisions*, `1610.08976`.

[60] J. P. Gauntlett and J. B. Gutowski, *All supersymmetric solutions of minimal gauged supergravity in five-dimensions*, *Phys. Rev.* **D68** (2003) 105009, [`hep-th/0304064`].

[61] J. Erdmenger, M. Haack, M. Kaminski and A. Yarom, *Fluid dynamics of R-charged black holes*, *JHEP* **01** (2009) 055, [`0809.2488`].

[62] N. Banerjee, J. Bhattacharya, S. Bhattacharyya, S. Dutta, R. Loganayagam and

P. Surowka, *Hydrodynamics from charged black branes*, *JHEP* **01** (2011) 094, [0809.2596].

[63] W. van der Schee, *Gravitational collisions and the quark-gluon plasma*. PhD thesis, Utrecht U., 2014. 1407.1849.

[64] P. M. Chesler, N. Kilbertus and W. van der Schee, *Universal hydrodynamic flow in holographic planar shock collisions*, *JHEP* **11** (2015) 135, [1507.02548].

[65] J. L. Albacete, Y. V. Kovchegov and A. Taliotis, *Asymmetric Collision of Two Shock Waves in AdS(5)*, *JHEP* **05** (2009) 060, [0902.3046].

[66] P. Arnold, P. Romatschke and W. van der Schee, *Absence of a local rest frame in far from equilibrium quantum matter*, *JHEP* **10** (2014) 110, [1408.2518].

[67] E917 collaboration, B. B. Back et al., *Baryon rapidity loss in relativistic Au+Au collisions*, *Phys. Rev. Lett.* **86** (2001) 1970–1973, [nucl-ex/0003007].

[68] NA49 collaboration, H. Appelshauser et al., *Baryon stopping and charged particle distributions in central Pb + Pb collisions at 158-GeV per nucleon*, *Phys. Rev. Lett.* **82** (1999) 2471–2475, [nucl-ex/9810014].

[69] E. Avsar, E. Iancu, L. McLerran and D. N. Triantafyllopoulos, *Shockwaves and deep inelastic scattering within the gauge/gravity duality*, *JHEP* **11** (2009) 105, [0907.4604].

[70] J. Casalderrey-Solana, D. C. Gulhan, J. G. Milhano, D. Pablos and K. Rajagopal, *A Hybrid Strong/Weak Coupling Approach to Jet Quenching*, *JHEP* **10** (2014) 019, [1405.3864].

[71] E. Iancu and A. Mukhopadhyay, *A semi-holographic model for heavy-ion collisions*, *JHEP* **06** (2015) 003, [1410.6448].

[72] HotQCD collaboration, A. Bazavov et al., *Equation of state in (2+1)-flavor QCD*, *Phys. Rev.* **D90** (2014) 094503, [1407.6387].

[73] S. Ryu, J. F. Paquet, C. Shen, G. S. Denicol, B. Schenke, S. Jeon et al., *Importance of the Bulk Viscosity of QCD in Ultrarelativistic Heavy-Ion Collisions*, *Phys. Rev. Lett.* **115** (2015) 132301, [1502.01675].

[74] P. Bozek, *Collective flow in p-Pb and d-Pd collisions at TeV energies*, *Phys. Rev.* **C85** (2012) 014911, [1112.0915].

[75] B. Schenke and R. Venugopalan, *Eccentric protons? Sensitivity of flow to system size and shape in p+p, p+Pb and Pb+Pb collisions*, *Phys. Rev. Lett.* **113** (2014) 102301, [1405.3605].

[76] M. Habich, G. A. Miller, P. Romatschke and W. Xiang, *A Hydrodynamic Study of p+p Collisions at $\sqrt{s} = 7$ TeV*, 1512.05354.

[77] S. Jeon and U. Heinz, *Introduction to Hydrodynamics*, *Int. J. Mod. Phys.* **E24** (2015) 1530010, [1503.03931].

[78] M. P. Heller, R. A. Janik and P. Witaszczyk, *The characteristics of thermalization of boost-invariant plasma from holography*, *Phys. Rev. Lett.* **108** (2012) 201602, [1103.3452].

[79] P. M. Chesler and L. G. Yaffe, *Boost invariant flow, black hole formation, and far-from-equilibrium dynamics in N = 4 supersymmetric Yang-Mills theory*, *Phys. Rev.* **D82** (2010) 026006, [0906.4426].

[80] P. M. Chesler and L. G. Yaffe, *Holography and off-center collisions of localized shock waves*, *JHEP* **10** (2015) 070, [1501.04644].

[81] M. P. Heller, R. A. Janik, M. Spali?ski and P. Witaszczyk, *Coupling hydrodynamics to nonequilibrium degrees of freedom in strongly interacting quark-gluon plasma*, *Phys. Rev. Lett.* **113** (2014) 261601, [1409.5087].

[82] R. A. Janik, J. Jankowski and H. Soltanpanahi, *Non-equilibrium dynamics and phase transitions*, 1512.06871.

[83] A. Buchel and A. Day, *Universal relaxation in quark-gluon plasma at strong coupling*, *Phys. Rev.* **D92** (2015) 026009, [1505.05012].

[84] R. Rougemont, A. Ficnar, S. Finazzo and J. Noronha, *Energy loss, equilibration, and thermodynamics of a baryon rich strongly coupled quark-gluon plasma*, 1507.06556.

[85] U. Gursoy, M. Jarvinen and G. Policastro, *Late time behavior of non-conformal plasmas*, *JHEP* **01** (2016) 134, [1507.08628].

[86] U. Gursoy, A. Jansen, W. Sybesma and S. Vandoren, *Holographic Equilibration of Nonrelativistic Plasmas*, 1602.01375.

[87] M. Ali-Akbari, F. Charmchi, H. Ebrahim and L. Shahkarami, *Various Time-Scales*

of Relaxation, `1602.07903`.

[88] M. Bianchi, D. Z. Freedman and K. Skenderis, *Holographic renormalization*, *Nucl. Phys.* **B631** (2002) 159–194, [`hep-th/0112119`].

[89] L. Girardello, M. Petrini, M. Porrati and A. Zaffaroni, *Novel local CFT and exact results on perturbations of N=4 superYang Mills from AdS dynamics*, *JHEP* **12** (1998) 022, [`hep-th/9810126`].

[90] I. Papadimitriou and K. Skenderis, *Correlation functions in holographic RG flows*, *JHEP* **10** (2004) 075, [`hep-th/0407071`].

[91] E. Megias, H. J. Pirner and K. Veschgini, *QCD thermodynamics using five-dimensional gravity*, *Phys. Rev.* **D83** (2011) 056003, [`1009.2953`].

[92] K. Veschgini, E. Megias and H. J. Pirner, *Trouble Finding the Optimal AdS/QCD*, *Phys. Lett.* **B696** (2011) 495–498, [`1009.4639`].

[93] U. Gursoy, E. Kiritsis, L. Mazzanti and F. Nitti, *Holography and Thermodynamics of 5D Dilaton-gravity*, *JHEP* **05** (2009) 033, [`0812.0792`].

[94] S. S. Gubser and A. Nellore, *Mimicking the QCD equation of state with a dual black hole*, *Phys. Rev.* **D78** (2008) 086007, [`0804.0434`].

[95] C. Eling and Y. Oz, *A Novel Formula for Bulk Viscosity from the Null Horizon Focusing Equation*, *JHEP* **06** (2011) 007, [`1103.1657`].

[96] S. S. Gubser, S. S. Pufu and F. D. Rocha, *Bulk viscosity of strongly coupled plasmas with holographic duals*, *JHEP* **08** (2008) 085, [`0806.0407`].

[97] J. Mas and J. Tarrio, *Hydrodynamics from the Dp-brane*, *JHEP* **05** (2007) 036, [`hep-th/0703093`].

[98] A. Buchel, *Violation of the holographic bulk viscosity bound*, *Phys. Rev.* **D85** (2012) 066004, [`1110.0063`].

[99] P. Benincasa, A. Buchel and A. O. Starinets, *Sound waves in strongly coupled non-conformal gauge theory plasma*, *Nucl. Phys.* **B733** (2006) 160–187, [`hep-th/0507026`].

[100] A. Nunez and A. O. Starinets, *AdS / CFT correspondence, quasinormal modes, and thermal correlators in N=4 SYM*, *Phys. Rev.* **D67** (2003) 124013, [`hep-th/0302026`].

[101] P. M. Chesler, *Colliding shock waves and hydrodynamics in small systems*, *Phys. Rev. Lett.* **115** (2015) 241602, [1506.02209].

[102] P. M. Chesler, *How big are the smallest drops of quark-gluon plasma?*, 1601.01583.

[103] H. O. Kreiss and J. Oliger, *Methods for the Approximate Solution of Time Dependent Problems*. World Meteorological Organization, 1973.

[104] J. P. Boyd, *Chebyshev and Fourier Spectral Methods*. Dover, New York, 2nd ed., 2001.

[105] R. A. Janik, J. Jankowski and H. Soltanpanahi, *Quasinormal modes and the phase structure of strongly coupled matter*, *JHEP* **06** (2016) 047, [1603.05950].

[106] P. M. Chesler and D. Teaney, *Dilaton emission and absorption from far-from-equilibrium non-abelian plasma*, 1211.0343.

[107] P. M. Chesler and D. Teaney, *Dynamical Hawking Radiation and Holographic Thermalization*, 1112.6196.

[108] F. Karsch, D. Kharzeev and K. Tuchin, *Universal properties of bulk viscosity near the QCD phase transition*, *Phys. Lett.* **B663** (2008) 217–221, [0711.0914].

[109] G. Torrieri and I. Mishustin, *Instability of Boost-invariant hydrodynamics with a QCD inspired bulk viscosity*, *Phys. Rev.* **C78** (2008) 021901, [0805.0442].

[110] P. Bozek, *Flow and interferometry in 3+1 dimensional viscous hydrodynamics*, *Phys. Rev.* **C85** (2012) 034901, [1110.6742].

[111] P. Bozek and I. Wyskiel-Piekarska, *Particle spectra in Pb-Pb collisions at $sqrtS_N N = 2.76$ TeV*, *Phys. Rev.* **C85** (2012) 064915, [1203.6513].

[112] A. Monnai and T. Hirano, *Effects of Bulk Viscosity at Freezeout*, *Phys. Rev.* **C80** (2009) 054906, [0903.4436].

[113] G. S. Denicol, T. Kodama and T. Koide, *The effect of shear and bulk viscosities on elliptic flow*, *J. Phys.* **G37** (2010) 094040, [1002.2394].

[114] H. Song and U. W. Heinz, *Interplay of shear and bulk viscosity in generating flow in heavy-ion collisions*, *Phys. Rev.* **C81** (2010) 024905, [0909.1549].

[115] K. Dusling and T. Schäfer, *Bulk viscosity, particle spectra and flow in heavy-ion*

collisions, *Phys. Rev.* **C85** (2012) 044909, [1109.5181].

[116] J. Noronha-Hostler, J. Noronha and F. Grassi, *Bulk viscosity-driven suppression of shear viscosity effects on the flow harmonics at energies available at the BNL Relativistic Heavy Ion Collider*, *Phys. Rev.* **C90** (2014) 034907, [1406.3333].

[117] W. Florkowski, R. Ryblewski, N. Su and K. Tywoniuk, *Transport coefficients of the Gribov-Zwanziger plasma*, *Phys. Rev.* **C94** (2016) 044904, [1509.01242].

[118] ALICE collaboration, B. Abelev et al., *Long-range angular correlations on the near and away side in p-Pb collisions at $\sqrt{s_{NN}} = 5.02$ TeV*, *Phys. Lett.* **B719** (2013) 29–41, [1212.2001].

[119] ATLAS collaboration, G. Aad et al., *Observation of Associated Near-Side and Away-Side Long-Range Correlations in $\sqrt{s_{NN}}=5.02TeV$ Proton-Lead Collisions with the ATLAS Detector*, *Phys. Rev. Lett.* **110** (2013) 182302, [1212.5198].

[120] PHENIX collaboration, A. Adare et al., *Quadrupole Anisotropy in Dihadron Azimuthal Correlations in Central d+Au Collisions at $\sqrt{s_{NN}}=200$ GeV*, *Phys. Rev. Lett.* **111** (2013) 212301, [1303.1794].

[121] CMS collaboration, S. Chatrchyan et al., *Multiplicity and transverse momentum dependence of two- and four-particle correlations in pPb and PbPb collisions*, *Phys. Lett.* **B724** (2013) 213–240, [1305.0609].

[122] PHENIX collaboration, A. Adare et al., *Measurements of elliptic and triangular flow in high-multiplicity ^3He+Au collisions at $\sqrt{s_{NN}} = 200$ GeV*, *Phys. Rev. Lett.* **115** (2015) 142301, [1507.06273].

[123] ATLAS collaboration, G. Aad et al., *Observation of long-range elliptic anisotropies in $\sqrt{s} =13$ and 2.76 TeV pp collisions with the ATLAS detector*, 1509.04776.

[124] J. L. Nagle, A. Adare, S. Beckman, T. Koblesky, J. Orjuela Koop, D. McGlinchey et al., *Exploiting Intrinsic Triangular Geometry in Relativistic He3+Au Collisions to Disentangle Medium Properties*, *Phys. Rev. Lett.* **113** (2014) 112301, [1312.4565].

[125] I. Kozlov, M. Luzum, G. Denicol, S. Jeon and C. Gale, *Transverse momentum structure of pair correlations as a signature of collective behavior in small collision systems*, 1405.3976.

[126] P. Romatschke, *Light-Heavy Ion Collisions: A window into pre-equilibrium QCD dynamics?*, *Eur. Phys. J.* **C75** (2015) 305, [1502.04745].

[127] P. Bozek and W. Broniowski, *Hydrodynamic modeling of* ^{3} *He–Au collisions at* $\sqrt{sNN}$=*200 GeV*, *Phys. Lett.* **B747** (2015) 135–138, [1503.00468].

[128] J. D. Orjuela Koop, R. Belmont, P. Yin and J. L. Nagle, *Exploring the Beam Energy Dependence of Flow-Like Signatures in Small System d+Au Collisions*, *Phys. Rev.* **C93** (2016) 044910, [1512.06949].

[129] K. Dusling, W. Li and B. Schenke, *Novel collective phenomena in high-energy proton–proton and proton–nucleus collisions*, *Int. J. Mod. Phys.* **E25** (2016) 1630002, [1509.07939].

[130] F. R. Brown, F. P. Butler, H. Chen, N. H. Christ, Z. Dong, W. Schaffer et al., *On the existence of a phase transition for qcd with three light quarks*, *Phys. Rev. Lett.* **65** (Nov, 1990) 2491–2494.

[131] M. A. Stephanov, *QCD phase diagram: An Overview*, *PoS* **LAT2006** (2006) 024, [hep-lat/0701002].

[132] K. Fukushima and T. Hatsuda, *The phase diagram of dense QCD*, *Rept. Prog. Phys.* **74** (2011) 014001, [1005.4814].

[133] G. Odyniec, *Future of the beam energy scan program at RHIC*, *EPJ Web Conf.* **95** (2015) 03027.

[134] O. DeWolfe, S. S. Gubser and C. Rosen, *A holographic critical point*, *Phys. Rev.* **D83** (2011) 086005, [1012.1864].

[135] O. DeWolfe, S. S. Gubser and C. Rosen, *Dynamic critical phenomena at a holographic critical point*, *Phys. Rev.* **D84** (2011) 126014, [1108.2029].

[136] STAR collaboration, K. H. Ackermann et al., *Elliptic flow in Au + Au collisions at (S(NN))**(1/2) = 130 GeV*, *Phys. Rev. Lett.* **86** (2001) 402–407, [nucl-ex/0009011].

[137] PHENIX collaboration, S. S. Adler et al., *Elliptic flow of identified hadrons in Au+Au collisions at s(NN)**(1/2) = 200-GeV*, *Phys. Rev. Lett.* **91** (2003) 182301, [nucl-ex/0305013].

[138] PHOBOS collaboration, B. B. Back et al., *Centrality and pseudorapidity*

dependence of elliptic flow for charged hadrons in Au+Au collisions at s(NN)**(1/2) = 200-GeV, *Phys. Rev.* **C72** (2005) 051901, [`nucl-ex/0407012`].

[139] ATLAS collaboration, G. Aad et al., *Measurement of the azimuthal anisotropy for charged particle production in $\sqrt{s_{NN}} = 2.76$ TeV lead-lead collisions with the ATLAS detector*, *Phys. Rev.* **C86** (2012) 014907, [`1203.3087`].

[140] CMS collaboration, S. Chatrchyan et al., *Measurement of the elliptic anisotropy of charged particles produced in PbPb collisions at $\sqrt{s_{NN}}$=2.76 TeV*, *Phys. Rev.* **C87** (2013) 014902, [`1204.1409`].

[141] ALICE collaboration, K. Aamodt et al., *Elliptic flow of charged particles in Pb-Pb collisions at 2.76 TeV*, *Phys. Rev. Lett.* **105** (2010) 252302, [`1011.3914`].

[142] P. Huovinen, P. F. Kolb, U. W. Heinz, P. V. Ruuskanen and S. A. Voloshin, *Radial and elliptic flow at RHIC: Further predictions*, *Phys. Lett.* **B503** (2001) 58–64, [`hep-ph/0101136`].

[143] T. Hirano, U. W. Heinz, D. Kharzeev, R. Lacey and Y. Nara, *Hadronic dissipative effects on elliptic flow in ultrarelativistic heavy-ion collisions*, *Phys. Lett.* **B636** (2006) 299–304, [`nucl-th/0511046`].

[144] B. Schenke, S. Jeon and C. Gale, *Elliptic and triangular flow in event-by-event (3+1)D viscous hydrodynamics*, *Phys. Rev. Lett.* **106** (2011) 042301, [`1009.3244`].

[145] C. Shen, Z. Qiu, H. Song, J. Bernhard, S. Bass and U. Heinz, *The iEBE-VISHNU code package for relativistic heavy-ion collisions*, *Comput. Phys. Commun.* **199** (2016) 61–85, [`1409.8164`].

[146] J. E. Bernhard, J. S. Moreland, S. A. Bass, J. Liu and U. Heinz, *Applying Bayesian parameter estimation to relativistic heavy-ion collisions: simultaneous characterization of the initial state and quark-gluon plasma medium*, *Phys. Rev.* **C94** (2016) 024907, [`1605.03954`].

[147] P. Romatschke, *Do nuclear collisions create a locally equilibrated quark–gluon plasma?*, *Eur. Phys. J.* **C77** (2017) 21, [`1609.02820`].

[148] CMS collaboration, V. Khachatryan et al., *Observation of Long-Range Near-Side Angular Correlations in Proton-Proton Collisions at the LHC*, *JHEP* **09** (2010) 091, [`1009.4122`].

[149] CMS collaboration, V. Khachatryan et al., *Evidence for collectivity in pp*

collisions at the LHC, *Phys. Lett.* **B765** (2017) 193–220, [`1606.06198`].

[150] R. D. Weller and P. Romatschke, *One fluid to rule them all: viscous hydrodynamic description of event-by-event central p+p, p+Pb and Pb+Pb collisions at* $\sqrt{s} = 5.02$ *TeV*, `1701.07145`.

[151] L. Keegan, A. Kurkela, A. Mazeliauskas and D. Teaney, *Initial conditions for hydrodynamics from weakly coupled pre-equilibrium evolution*, *JHEP* **08** (2016) 171, [`1605.04287`].

[152] O. J. C. Dias, J. E. Santos and B. Way, *Localised and nonuniform thermal states of super-Yang-Mills on a circle*, `1702.07718`.

[153] P. Chomaz, M. Colonna and J. Randrup, *Nuclear spinodal fragmentation*, *Phys. Rept.* **389** (2004) 263–440.

[154] A. Buchel, *A Holographic perspective on Gubser-Mitra conjecture*, *Nucl. Phys.* **B731** (2005) 109–124, [`hep-th/0507275`].

[155] R. Emparan, T. Harmark, V. Niarchos and N. A. Obers, *World-Volume Effective Theory for Higher-Dimensional Black Holes*, *Phys. Rev. Lett.* **102** (2009) 191301, [`0902.0427`].

[156] R. Emparan, T. Harmark, V. Niarchos and N. A. Obers, *Essentials of Blackfold Dynamics*, *JHEP* **03** (2010) 063, [`0910.1601`].

[157] R. Gregory and R. Laflamme, *Black strings and p-branes are unstable*, *Phys. Rev. Lett.* **70** (1993) 2837–2840, [`hep-th/9301052`].

[158] P. Romatschke, *Relativistic Viscous Fluid Dynamics and Non-Equilibrium Entropy*, *Class. Quant. Grav.* **27** (2010) 025006, [`0906.4787`].

[159] P. Kleinert and J. Probst, *Second-Order Hydrodynamics and Universality in Non-Conformal Holographic Fluids*, *JHEP* **12** (2016) 091, [`1610.01081`].